

University of Warwick institutional repository: <http://go.warwick.ac.uk/wrap>

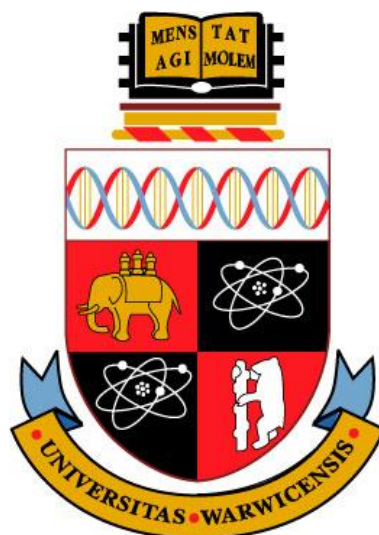
**A Thesis Submitted for the Degree of PhD at the University of Warwick**

<http://go.warwick.ac.uk/wrap/54607>

This thesis is made available online and is protected by original copyright.

Please scroll down to view the document itself.

Please refer to the repository record for this item for information to help you to cite it. Our policy information is available from the repository home page.



# Crystallography of New Materials for Clean Energy Production and the Switch to a Hydrogen Based Economy

by

**Iain Dunn**

**Thesis**

Submitted to the University of Warwick

for the degree of

**Doctor of Philosophy**

**Department of Physics**

October 2012

THE UNIVERSITY OF  
**WARWICK**

# Contents

Title Page	i
Contents	ii
List of Tables	vi
List of Figures	vii
Acknowledgments	x
Declaration and Published Work	xii
Abstract	xiii
Glossary & Abbreviations	xiv
<b>Chapter 1 Introduction .....</b>	<b>1</b>
1.1 The Hydrogen Economy .....	1
1.1.1 Non Renewable Hydrogen Production .....	1
1.1.2 Greenhouse Gas Free Production .....	3
1.1.3 Hydrogen Supply and Storage.....	4
1.1.4 On-Board Hydrogen Storage.....	5
1.1.5 Hydrogen Utilisation .....	7
1.2 Thermal Photovoltaic Electricity Production .....	9
1.3 Literature Review .....	10
1.3.1 Targets for On-Board Hydrogen Storage .....	11
1.3.2 Solid State Hydrogen Storage .....	13
1.3.3 Band Gap Narrowing.....	16
1.4 Aims of the Present Work.....	17
References .....	19

<b>Chapter 2 Experimental Background &amp; Theory .....</b>	<b>22</b>
2.1 Introduction .....	22
2.2 Crystallography .....	22
2.2.1. Definition of a Crystal .....	22
2.2.2 Crystal Systems .....	22
2.2.3 Powder X-ray Diffraction.....	24
2.2.4 The Rietveld Method .....	25
2.2.4.1 Peak Shape .....	30
2.2.4.2 Goodness-of-fit Parameters.....	31
2.2.5 High Resolution X-ray Diffraction.....	33
2.2.5.1 Reciprocal Space Maps .....	35
2.2.5.2 Relaxation and Composition .....	38
2.2.6 Single-Crystal Diffraction .....	41
2.2.6.1 Data Collection.....	41
2.2.6.2 Structural Refinement.....	42
2.3 Complementary Techniques to Diffraction.....	43
2.3.1 Secondary Ion Mass Spectroscopy (SIMS) .....	43
2.3.2 Nuclear Magnetic Resonance (NMR).....	44
2.3.3 Thermal Analysis (TA).....	48
2.4 Air and Moisture Sensitive Samples .....	48
References .....	50
<b>Chapter 3 Di-sodium Amide Borohydride .....</b>	<b>51</b>
3.1 Introduction .....	51
3.2 Experimental Details .....	52
3.2.1 Synthesis .....	52
3.2.2 Thermal Analysis and Structural Experiments .....	53
3.3 Experimental Results.....	55
3.3.1 Powder Sample .....	55
3.3.2 Single Crystal Results .....	67
3.4 Conclusions .....	71

3.5 Further Work.....	72
References .....	73
<b>Chapter 4 Homoepitaxial Growth of Nitrogen - doped Antimonides .....</b>	<b>74</b>
4.1 Introduction .....	74
4.2 Sample Growth .....	75
4.3 Sample Characterisation .....	76
4.4 Experimental Results.....	78
4.4.1 InNSb Grown on InSb .....	78
4.4.2 GaNSb Grown on GaSb .....	81
4.4.3 Relaxation of GaNSb Grown on GaSb .....	83
4.4.4 Crystal quality of GaNSb Grown on GaSb .....	85
4.5 Conclusions .....	88
4.6 Further Work.....	89
References .....	90
<b>Chapter 5 Annealing of GaNSb Samples Grown Heteroepitaxially on GaAs.....</b>	<b>91</b>
5.1 Introduction .....	91
5.2 Sample Growth and Annealing .....	92
5.3 Experimental Details .....	93
5.3.1 X-ray Diffraction .....	93
5.3.2 Secondary Ion Mass Spectroscopy (SIMS) .....	94
5.4 Experimental Results.....	94
5.4.1 X-ray Analysis of Nitrogen Content.....	94
5.4.2 Crystal Quality Determined by X-ray Analysis.....	102
5.4.3 SIMS Analysis of Nitrogen Content .....	107
5.5 Conclusions .....	113
5.6 Further Work.....	113

References .....	115
<b>Chapter 6 Sodium Lithium Borohydride .....</b>	<b>116</b>
6.1 Introduction .....	116
6.2 Experimental Details .....	117
6.3 Experimental Results.....	120
6.3.1 Initial Synthesis .....	120
6.3.2 In Situ Synthesis of $\text{Li}_{0.1}\text{Na}_{0.9}\text{BH}_4$ .....	123
6.3.3 In Situ Synthesis of Li-0.2 and Li-0.3 .....	126
6.3.4 Ex Situ Analysis of Lithium Sodium Borohydride .....	126
6.3.5 Nuclear Magnetic Resonance .....	132
6.3.6 Thermal Analysis .....	137
6.4 Conclusions .....	139
6.5 Further Work.....	140
References .....	142
<b>Chapter 7 Conclusions .....</b>	<b>143</b>
7.1 Hydrogen Storage Materials .....	143
7.2 Dilute Nitrides .....	144
7.3 Suggestions for Further Study.....	145

# List of Tables

1.1 Hydrogen fuel cell types, power outputs and working temperatures.....	8
1.2 DOE target for on-board hydrogen storage systems .....	12
2.1 Seven crystal systems and symmetry operators.....	23
2.2 Definitions of peak shape parameters for Rietveld refinement .....	31
2.3 Selection of R-values used in Rietveld refinement .....	32
2.4 Quality of fit parameters for single-crystal refinement .....	43
3.1 Unit cell volume fitting parameters of O-phase di-sodium amide borohydride .....	63
3.2 Lattice fitting results from O-phase and MC-phase of $\text{Na}_2\text{BH}_4\text{NH}_2$ .....	69
4.1 Properties of gallium antimonide and indium antimonide .....	74
4.2 Nitrogen incorporation and lattice relaxation of GaNSb layers.....	84
5.1 Annealing temperatures of GaNSb grown on GaAs.....	92
6.1 Annealing parameters of three lithium sodium borohydride samples.....	119
6.2 Lattice parameters and thermal expansion of lithium containing samples .....	128

# List of Figures

1.1 Gravimetric and volumetric densities of various hydrogen storage materials.....	13
2.1 Geometry of para-focused and transmission x-ray modes.....	27
2.2 Arrangement of the components that make up the HR-XRD .....	34
2.3 Schematic view of the degrees of freedom of HR-XRD sample stage .....	35
2.4 Schematic view of reciprocal space from a 001 oriented crystal .....	36
2.5 Peaks positions of strained and relaxed layers on 004 and 224 RSM.....	37
2.6 Tetragonal distortions of crystal structures under tensile and compressive strain .....	39
3.1 X-ray diffraction rings collected on a 2-dimensional detector .....	54
3.2 DSC of the synthesis and melting of di-sodium amide borohydride .....	56
3.3 Crystal structures of C-phase and O-phase di-sodium amide borohydride.....	57
3.4 Diffraction patterns of C-phase and O-phase di-sodium amide borohydride .....	58
3.5 Stack plot of di-sodium amide borohydride diffraction patterns.....	58
3.6 Lattice parameters of di-sodium amide borohydride as a function of temperature ...	59
3.7 a and b lattice parameters of $\text{Na}_2\text{BH}_4\text{NH}_2$ O-phase as a function of temperature .....	61
3.8 c-lattice parameters of $\text{Na}_2\text{BH}_4\text{NH}_2$ O-phase as a function of temperature.....	61
3.9 Unit cell volume of O-phase $\text{Na}_2\text{BH}_4\text{NH}_2$ as a function of temperature .....	63
3.10 Cubic unit cell volume of $\text{Na}_2\text{BH}_4\text{NH}_2$ C-phase as a function of temperature .....	64
3.11 Cubic lattice parameters of MC-phase of $\text{Na}_2\text{BH}_4\text{NH}_2$ as a function of temperature .	65
3.12 Weight percentages of C-phase and O-phase of $\text{Na}_2\text{BH}_4\text{NH}_2$ .....	65
3.13 Volume per formula unit of $\text{Na}_2\text{BH}_4\text{NH}_2$ as a function of temperature .....	67



3.14 0kl plane of MC-phase of $\text{Na}_2\text{BH}_4\text{NH}_2$ from single-crystal diffraction.....	68
3.15 0kl plane of O-phase of $\text{Na}_2\text{BH}_4\text{NH}_2$ from single-crystal diffraction.....	69
4.1 Structure of Zinc Blende materials.....	74
4.2 Rocking curve of GaNSb sample and fitting.....	77
4.3 Nitrogen incorporation in InNSb as a function of temperature .....	79
4.4 2theta FWHM of InNSb layers as a function of temperature .....	81
4.5 Nitrogen incorporation in GaNSb as a function of temperature .....	82
4.6 Example of symmetric and asymmetric RSM scans of a homoepitaxial layer.....	83
4.7 Lattice relaxation of GaNSb layers as a function of temperature.....	85
4.8 Omega FWHM of GaNSb layer as a function of nitrogen content.....	87
4.9 Omega FWHM of GaNSb layer as a function of growth temperature.....	87
5.1 Example 2theta-omega scan of GaNSb layer grown on GaAs .....	95
5.2 Nitrogen content of various samples assuming 100% relaxation.....	97
5.3 Example of symmetric and asymmetric RSM scans.....	98
5.4 Nitrogen content and lattice relaxation of annealed GaNSb samples.....	100
5.5 Omega and 2theta FWHM as a function of annealing temperature .....	104
5.6 Omega and 2theta FWHM of samples as a function of nitrogen content.....	106
5.7 SIMS profile of nitrogen content as a function of depth for annealed samples.....	110
5.8 SIMS profile of antimony ion yield as a function of exposure time.....	112
6.1 Crystal structure of lithium and sodium borohydride .....	117
6.2 Cubic lattice parameters of mixed ion sample and pure sodium borohydride .....	120
6.3 X-ray diffraction scans of the initial sample before and after heating .....	121
6.4 FWHM of 002 diffraction peak of lithium sodium borohydride .....	122

6.5 Cubic lattice parameters of in situ synthesis Li-0.1 sample .....	124
6.6 FWHM of 002 diffraction peak of in situ synthesis Li-0.1 sample.....	125
6.7 Cubic lattice parameter of lithium samples as a function of temperature .....	127
6.8 Linear thermal expansion coefficients as a function of lithium content .....	129
6.9 FWHM of 002 peak from lithium containing samples .....	130
6.10 FWHM of 111 peak from lithium containing samples .....	130
6.11 Lithium-7 NMR from lithium containing samples Li-0.1, Li-0.2 and Li-0.3.....	133
6.12 Sodium-23 NMR spectra from lithium containing samples and pure NaBH <sub>4</sub> .....	135
6.13 Boron-11 NMR spectra from lithium containing samples and pure NaBH <sub>4</sub> .....	137
6.14 Differential thermal analysis of lithium containing samples .....	138

# Acknowledgements

I must firstly thank my supervisor, Pam Thomas, for all the guidance and support that she has bestowed over the last four years. She has provided both knowledge and funds that have helped this work progress. As well as wrangling together the money to buy the glove box, without which most of this work would not be possible. By securing extra money to keep me funded over the last six months Pam has allowed me to survive the process of writing this thesis, something she may be regretting after having to check through my grammar many times- for which I'm very grateful.

I am also thankful to various postdocs in the crystallography group who helped along the way, particularly Dr. David Walker who has taught me how to use all the x-ray diffraction equipment as well as many other aspects of crystallography too numerous to mention. Dr Dean Keeble has given me masses of advice regarding the software used for both signal-crystal diffraction data collection and the refinement process and Dr David Woodward for adding his unconventional style and approach to problems. There are other members of the physics department who need a special mention, including, in no particular order, Frederick Romer and John Hanna for all their help collecting and analysing NMR data; Dr. Richard Morris for collecting and analysing SIMS data; Mark Ashwin for growing various semiconductor samples and Tim Veal providing me with others, all of whom have helped with advice and guidance as well. Dave Hammond, who has not only kept the XRD equipment running over the years, but who has also helped run all the thermal analysis experiment I have needed. Dr. Peter Scott from the chemistry department who offered advice about glove boxes and helped us procure the glove box used throughout this work.

I can't fail to mention the other Ph.D students whom I have had the great pleasure to get to know over the course of this work, both in the Crystallography group but also in the Glass group. Again in no particular order, these include Robin, Dan, Kaustuv, Aoife, Steve, Andy, Meng, Oli and Sam. Many of whom have not only helped keep me on my toes and spurred me on to finish but also offered a sounding board for my thoughts and ideas. Special thanks have to go to, now, Dr Martin Mee without whom I would have either finished writing this thesis sooner or not finished it at all! He has offered counsel and direction about all things physics related and otherwise. Our many trips for coffee and the 'occasional' trip to the pub have been a welcome distraction and have only rarely descended into drunkenness.

Finally I would like to thank my parents and sister who have lovingly put up with living with me whilst having no idea what it is I get up to everyday when I leave the house, and my friends, particularly, Daniel Waldron and Adam Trus, who have for the most part resisted calling me a tax-dodging student and have feigned interest whenever I tell them what I've been up to.

# Declaration and Published Work

I declare that the work presented in this thesis is my own except where stated otherwise, and was carried out entirely at the University of Warwick, during the period of October 2008 to September 2012, under the supervision of Prof. Pam Thomas. The research reported here has not been submitted, either wholly or in part, in this or any other academic institution for admission to a higher degree. Some parts of this work have been published, as listed below.

## **Published Papers**

M. J. Ashwin, T. D. Veal, J. J. Bompfrey, I. R. Dunn, D. Walker, P. A. Thomas, T. S. Jones, AIP Advances **1** (2011) 032159

I. R. Dunn  
September 2012

# Abstract

New energy materials have been investigated, including hydrogen storage materials and dilute nitride semiconductors. The two potential hydrogen storage materials to have been investigated are di-sodium amide borohydride ( $\text{Na}_2\text{NH}_2\text{BH}_4$ ) and lithium sodium borohydride ( $\text{LiNaBH}_4$ ). Additionally, the homoepitaxial growth of  $\text{InNSb}$  and  $\text{GaNSb}$  across a range of growth temperatures and rates has been examined and the effect of annealing  $\text{GaNSb}$  layers grown on  $\text{GaAs}$  has also been studied.

It has been shown that  $\text{Na}_2\text{NH}_2\text{BH}_4$  undergoes a first order phase transition between a low temperature orthorhombic phase and a high temperature cubic phase. There is a large coexistence region between the two phases of  $-10^\circ\text{C}$  to  $70^\circ\text{C}$ . The relative percentages of each of these phases in this region are dependent on whether the sample is been heated or cooled and the rate of change of the temperature, leading to a discrepancy in the overall volume of the sample between heating and cooling. It has also been proved that there is a metastable cubic phase of the sample that is seen when this material is first formed and cooled.

Phase pure samples of  $\text{LiNaBH}_4$  have been synthesised from mixtures of sodium borohydride and lithium borohydride, with varying amounts of lithium inclusion. This lithium inclusion has resulted in some disorder in the sodium borohydride structure of the samples up to temperatures of  $200^\circ\text{C}$ , which disorder is increased as the amount of lithium increases. The inclusion of lithium has reduced the hydrogen desorption temperature by c.a.10% from  $550^\circ\text{C}$  for pure sodium borohydride to  $504^\circ\text{C}$  for the sample with the most lithium inclusion.

Both  $\text{InNSb}$  and  $\text{GaNSb}$  exhibit a linear relationship between growth temperature and amount of nitrogen inclusion, with both more nitrogen being included and a greater maximum growth temperature seen in the  $\text{GaSb}$ -based material. In both types of material higher growth rates have resulted in less nitrogen inclusion at a given temperature. It has been shown that the increased amount of nitrogen inclusion has improved the quality of the grown layer.

Annealing of heteroepitaxially grown  $\text{GaNSb}$  has increased the amount of substitutional nitrogen in these layers by allowing interstitial nitrogen to diffuse on to the crystallographic B site of the material, at higher temperatures this effect has been reversed. Increased nitrogen incorporation has resulted in a reduction in the crystal quality of these layers, differing from the effects seen in the homoepitaxial layers.

# Glossary & Abbreviations

a, b, c	Unit cell lattice parameters
$\alpha, \beta, \gamma$	Unit cell angles
ADP's	Anisotropic Displacement Parameters
CCD	Charge Coupled Device
DOE	Department of Energy, (U.S.A)
DSC	Differential Scanning Calorimetry
DTA	Differential Thermal Analysis
FID	Free Induction Decay
FWHM	Full Width at Half Maximum
hkl	Miller indices
HR-XRD	High Resolution X-ray Diffraction
HT-PXRD	High Temperature Powder X-ray Diffraction
LT-PXRD	Low Temperature Powder X-ray Diffraction
MAS	Magic Angle Spinning
MBE	Molecular Beam Epitaxy
MOCVD	Metalorganic Chemical Vapour Deposition
NMR	Nuclear Magnetic Resonance
OPEC	Organisation of Petroleum Exporting Countries
PEM	Proton Exchange Membrane
PXRD	Powder X-ray Diffraction
r.f.	Radio Frequency
RSM	Reciprocal Space Map
SC-XRD	Single Crystal X-ray Diffraction
SIMS	Secondary Ion Mass Spectrometry
TPV	Thermal Photo Voltaic

# Chapter 1

## Introduction

### 1.1 The Hydrogen Economy

In order to create the shift from a fossil fuel based economy to one based on hydrogen, the only real viable alternative, there are several areas where additional research and development is required. [1-2] They can be divided into three main categories:- hydrogen production, supply and storage and hydrogen utilisation. [3]

The switch to a hydrogen based economy is a vast undertaking involving such a fundamental change in the production of energy and changes in how many people from all walks of life utilise it. As well as the very large infrastructure changes associated with the distribution of hydrogen, the current concerns over the mitigation of greenhouse gas emissions are seen as a political issue, which has repercussions for any future hydrogen based economy. Whilst these political issues may prove to be important in the future when the hydrogen economy becomes more established, they are not something this thesis aims to address and are beyond the scope of the work discussed herein.

#### 1.1.1 Non Renewable Hydrogen production

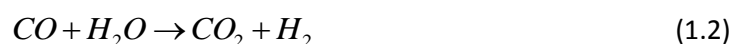
##### **Natural Gas Reforming**

Currently the vast majority of commercial hydrogen is produced through the process of steam natural gas reforming (95% USA). In this process the methane present in natural gas is reacted with high temperature steam (700°C-1000°C) [4] at a pressure of 3-25 bar, in the presence of a catalyst, to produce hydrogen gas and carbon monoxide (equation (1.1)). Similarly the process can utilise other common fuels such as ethanol and propane, in each case the by-product of the reaction is carbon monoxide.



Inevitably this carbon monoxide will react to form carbon dioxide. In order to extract additional hydrogen the carbon monoxide is further reacted with high temperature steam to form hydrogen and carbon dioxide as described below.





Whilst this process can produce a near pure source of hydrogen, which is important for use in hydrogen fuel cells to avoid contamination of the component parts of the cell, there are limitations to this method of production. Chiefly this process is still dependent on the use of fossil fuels and the associated release of greenhouse gases, which a switch to a hydrogen based economy is set to mitigate. In addition to this, the process requires vast amount of thermal energy, not only to heat the steam but also to maintain the reaction in equation (1.1). This reaction is endothermic and whilst the additional water-gas shift reaction, equation (1.2), is exothermic, the net effect is still endothermic.

### **Partial Oxidisation**

The other commercial method of producing hydrogen from natural gas products is partial oxidation, which avoids many of the energy requirements of steam natural gas reforming by limiting the need for high temperature steam as well as relying on an initial reaction that is exothermic, (equation (1.3)). Similarly to the above reaction, it is possible to use other fuel sources in this process such as ethanol or propane.



At this point, the water-gas shift reaction, equation (1.2), is again used to recover additional hydrogen and it is here that high temperature steam is required. Whilst this reaction pathway is typically faster than natural gas reforming, by examining equations (1.1) and (1.3), it can be seen that the initial reaction produces less hydrogen per unit of fuel. Again this method of hydrogen production is limited by its reliance on fossil fuels and the release of the greenhouse gas carbon dioxide.

These processes have the advantage that the infrastructure associated with their use is already in place and well established. [5] Using this hydrogen in a fuel cell can reduce the amount of greenhouse gas emission by up to 50% when compared to the use of petroleum in internal combustion engines (ICE). [6] However, they are not seen as a viable long term solution to hydrogen production needs as the cost of the hydrogen produced in this manner is deemed to be too high when compared to traditional fuels. In addition to this, the amount of natural gas and other potential input fuels is considerably restricted because of dwindling reserves and the demand from primary users of these fuels for heating and

electricity production. In the future the switch to a 100% hydrogen-based economy will involve these activities being moved to a hydrogen, or renewable energy, based system.

One possible solution to this problem of supply of natural gas and the release of greenhouse gases would be to use biomass as the source of methane for the reaction; this would mitigate the greenhouse gas emissions as the process would become essentially carbon neutral. Whilst in theory there is no limit on the supply of biomass it would increase the overall cost of the hydrogen produced even further to the point where, at least for now, it would not be able to compete with other fuel sources. It is because of this that this area is not actively pursued, as there are considered to be more efficient methods of producing carbon neutral hydrogen.

#### 1.1.2 Greenhouse Gas Free Production

One of the most advanced alternatives for hydrogen production is high temperature (500°C-2000°C, depending on the exact method used) water splitting. [7] It is obvious that the largest supply of potential hydrogen on the planet is that locked up in water, and so this research area has attracted significant interest. Splitting the water into its constituent parts would offer a limitless supply of hydrogen fuel as when this hydrogen is burnt, either in an ICE or a fuel cell, the resulting product would simply be water, and the process cycle begins over again. This illustrates a common misconception in this area about the distinction of the nature of hydrogen as a fuel, namely, unlike when considering traditional fuels, hydrogen is an energy carrier and not an actual source of energy in its own right. In the example of high-temperature water splitting, the source of the energy is whichever method is used to heat the water used for splitting. If this energy is supplied from an existing fossil fuel based source, there is very little advantage to this method of production as it is still reliant on fossil fuels and releases greenhouse gases. It is for reasons such as these that it is not possible to see the hydrogen economy as a single entity that will provide of the world's energy needs into the future. It is just one area that has to be used in conjunction with others to provide an overall renewable energy future, which will allow for the dramatic reduction in the reliance on fossil fuels and mitigate the greenhouse effect. To this end the main focus of the research in this area is to develop other ways to produce the energy to heat water into superheated steam. The two main areas are nuclear power and solar concentrators which both have the ability to provide the energy to perform such a task.

Another method of splitting water is electrolysis, which has the added advantage that it fits neatly with the scope and power produced by many renewable sources of electricity such as solid state solar power and wind turbine electricity production. [8] The electrolysis of water from these sources into hydrogen and oxygen can be extended further as a battery of sorts that can store excess energy in the form of hydrogen, which can then be used to supplement supply at the time it is needed.

The electrolysis process is essentially the reverse of the process in fuel cells, which produces electricity from the controlled oxidation of hydrogen. Therefore, the ideal solution would be to use the same technology for both the production of hydrogen and the utilisation of hydrogen to produce electricity. Such technology can then be easily scaled to suit the needs of the end user, whether that is the individual household or for city wide power/hydrogen production. [9] In this scenario the hydrogen is used as a store of energy as well as a supply to be used elsewhere. For example, in combined heat and power units or to be transferred for on-board storage in automobiles for the powering of onboard engines, either ICE's or more likely specially designed fuel cells adapted to these conditions.

These initiatives show that in the area of hydrogen production there is a wide range of different approaches being examined with the hope of reducing and eliminating the need for fossil fuels as both the source of hydrogen and the source of energy for the production of hydrogen. It is clear that the development of these production methods go hand in hand with the development of renewable energy sources, which are required to produce the energy needed to manufacture hydrogen, in most cases in the form of electricity.

### 1.1.3 Hydrogen Supply and Storage

Many of the production methods detailed here require the centralised production of hydrogen, which then has to be distributed to where it is needed and stored locally before it is either transferred to other storage media or used to produce power. Much of this infrastructure including pipeline, trucks, high pressure storage tanks and cryogenic storage systems already exists and is used for both the storage and transportation of the existing supply of hydrogen, which is used mainly in refining oil products and the production of ammonia for fertilizer. [10] There are several major hurdles that have to be overcome to be able to distribute the expected volumes that a switch to a hydrogen based economy would demand. One of the most promising distribution paths for this hydrogen would be to utilise the natural gas pipelines which have already seen significant development and

implementation within modern power distribution network. [11] Pipelines are seen to be the most efficient method to distribute hydrogen given its low volumetric energy density although specific problems need to be overcome before the widespread implementation of this system. These include the potential of hydrogen to affect the steel these pipes are made from and the welds used to join them together as pressurised hydrogen can be absorbed by steel, rendering it brittle and more susceptible to fracture and failure. As well as this, there is the need to control the loss of hydrogen from these pipes, not only from leaks but also from the penetration of the hydrogen into the steel, resulting in losses via solid-state diffusion. [10, 12]

Other hydrogen delivery systems use hydrogen stored in the conventional way, either as a compressed gas in cylindrical steel tanks or composite tanks, which can operate up to a pressure of 350 or 700 bar, respectively, or in cryogenic storage systems that store liquefied hydrogen below  $-253^{\circ}\text{C}$  in insulated tanks. Whilst both of these systems can be installed into specially-designed trucks for delivery purposes, they both have disadvantages. Carrying hydrogen as a compressed gas can be expensive to implement and the cost can be prohibitive over long distances. [10] High-pressure tanks have to be substantial enough to contain the pressure of their contents:- this makes them heavy and adds to the overall cost of the vehicle and the fuel costs. Liquid hydrogen has an associated energy cost because of the liquefaction process, which is up to 30% of its energy content. Also the losses from the evaporation of the hydrogen during transit have to be accounted for, especially if smaller tanks are used as they have a larger surface area to volume ratio. This method of delivery does, however, have an advantage over compressed gas as a higher density of hydrogen can be carried. [10]

As mentioned above, these hydrogen supply solutions are only needed if hydrogen production is centralised, to take advantages of economies of scale. However, many of the production methods described have the ability to be used in a de-centralised infrastructure, which would help negate the need for large-scale hydrogen supply solutions as hydrogen would be distributed more locally.

#### 1.1.4 On-Board Hydrogen Storage

The storage methods discussed above are considered adequate for stationary storage of hydrogen. Continued development of these storage methods has focussed on improving the storage capabilities given that in most cases, limited space is not a critical factor so that

the low volumetric density of these methods, Figure 1.1, is outweighed by their convenience and reliability. There is one major area where this is not the case, i.e. on-board storage of hydrogen for use in automobiles, where space and weight-load are at a premium. This is considered one of the last major hurdles before the widespread implementation of hydrogen as the fuel source for motive power within the automotive industry.

There two newer areas of storage methodology that have the potential to provide the solution to improved volumetric and gravimetric densities of hydrogen storage, other than major improvement of existing technologies such as high-pressure tanks and liquid storage. These are *physically bound hydrogen* and *chemically bound hydrogen*, which have the potential to provide the required gravimetric and volumetric densities for a feasible on-board storage system. They also offer safety advantages over the use of high pressures or extremely low temperatures as they would ideally operate at ambient pressures and temperatures. [13-14]

#### **Physically-Bound Hydrogen Storage**

This method of storage relies on physisorption of hydrogen gas onto a surface, where the diatomic hydrogen molecule is held on the surface by weak van der Waals interactions. The low strength of these interactions means that the hydrogen molecule's thermal energy has to be reduced so as not to overcome the van der Waals force. This requires, therefore, that the systems are cooled, which adds an extra complication to the technology and also results in a net reduction of their energy efficiency. Despite this, there is still an energy saving over a liquid hydrogen storage system because the cooling required here is not to cryogenic temperatures. The porous materials (giving large surface areas) used in these systems have excellent reversibility of adsorbing/desorbing of hydrogen as the material itself is not permanently affected by the process. The weakness of the van der Waals forces make it easy to desorb the hydrogen from the surface although additional thermal management is needed to adsorb hydrogen in a reasonable amount of time. [10]

#### **Chemically-Bound Hydrogen Storage**

Chemically-bound hydrogen is seen as a more appropriate alternative to physically-bound hydrogen systems for on-board hydrogen storage as there are no cryogenic systems involved, which increase the overall weight of any on-board system as well as reducing the volumetric efficiency of any design.

Chemically-bound hydrogen can be further split into two different regimes; metal hydrides, and complex metal hydrides, which cover many systems such as borohydrides, amides and alanates. In order to maximise the gravimetric density of these systems, the metals used are normally light. Current research concentrates on non-transition metals with atomic weights less than 40a.u. This narrows down the choices for these systems to metals such as lithium, magnesium, sodium and potassium. Although beryllium also falls into this range, its toxicity is seen as an additional difficulty, which precludes its use.

The simplest form of hydrogen storage is summarised in equation (1.4) where M represents any appropriate metal which will form a hydride in a reversible reaction. [14]



In these cases, the forming of the hydride is an endothermic reaction and, conversely, desorption of the hydrogen is exothermic. In order to control the reaction and the rate of release of hydrogen, either an increase in temperature or reduction of the pressure is required. Unfortunately, the metals that are best suited to a reasonable temperature and pressure range for on-board storage, around 80°C and 1 bar, respectively, are heavy transition metals, which offer low gravimetric storage capacities. [10] Other hydride and complex metal hydrides offer higher gravimetric capacity (figure 1.1) but require higher temperatures to initiate hydrogen release. Because of this, research has focussed on the development of new complex metal hydrides, which offer the properties that are required for hydrogen release under reasonable conditions but still have acceptable hydrogen storage densities. Another area of research is into the effect that the mixing or destabilising of these current hydride materials has on the temperatures and pressures that are needed for hydrogen release. Further to these considerations, there are other properties of potential materials that have to be fulfilled, such as the reversibility of the appropriate reactions and their response to repeated cycling.

#### 1.1.5 Hydrogen Utilisation

As alluded to earlier, by far the most common hydrogen-fuelled device is a fuel cell. In its simplest terms, a fuel cell takes diatomic hydrogen and, using a catalyst, splits the molecule into ionised hydrogen, protons, which then react with similarly ionised oxygen in a controlled manner. Simultaneously, the electrons associated with the reaction are diverted via an external circuit in the form of an electrical current. The structure of a fuel cell consists of an electrolyte sandwiched between electrodes; a cathode and anode, at which

points, the oxygen and hydrogen are ionised, respectively. Suitable membranes allow only the ions and not the electrons through into the electrolyte, where the chemical reaction takes place. Conductive contacts on the electrodes carry the electrons from the anode to the cathode through the external circuit that is going to utilise the supply. The hydrogen-oxygen reaction is exothermic and the excess heat created can be used for other applications: - in the case of solid state hydrogen storage, this heat can be used when desorbing hydrogen from the material, thus increasing the overall efficiency of any combined system. There are various types of fuels cells each of which have specific properties that are desirable for different applications. This, along with their capability to be stacked to produce greater power output, makes them highly adaptable to tailoring for many applications from power generation for consumer electronics up to commercial power plants. The fuel cell is named after the type of electrolyte the cell uses and this electrolyte determines the kind of chemical reactions that take place as well as the operating temperature range of each cell determined by the optimum permittivity of the electrolyte to the transported ions. Giving an overview of some common fuel cell types along with the properties of each cell (table 1.1) shows that there is a varied range of both operative temperature and power output ranging up to 1000°C and 2MW power. The combination of these two factors leads to the typical applications for each cell.

Fuel Cell Type	Common Electrolyte	Operating Temperature /°C	Typical Stack Size	Efficiency	Applications
Polymer Electrolyte membrane/ Proton Exchange Membrane (PEM)	Perfluoro sulfonic acid	50-100 Typically 80°C	<1-100kW	60% transportation 35% stationary	Backup power Portable power Transportation Specialty vehicles
Alkaline (AFC)	Aqueous solution of potassium hydroxide soaked in a matrix	90-100	10-100kW	60%	Military Space
Phosphoric Acid (PHFC)	Phosphoric acid soaked in a matrix	150-200	400kW	40%	Distributed generation
Molten Carbonate (MCFC)	Solution of lithium sodium, and/or potassium carbonates soaked in a matrix	600-700	300kW-3MW	45-50%	Distributed generation Electric utility
Solid Oxide (SOFC)	Ytria stabilized zirconia (YSZ)	700-1000	1kW-2MW	60%	Auxiliary power Electric utility Distributed generation

Table 1.1 Common hydrogen fuel cells types along with their typical power outputs and working temperatures along with the typical professed applications for each fuel cell. Adapted from [15]

## 1.2 Thermal Photovoltaic Electricity Production

Ultimately the goal of switching to a hydrogen-based economy is to end our reliance on fossil fuels and to curtail the amount of carbon dioxide and other toxins released into the atmosphere. In order to achieve this goal, the production, storage and utilisation of hydrogen is only one of the obstacles to overcome. New ways of producing energy, most usefully in the form of electricity, are required. These production methods will not only complement the hydrogen economy by allowing for clean electricity production, but also this electricity will be used to produce hydrogen using the techniques detailed in section 1.1.2. One obvious answer would be to use nuclear fission power- however, this has its own drawbacks and environmental concerns beyond the scope of this work, and whilst nuclear fusion power is a really possibility in the future, it is many years away from practical implementation. One of the most promising avenues for electrical production is *photovoltaic solar cells*. Research in this area has the target of producing more efficient and more effective solar cells for wide scale, low cost, electrical production. [16-17] One factor hampering the efficiency of photovoltaic cells is that they, by their very nature, are wavelength dependent and can only operate using a narrow band of energies to which they have been tuned. These energies are conventionally in the visible range of the EM spectrum as there is an atmospheric transmission window that allows these wavelengths to reach ground level. There are transmission windows also in the infra-red region that could be exploited in a similar way as long as potential semiconductor materials can be tuned to their specific energies, namely the 2-5 $\mu$ m range. These materials can also be used in a very different way to generate electricity from other sources of heat using additional components to focus and recycle this heat through a suitable semiconductor converter device; the most promising materials to produce these converters are III-V semiconductors such as GaAs and GaSb. [18] Intrinsically these materials have band gap energies outside the usable range for these thermal photovoltaic (TPV) devices and, therefore, methods to reduce the band gap of these materials and tune them to specific energies have been developed. One of the methods used is anion substitution i.e., replacing the constituent anions with atoms that are more electronegative, for example, nitrogen. Nitrogen substitution reduces both the lattice parameters of the material and the band gap energy because of the perturbation in the electronic potential surrounding the small, highly electronegative anion-substituted atom within the host crystal structure. [19-20] Modelling the effects of nitrogen substitution with respect to variations in the growth conditions allows tuning of the growth to produce materials with properties tailored for specific



applications. These materials can then be used in TPV arrays to produce efficient clean electrical energy, which can then be either used directly or to produce hydrogen.

### 1.3 Literature Review

There has been much interest in hydrogen since it was isolated in the 1700's by Henry Cavendish. A further milestone in the development of hydrogen came in 1839 when Sir William Robert Grove shows that hydrogen could be isolated from water using electrolysis and that if the process was reversed, the hydrogen could be used to produce, or rather release, energy. He also demonstrated using one of the first prototype devices, which would later become known as a fuel cell. In the 1970's, there was renewed interest in hydrogen as an energy carrier to enable the switch to a hydrogen-based economy in an attempt to relieve societies' dependence on fossil fuels and oil imports. This was kick-started by the landmark work by Gregory et al. [21], which showed that hydrogen had the potential to distribute energy over large distances more efficiently than other methods. From there, the roadmap of a hydrogen economy was developed, which was described as the use of hydrogen to transport energy from renewable sources over large distances and to store it in large amounts for use in one of two ways: (1) in fuels cells to produce electricity; (2) burned with oxygen to produce heat as an alternative to natural gas. [22] This description is still accurate today and has been the goal of this field of research ever since. As this description shows, even from the beginning, there has been the understanding that both technologies for the use of hydrogen and for the development of new renewable energy sources are necessary. It is no coincidence that these ideas first started to surface at the same time as the oil embargo after the formation of the Organisation of Petroleum Exporting Countries (OPEC), when the security of oil supply was in question. Originally, the purpose of the switch to hydrogen-based instead of carbon-based activities was to secure continued supply of energy, with hydrogen being the 9<sup>th</sup> most abundant element of earth, although almost all of it is contained as water, or reacted with carbon in hydrocarbons. At an early stage of this development, the US government through the Department of Energy (DOE), entered the area to offer guidelines and incentives to aid research that would lead to developments crucial to the implementation of a hydrogen-based economy. In addition, to coordinate research efforts initially throughout the USA but more recently throughout the wider world, the DOE has taken membership of international organisations such as the International Energy Agency and

International Partnership of Hydrogen and Fuel Cells in the Economy. [23] This international involvement has led to the DOE being a major influence worldwide on the development of the technologies involved through the grants it awards to research agencies. The DOE, in the guise of the Fuel Cell Technologies Program, has set out various areas that require research; broadly speaking, they follow the areas set out in section 1.1 – hydrogen production, delivery, storage and fuel cells for utilisation. However, in addition to this, they have actively helped to develop manufacturing techniques and codes of practice with regard to safety and standards, which are sometime overlooked, but still vital to any implementation of the research into the hydrogen economy. One of the main areas where the DOE targets have been adopted worldwide are the targets it releases for the development of on-board hydrogen storage. Since first being published, these targets have been revised to take into account the current rate of research and development. They continue to offer achievable goals for the research effort in this field in an attempt to continue the impetus and momentum gained over the decades since the DOE first saw the need for a switch to a hydrogen-based economy.

#### 1.3.1 Targets for On-Board Hydrogen Storage

As a result of both the challenges of on-board hydrogen storage and its unique position as the final stumbling block to the long-term large-scale implementation of hydrogen-based transport, this area has received extra attention from the DOE, who have set target for the development of these technologies. These targets cover many areas specifically associated with the use of the necessary materials in automotive vehicles, the aim being that working towards these targets will enable the phased introduction of hydrogen-based vehicles. A summary of the most recent targets is given in table 1.2. In addition the DOE has stipulated that any storage system must comply with these targets at the end of its service life, which it defines as 1500 cycles or 5000 operation hours.

Target Parameter	2010	2017	Ultimate
System Gravimetric Capacity ( $\text{kWh kg}^{-1}$ )	1.5 (4.5 wt% $\text{H}_2$ )	1.8 (5.4 wt% $\text{H}_2$ )	2.5 (7.5 wt% $\text{H}_2$ )
System Volumetric Capacity ( $\text{kWh l}^{-1}$ )	0.9 (0.028 $\text{kg H}_2 \text{l}^{-1}$ )	1.3 (0.040 $\text{kg H}_2 \text{l}^{-1}$ )	2.3 (0.070 $\text{kg H}_2 \text{l}^{-1}$ )
Min/max Operating Ambient Temperature ( $^{\circ}\text{C}$ )	-30/50	-40/60	-40/60
Min/max delivery temperature ( $^{\circ}\text{C}$ )	-40/85	-40/85	-40/85
Operational cycle life	1000	1500	1500
System Fill time, 5kg $\text{H}_2$ , (minutes)	4.2 (1.2 $\text{kg H}_2 \text{min}^{-1}$ )	3.3 (1.5 $\text{kg H}_2 \text{min}^{-1}$ )	2.5 (2.0 $\text{kg H}_2 \text{min}^{-1}$ )

Table 1.2 DOE targets for onboard hydrogen storage systems for light-duty vehicles [24]

It is important to note that the values of capacity given in table 1.2 are quoted for the entire storage system not just the storage medium used. Currently very few of the materials being investigated have been turned into viable complete storage solutions as many details have to be finalised, such as how these materials will be heated to stimulate hydrogen release and how the system will be recharged either on-board with integrated heat management or remote from the vehicle. Currently, it is understood that the heat energy required for the release of hydrogen from these materials will be the waste heat produced in the on-board hydrogen fuel cells, which will utilise this hydrogen. The best-suited fuel cell for this application, in terms of power production density and hydrogen usage is a Proton Exchange Membrane (PEM) fuel cell, which has an operating temperature of around  $80^{\circ}\text{C}$ . However, it is possible that other types of fuel cell, or even ICE's, could be used, increasing the possible delivery temperature as these fuel cells operate at higher temperatures (table 1.1). The targets set by the DOE in this area are beyond those currently achievable with the technologies discussed in section 1.1.3 and are specifically designed to advance the development of solid state hydrogen storage solutions (section 1.1.4.) By comparing these targets with the materials in Figure 1.1, which shows some of the current hydrogen storage candidates and existing fuels, it is clear to see that using materials such as these, the DOE targets can be met. However, it is difficult directly to compare these values with the overall DOE system targets given in table 1.2 as the exact configuration of the whole system is not being discussed. It does, however, stand to reason that in general, materials with higher volumetric and gravimetric densities will offer advantages over those with lower densities, regardless of the final system configuration.

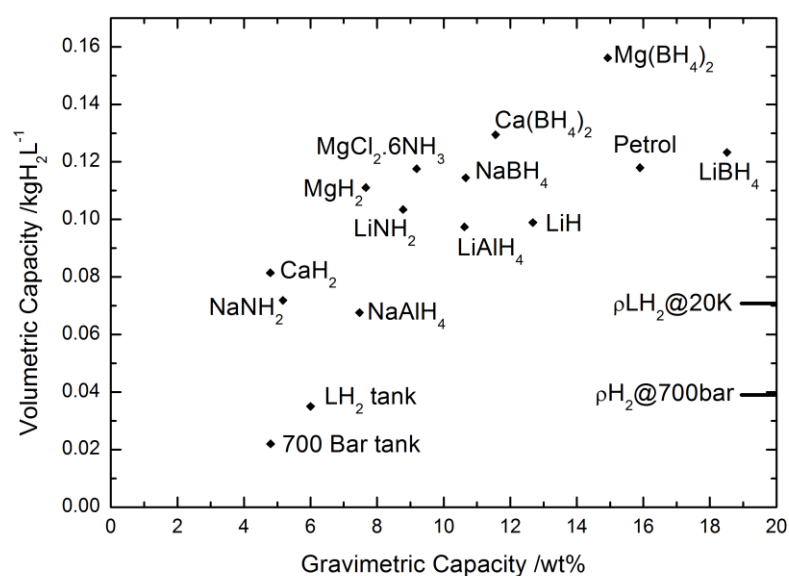


Figure 1.1 the comparison of gravimetric and volumetric densities of many possible hydrogen storage materials along with current liquid storage and 700 bar tanks. For comparison the density of liquid hydrogen and hydrogen at 700 bar have been shown on the right. These clearly have a gravimetric density of 100% adapted from [10]

It is clear from figure 1.1 that many materials have volumetric densities greater than that of current hydrogen storage tanks and cryogenic systems but there are few existing materials that have greater volumetric and gravimetric densities than those specified by the DOE targets. This has helped to encourage researchers to develop new complex materials with more favourable densities. However, other material properties have to be investigated, such as the temperatures required for these materials to release hydrogen and the thermodynamics of the chemical reactions associated with the release and absorption of hydrogen in order to meet the DOE targets for delivery temperature and filling times.

### 1.3.2 Solid State Hydrogen Storage

With the ongoing research into solid state hydrogen storage over the last 4 decades, there has been a large volume of work published on the various potential materials at various stages of development, from initial synthesis [25] to full systems that have demonstrated that they have the potential to provide hydrogen for the automotive industry. [26] One of the definitive review works written on this area was in 2007 by Sakintuna et al. [2]. The review attempts to collate the current state of research into what is seen as the only potential metal hydride system, magnesium hydride,  $\text{MgH}_2$ , and mixtures of  $\text{MgH}_2$  with

other materials, as well as the popular complex hydride systems- alanates, nitrides and borohydrides. This work outlines the rationale for the use of solid state storage over more traditional hydrogen storage methods and expands on the implications of the DOE storage targets for the materials that are reviewed. Sakintuna et al. [27] also present the work that has taken place on  $\text{MgH}_2$  in order to try and improve the kinematics of desorption e.g. much work on the effect of ball milling is presented. Many groups have investigated the effect of ball milling of samples with varying success. In the main, ball milling increases the surface area of the samples investigated, which has been shown to decrease the desorption times required [27]. This is encouraging as whilst the reactions are not constrained to the surfaces of the materials, the desorbed hydrogen relies on diffusion through the material and reducing this diffusion length thus speeds up the release of hydrogen. However, there is a word of caution when examining the effect of ball milling- whilst this reduction may be seen during the first desorption and re-absorption cycle, it cannot be guaranteed to have the same effect in subsequent cycling. As the material is cycled, it has a tendency for the grain size to grow to the point where the material has re-grown to its un-milled morphology. [28] They emphasise some important aspects of the development that are sometimes overlooked such as the effect of cycling and the experimental percentage of hydrogen that can be practically desorbed from these mixtures. Various popular, light weight borohydride materials such as those based on lithium and sodium have been investigated as they have favourable gravimetric hydrogen density percentages, as well as being relatively inexpensive and abundant; a 2009 review has focussed on sodium borohydride storage systems [29] and concluded that there is more research to be performed to improve the hydrogen desorption characteristics of this material such as the temperatures involved and the by-products created. The works presented above offer a starting point to examine the current level of research that is being conducted on a wide range of potential storage materials and shows areas where further work is required to improve all aspects of on-board hydrogen storage.

The work conducted by Somer et al. [30], which was published in mid-2011 (well after the research reported in this thesis was started), is typical of the type of research that is published in the area of complex hydrides. They investigated what materials were formed by the mixing of two or more existing hydride materials together in different molar ratios. This method has proved that it is possible to produce new, previously un-reported, complex hydride materials. [25, 31-32] From this starting point, the materials isolated are examined for both their crystal structure and desorption characteristics. Whilst most published work

includes investigations of both of these properties, it can vary enormously in the level of detail that is included. Unusually, Somer et al. have included comprehensive detail in both areas, which is useful for further structural work and for examining the desorption pathways that the material takes to liberate hydrogen. Not only has the crystal structure of the high-temperature (HT) phase been determined through powder XRD and vibrational spectroscopy, they have identified an additional low-temperature (LT) polymorph of the material. They report the crystal structure of the LT polymorph and using these structural data, show how the two polymorphs are related. Additionally, they deduce how the symmetry of the high temperature phase is broken leading to the low temperature phase. The work also shows that there is a temperature-driven reversible phase change between the two polymorphs and this has provided the basis for Chapter 3 of this thesis. All the relevant data on how the refinements were carried out and the results of each refinement are given clearly and unambiguously. The transition between polymorphs, investigated by differential scanning calorimetry and the XRD patterns associated with each phase, are given. Nevertheless, there are some limitations to their work that require additional attention. Firstly no consideration has been given to any additional low temperature polymorphs that may be present - although these additional phases would have no impact on the performance of the material as a hydrogen storage medium, it is possible that prolonged exposure to cold climates could lead to the formation of these polymorphs and reduce the efficiency of the storage material when it has to be rapidly heated to release hydrogen for use on the start up of any device. Additionally, whilst there is some temperature-dependent XRD analysis, it is very limited with no diffraction data collected across the phase transition temperature. Discussion of the phase change and its reversibility is also limited with little discussion as to why there is a discrepancy observed between heating and cooling. Finally, Somer et al. include no data on the thermal expansion of either of these polymorphs, which would be vital if this material was used as a storage material as its interaction and compatibility with other materials at different temperatures has then to be considered. This assessment is typical of many of the published works in this field- many groups have focused on the headline results such as percentage hydrogen content and desorption temperatures, whilst important additional information about the operational parameters of these materials is neglected.

### 1.3.3 Band Gap Narrowing

Many theoretical studies have shown the effect of doping on the band gap of III-V semiconductors. [33-34] In most cases, a reduction in the band gap is desirable as it allows for longer wavelengths to be accessed. Most work in this area concentrates on narrowing band gaps such that they can be used in electronic devices as infrared detectors. However, in addition this, modified semiconductor devices can be used as part of thermal photovoltaic cells to produce electricity in new ways. As well as the theory of band narrowing, work has been carried out on the growth of various dilute nitride containing layers. The technique that is focused on for the majority of this work is plasma-assisted molecular beam epitaxy (MBE), which is used to grow nitrogen containing layers on various suitable III-V substrate materials either homoepitaxially or heteroepitaxially. Other techniques can also be used, such as metalorganic chemical vapour deposition, MOCVD, [35] although ultimately, whichever technique is used, the morphology of the samples aims to be consistent between techniques. The majority of the work performed on III-V semiconductors has been on GaAs because of its physical properties and wide range of applications. [36] A suite of techniques has been used to characterise these materials, including optical absorption measurements to determine band gap energies, high-resolution XRD for determining the nitrogen incorporation into the structure of the semiconductor and secondary techniques such as secondary ion mass spectroscopy, SIMS, to verify sample nitrogen concentrations and thicknesses.[37] Further to the work on GaAs the next logical choice is GaSb, which has similar properties to gallium arsenide but has a larger electronegativity mismatch between nitrogen and antimony, larger than most other group V elements. This leads to similar band gap narrowing from smaller inclusions of nitrogen and has the potential to access even longer IR wavelengths. [19, 38] The current thrust of ongoing research is to characterise dilute nitride GaSb films and to relate the growth conditions of the films with their nitrogen incorporation and the band gap energy with the ultimate goal of being able to tune the growth conditions of these materials to specific applications. [39-40] In addition to this other parameters are also important, namely the crystal quality of the grown layer. Adding a mismatched anion to the structure will inevitably reduce the quality of the material, from the increased structural strain, but in order to maintain the optical quality ultimately required, this has to be controlled. Work has shown that annealing the grown samples can improve the crystal quality of the materials by reducing the strain. This annealing has had another unforeseen effect- an increase in the quantity of nitrogen that appears to be incorporated into the structure of

the material. [41] Understanding this annealing and how it improves both the crystal quality and the amount of nitrogen incorporated into the samples is an important step and work is ongoing with regard to GaSb based systems, with some work having already been published based on other III-V materials. [19,37]

## 1.4 Aims of the Present Work

With the continued research and development of new materials for chemical hydrogen storage there have been many materials discovered and investigated to determine their suitability of the purpose of hydrogen storage in terms of storage capacity and reversibility. In this work the crystallography of some of these materials is examined to further the structural understanding of these materials through not only analysis of powder XRD but also, where possible, the use of single crystal diffraction. In addition, complementary techniques, such as nuclear magnetic resonance (NMR) and thermal analysis are used to confirm the local structure and the critical temperatures for any structural phase transitions, phase changes and thermal decomposition. Powder XRD is also employed to examine the behaviour of these materials as a function of temperature as it is clear they will be subjected to temperature variations across the operating range (table 1.2). Further to this, attempts to reduce the desorption temperature of the materials have been performed by destabilising their structure with dopants. By reducing the desorption temperatures, the materials in question will become more attractive for use in hydrogen storage without significantly reducing their storage capacity.

A systematic collection of semiconductor thin-film materials are examined for their nitrogen incorporation and growth quality, along with their growth rates and thicknesses, to fine-tune the specific growth conditions which lead to optimum crystalline growth as well as being able to predict confidently the amount of nitrogen incorporation for given growth conditions. In order to investigate these materials, HR-XRD is employed as a mature and well understood technique for investigating this family of materials. In addition to investigating the growth of these materials, the effect of annealing of these samples has been investigated to increase the understanding of how these materials are grown and to develop ways to improve the quality of the grown layer, as well as the quantity of nitrogen incorporated. Along with HR-XRD to investigate the amount of nitrogen incorporated into the lattice, SIMS is employed to determine the amount of residual nitrogen that is left in



interstitial sites after growth and is not incorporated into the crystal structure of the material. It also determines whether annealing has allowed any interstitial nitrogen to be incorporated in the structure. The aims of this part of the work are twofold: (1) to understand the most effective and reliable ways of incorporating the desired amount of nitrogen into the structure to give the photovoltaic properties required; (2) to increase the quality of the materials grown such that when employed in photovoltaic devices, their efficiency can be optimised.

## References

- [1] P. Tseng, J. Lee, P. Friley, *Energy* **30**, (2005) 2703-2720
- [2] B. Sakintuna, F. Lamari-Darkrim, M. Hirscher, *Int. J. Hydrogen Energy* **32** (2007) 1121-1140
- [3] P. P. Edwards, V. L. Kuznetsov, W. I. F. David *Phil. Trans. R. Soc. A* (2007) **365**, 1043-1056
- [4] A. Heinzl, B. Vogel, P. Hübner, *J. Power Sources* **105** (2002) 202-207
- [5] S. H.D. Lee, D. V. Applegate, S. Ahmed, S. G. Calderone, T. L. Harvey, *Int. J. Hydrogen Energy* **30** (2005) 829-842
- [6] IPHE Renewable Hydrogen Report (March 2011) [www.iphe.net](http://www.iphe.net)
- [7] C. Perkins, A. W. Weimer, *Int. J. Hydrogen Energy* **29** (2004) 1587-1599
- [8] F. Barbir *Solar Energy* **78** (2005) 661-669
- [9] J. I. Levene, M. K. Mann, R. M. Margolis, A. Milbrandt, *Solar Energy* **81** (2007) 773-780
- [10] Walker, G. (2008) *Solid-state hydrogen storage- materials and chemistry*. Cambridge, England: Woodhead publishing, 2008
- [11] D. Haeseldonckx, W. D'haeseleer, *Int. J. Hydrogen Energy* **32** (2007) 1381-1386
- [12] H. Barthélémy, *Int. J. Hydrogen Energy* **36** (2011) 2750-2758
- [13] M. A. DeLuchi, *Int. J. Hydrogen Energy* **14** (1989) 81-130
- [14] B. Sakintuna, F. Lamari-Darkrim, M. Hirscher, *Int. J. Hydrogen Energy* **32** (2007) 1121-1140
- [15] U.S. DOE Energy efficiency & Renewable energy, Fuel cell technologies program. [www1.eere.energy.gov/hydrogenandfuelcells/fuelcells/fc\\_types](http://www1.eere.energy.gov/hydrogenandfuelcells/fuelcells/fc_types)
- [16] A. Pivrikas, H. Neugebauer, N. S. Sariciftci, *Solar Energy* **85** (2011) 1226-1237
- [17] W. Cai, X. Gong, Y. Cao, *Solar Energy Materials & Solar Cells* **94** (2010) 114-127
- [18] T. J. Coutts, *Solar Energy Materials & Solar Cells* **66** (2001) 443-452
- [19] L. Buckle, S. D. Coomber, T. Ashley, P. H. Jefferson, D. Walker, T. D. Veal, C. F. McConville, P. A. Thomas, *Microelectronics Journal* **40** (2009) 399-402
- [20] K. Uesugi, I. Suemune, *Journal of Crystal Growth* **188** (1998) 103-106
- [21] D. P. Gregory, D. N. Long, G. Ng, Editor: J. O'M Bockris, *The electrochemistry of cleaner environments*. New York: Plenum Press, 1972
- [22] J. O'M. Bockris, *Int. J. Hydrogen Energy* **27** (2002) 731-740

- [23] U.S. DOE Energy efficiency & Renewable energy, Fuel cell technologies program. [www1.eere.energy.gov/hydrogenandfuelcells/international\\_activities](http://www1.eere.energy.gov/hydrogenandfuelcells/international_activities)
- [24] Report: Targets for Onboard Hydrogen Storage Systems for Light-Duty Vehicles  
US Department of Energy, Office of Energy Efficiency and Renewable Energy and  
The FreedomCAR and Fuel Partnership. September 2009
- [25] P. A. Chater, P. A. Anderson, J. W. Prendergast, A. Walton, V. S. J. Mann, D. Book, W. I. F. David, S. R. Johnson, P. P. Edwards, J. Alloys & Compounds **446-447** (2007) 250-354
- P. A. Chater, W. I. F. David, S. R. Johnson, P. P. Edwards, P. A. Anderson, Chem. Commun. **23** (2006) 2439-2441
- [26] T. A. Johnson, S. W. Jorgensen, D. E. Dedrick, Faradays Discuss. **151** (2011) 327-352
- [27] J. Huot, G. Liang, S. Boily, A. Van Neste, R. Schulz, J. Alloys & Compounds **293-295** (1999) 495-500
- [28] B. Paik, A. Walton, V. Mann, D. Book, I. P. Jones, I. R. Harris, Int. J. Hydrogen Energy **35** (2010) 9012-9020
- [29] U. B. Dermirci, O. Akdim, P. Miele, , Int. J. Hydrogen Energy **34** (2009) 2638-2645
- [30] M. Somer, S. Acar, C. Koz, I. Kokal, P. Höhn, R. Cardoso-Gil, U. Aydemir, L. Akselrud, J. Alloys Compd. **491** (2010) 98-105
- [31] F. E. Pinkerton, G. P. Meisner, M. S. Meyer, M. P. Balogh, M. D. Kundrat, J. Phys. Chem. Letts. (2005) 6-8
- [32] G. P. Meisner, M. I. Scullin, M. P. Balogh, F. E. Pinkerton, M. S. Mayer, J. Phys. Chem. B **110** (2006) 4186-4192
- [33] V. Panlankovski, G. Kailblinger-Grujin, S. Selberherr, Materials Science and Engineering **B66** (1999) 46-49
- [34] S. C. Jain, D. J. roulston, Solid State Electronics **34** (1991) 453-465
- [35] D. Sentosa, X. Tang, Z. Yin, S. J. Chua, J. of Crystal Growth, **307** (2007) 229-234
- [36] G. Pozina, I. Ivanov, B. Monemar, J. Thordson, T. G. Anderson, Materials Science and engineering **B50** (1997) 153-156
- [37] H. F. Liu, N. Xiang, S. J. Chua, J. of Crystal Growth **290** (2006) 24-28
- [38] T. D. Veal, L. F. J. Piper, S. Jollands, B. R. Bennett, P. H. Jefferson, P. A. Thomas, C. F. McConville et al., Applied Physics letters **87** (2005) 132101
- [39] L. Buckle, B. R. Bennett, S. Jollands, T. D. Veal, N. R. Wilson, B. N. Murdin, C. F. McConville, T. Ashley, J. of Crystal Growth **278** (2005) 188-192

[40] M. J. Ashwin, T. D. Veal, J. J. Bompfrey, I. R. Dunn, D. Walker, P. A. Thomas, T. S. Jones, AIP Advances **1** (2011) 032159

[41] H. F. Liu, N. Xiang, S. J. Chua, S. Tripathy, J. of Crystal Growth **288** (2006) 44-48

## Chapter 2

# Experimental Background & Theory

### 2.1 Introduction

There are many mature scientific techniques that have been utilised to collect the data presented in this work; this chapter will outline some of the principles and concepts behind these techniques. X-ray crystallography, both powder x-ray diffraction (PXRD) and high-resolution x-ray diffraction (HR-XRD) are the main techniques employed and explored here. Additionally, the procedures associated with single crystal x-ray diffraction and the basic theories of the complementary techniques used in this thesis are explained. These techniques include thermal analysis, Nuclear Magnetic Resonance (NMR) and Secondary Ion Mass Spectroscopy (SIMS). As many of the samples examined in this work are air sensitive and have had to be stored, manipulated and mounted for x-ray analysis under an inert atmosphere, details of the glove box used and the methods of maintaining this atmosphere are briefly discussed.

### 2.2 Crystallography

#### 2.2.1. Definition of a Crystal

Crystals are defined as materials with a regular, repeating structure on the microscopic scale. This periodic long range order can be described mathematically as a convolution of a crystal lattice and a unit cell. The lattice is an infinite periodic, 3-dimensional, array of lattice points which can be described by three basis vectors, **a**, **b**, and **c**. Thus any point on this lattice can be defined by a linear combination of these three vectors. The unit cell is defined as the arrangement of atoms which is required to produce the crystal structure when convoluted with the crystal lattice points. The unit cell is described by the lattice parameters  $a$ ,  $b$ ,  $c$ ,  $\alpha$ ,  $\beta$ ,  $\gamma$ . Where  $\alpha$ ,  $\beta$  and  $\gamma$  are defined as the smaller angle between  $b$  and  $c$ ,  $c$  and  $a$ , and  $a$  and  $b$  respectively.

#### 2.2.2 Crystal Systems

There are seven unique Crystal systems each of which has associated symmetry operations which restrict the values the lattice parameters can take. These operators and resultant

lattice parameter restrictions are given in table 2.1. Each of these crystal systems can be applied to different lattices to create a unique arrangement which fills all space. These lattices are Primitive (P), Base Centred (C), Body Centred (I) and Face Centred (F). There are 14 possible combinations, so-called Bravais lattices, of these systems and these are also given in table 2.1. It is important to note that, by convention, there are two ways of defining the lattice parameter restrictions for the trigonal system, which are termed rhombohedral and hexagonal, each with only two definable variables.

Crystal System	Defining Symmetry	Lattice Parameter Constraints	Possible Lattice Centring
Triclinic	None	$a \neq b \neq c$ $\alpha \neq \beta \neq \gamma \neq 90^\circ$	Primitive (P)
Monoclinic	2-fold rotational axis Mirror plane	$a \neq b \neq c$ $\alpha = \gamma = 90^\circ, \beta \neq 90^\circ$	Primitive (P) Base Centred (C)
Orthorhombic	3 perpendicular 2-fold axes 3 perpendicular Mirror planes	$a \neq b \neq c$ $\alpha = \beta = \gamma = 90^\circ$	Primitive (P) Base Centred (C) Face Centred (F) Body Centred (I)
Hexagonal	6-fold rotational axis	$a = b \neq c$ $\alpha = \beta = 90^\circ, \gamma = 120^\circ$	Primitive (P)
Cubic	Four intersecting 3-fold rotational axes	$a = b = c$ $\alpha = \beta = \gamma = 90^\circ$	Primitive (P) Face Centred (F) Body Centred (I)
Tetragonal	4-fold rotational axis	$a = b \neq c$ $\alpha = \beta = \gamma = 90^\circ$	Primitive (P) Body Centred (I)
Trigonal	3-fold rotational axis	$a = b = c$ $\alpha = \beta = \gamma \neq 90^\circ$ (Rhombohedral setting) $a = b \neq c$ $\alpha = \beta = 90^\circ, \gamma = 120^\circ$ (Hexagonal Setting)	Primitive (P)

Table 2.1 The seven crystal systems and the symmetry operations which define these systems as well as the resultant lattice restrictions. By convention, the angles which are not defined are  $<90^\circ$ . Included are the possible lattice centring for each crystal system which creates the 14 possible Bravais lattices in 3-dimensional space.

To describe fully the symmetry of a crystal, the symmetry around a fixed point (point group symmetry) and the translational symmetry (Bravais lattice type) have to be combined. The combination of these symmetries with the addition of other symmetry operators (glide planes and screw axes) results in 230 unique space groups. Further detail about these space groups, point groups, and symmetry operators can be found in the International Tables for Crystallography, Volume A. [1]

### 2.2.3 Powder X-ray Diffraction

The theory of diffraction is well known by scientists in the field and detailed background on the subject can be found in many references. [2-3] Whilst the basic details do not need to be repeated, there are some subtleties that require explaining that are specific to the nature of the samples that are investigated in this work.

The interaction of coherent, monochromatic x-rays with crystalline materials is well understood and therefore x-ray diffraction has become a powerful technique for the identification of new materials and studies of structural phase changes within materials. This is achieved by the simple geometry of diffraction which makes the experiments easy to perform and refinements a comparatively simple process. The ease at which the temperature of the sample can also be controlled makes this a natural extension to the process to allow non-ambient analysis of materials. Given the relatively light elements contained in the samples presented in this work, there is very little x-ray absorption by the sample. As a result of this and the mounting of the air sensitive samples in glass capillaries, the x-ray diffraction can be undertaken in so-called transmission mode. Using this mode removes the need to rely on the para-focusing of the x-rays from a flat sample, as is common in the widely-used Bragg-Brentano reflection mode. A simple diagrammatic representation of both modes is shown in figure 2.1, where it is seen that the primary differences are in the focusing of the x-rays. The x-rays from the incident beam optics in reflection mode are diverging at the goniometer circle and as such will not be focused into the detector without the additional para-focusing off the flat sample. This configuration has the advantage that a large area of the sample can be irradiated and high intensities of x-ray can be focused at the detector. This para-focusing increases the intensity of the diffraction pattern but at the expense of several aberrations that reduce the resolution of the resulting diffraction pattern. A closer look at figure 2.1(a) shows the difference between the flat sample and the ideal shape of the sample, which would lie on the circumference of the focusing circle. This introduces an error in the position of the diffraction peaks in  $2\theta$  as the  $\theta/2\theta$  geometry is not perfect. Additionally, the transparency of the sample has to be considered. If x-rays are able to penetrate deep into the sample, the point at which they diffract and the diffracted beam is detected introduces a height error because the diffracted beam has originated off the focusing circle. This is particularly evident in samples that exhibit low x-ray absorption which have low densities and are made out of, light weight, low Z atoms. To avoid these aberrations, x-ray diffraction in transmission mode can be used. From figure 2.1(b) there is a difference in the focusing of the incident

beam optics in transmission geometry. In this case the x-ray beam at the goniometer circle is not diverging; rather, it is focused on the detector, which is also on the goniometer circle. This circle is centred at the sample, in this case a glass capillary. Whilst it is important that the samples absorption is low in order that the diffracted intensity at the detector is adequate, this attenuation can be controlled by changing the size of the capillary. Conversely though, the diameter of the capillary should be maximised to allow as much as possible sample to be exposed to the beam. There is a trade off between these effects and the samples linear attenuation coefficient has to be taken into account, in conjunction with equation 2.1, when deciding on the appropriate diameter of a capillary

$$\mu \times r \leq 1.5 \quad (2.1)$$

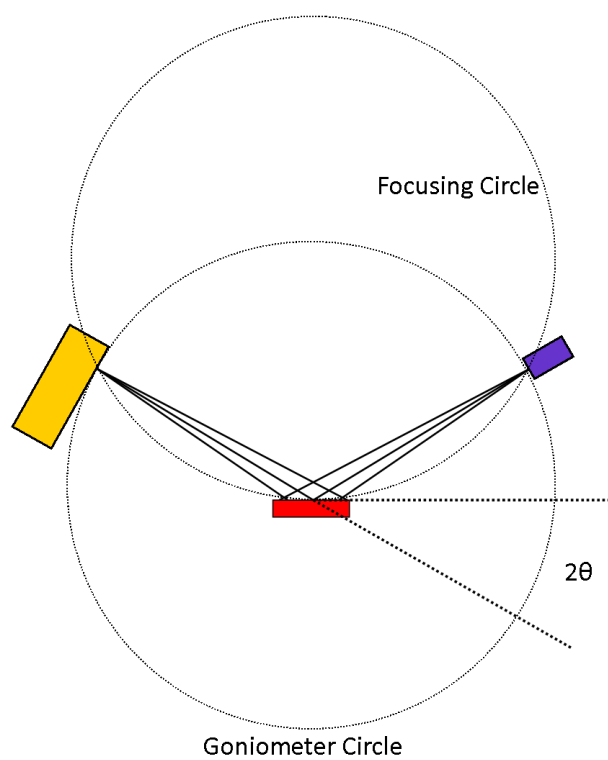
Where  $\mu$  is the combined linear attenuation coefficient of the sample and  $r$  the radius of the capillary. Figure 2.1(b) shows there is a finite size of the beam at the centre of the goniometer circle and that any capillary larger then this would not increase x-ray exposure and would only add to x-ray absorption by the sample. The x-ray absorption in the transmission mode (figure 2.1(b)) is dependent on  $2\theta$  position; as scattered intensity falls off as a function of the angle cubed, it is clear where the value of 1.5 originates in equation 2.1. There are some disadvantages to capillary transmission diffraction as the intensity of the diffraction peak is much lower due to both the amount of sample that is irradiated by the incident beam and the lower intensity of the focused beam when compared to the divergent beam. However the optical system used in transmission mode is easier to align, as well as having fewer variables to consider, with the principal factor of importance being the need to maintain the capillary at the centre of the goniometer circle.

#### 2.2.4 The Rietveld Method

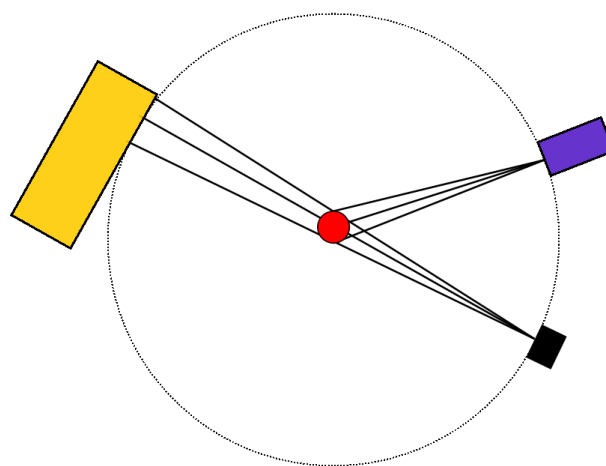
With the proliferation of x-ray powder diffraction and the increased use of computers, methods of modelling x-ray diffraction patterns have been developed. One such method of calculating a diffraction pattern and manipulating this pattern to fit the experimental data is the Rietveld method. [4-5] This is a mathematical algorithm that allows the calculation of the full pattern from a reasonably small set of parameters. There are sample-specific parameters, such as lattice parameters and the atomic arrangement in the unit cell, and profile-specific parameters relating to the diffractometer and the optics used. The principal part of this method, which is common to all diffraction methods aimed at determining crystal structure, is to calculate the diffraction peak positions and intensities from the



lattice parameters, and atomic coordinates respectively. As well as atomic thermal parameters, which define the thermal movement of the atoms in the unit cell. With the samples presented in this work being made of light, low Z, elements these thermal parameters are modelled as anisotropic displacement parameters (ADPs). These ADPs take into account the symmetry of each atomic site when modelling how the atoms are expected to vibrate. This is instead of assuming an isotropic displacement around the atomic position which, as the name suggests, assumes equal displacement around the atomic position in all directions. The ADPs also help define the peak intensities of the calculated profile. In addition, there are other factors which are included in the calculated profile to better fit the experimental data, such as, a polynomial function to describe the background scattering underlying the Bragg diffraction peaks. The calculated emission profile of the x-ray source is defined by the x-ray wavelength and the Lorentz polarisation factor, which is dependent on the type of monochromator used. The x-ray diffraction presented in this work was undertaken using a copper anode to produce x-rays. This defines the wavelength of the x-ray emission profile. The defined emission profile is also dependent on what type of incident beam optics are used as this will determine whether the emission profile will contain both  $\text{CuK}\alpha_1$  and  $\text{CuK}\alpha_2$  radiation or just  $\text{CuK}\alpha_1$  radiation. Along with these parameters there are also  $2\theta$ -dependent peak-shape functions. Finally the peak shape can be manipulated by correcting for the axial divergence of the beam, seen in figure 2.1(a), which has the effect to increase the asymmetry in the low angle side of the peaks, especially evident at small  $2\theta$  angles where this divergence is more pronounced. There are several corrections to the calculated profile, to correct for minor misalignments of the sample or the diffractometer. For example, the height error induced by the sample not being on the focusing circle, (Figure 2.1(b)) and the zero error which is manifest due to a misalignment of the detector with the position of the straight through x-ray beam. This is not trivial to correct mechanically with the diffractometer in para-focusing mode as the straight through, divergent, beam position cannot be defined at the detector. These aberrations and corrections are not needed when considering the Rietveld method as applied to scans collected by the diffractometer in transmission mode. This is a result of the focused beam, the position of which can be easily defined when looking at the straight through beam and results in no axial divergence correction to the peak shape of the scans.



(a)



(b)

Figure 2.1 The optics and geometry of XRD when carried out in (a) para-focusing reflection mode and (b) in transmission mode using a glass capillary. The yellow box represents both the x-ray source and also the incident beam optics which create a diverging beam in (a) and a focused beam in (b). The x-ray detector is represented in purple and all diffraction beam optics have been omitted.

There are several parameters which have to be included in the model when considering diffraction from a sample contained in a capillary; as absorption becomes important in transmission mode, the linear attenuation of the sample is needed along with the diameter of the capillary but as these parameters have known values and the form of the analytical correction has been tabulated (see, for example, International Tables for Crystallography), and they do not contribute additional parameters for refinement in the model. Furthermore, use of a capillary minimises the need for other corrections such as that of preferred orientation, which may be required if the intensity of a specific set of reflections, for example the (00l), are consistently different in the experimental data from those of the calculated diffraction pattern. Preferred orientation can be modelled in the Rietveld method to give the calculated pattern better agreement with the experimental data. However, this must be done with caution as the modelling introduces more refinable parameters into the model, which allows for more degrees of freedom and may simply lead to an improved fit of the calculated pattern to the observed data that has no additional physical meaning. By using a capillary the problem of preferred orientation is reduced in two ways: (1) the capillary can be spun around its axis during the scan thus allowing the x-ray beam access to different crystalline orientations; (2) the size of the capillary means that for any polycrystalline material to be able to fit within it the powder has to be ground very finely thereby tending to reduce, and homogenise, the size of the crystallites that form the sample under investigation.

The purpose of the Rietveld method is to minimise the residual between the calculated profile and the experimentally collected pattern. This is achieved by refining the parameters discussed above in order to minimise the residual,  $S_y$ , which is defined in equation 2.2. [6]

$$S_y = \sum_i w_i |y_i - y_{i(c)}|^2 \quad (2.2)$$

The diffraction pattern is split into  $i$  increments; in the case of angular dispersive diffraction, these increments are in the  $2\theta$  angle. For each point the calculated intensity  $y_{i(c)}$  is compared to the observed intensity  $y_i$  and then weighted by a factor  $w_i$  which is defined as  $1/y_i$  for each  $i$ th increment and then summed over all  $2\theta$ . As discussed above each of the values of  $y_{i(c)}$  are calculated from the sum of the background and any Bragg peak contribution which is appropriate given the position, in  $2\theta$ , of the  $i$ th increment. The

Bragg peak intensity at any given point is defined by the lattice parameters and then modified by other factors given above such as peak shape function and Lorentz polarisation factor. The full description of this intensity,  $y_{i(c)}$ , is given in as:

$$y_{i(c)} = s \sum_n L_n |F_n|^2 \phi(2\theta_i - 2\theta_n) A + y_{b,i} \quad (2.3)$$

Where  $s$  is the overall scale factor of the whole pattern,  $n$  the Miller indices (hkl) of the Bragg reflection,  $F_n$  is the structure factor associated with the reflection described by the Miller indices,  $n$ ,  $L_n$  represents the Lorentz polarization factor and multiplicity of the reflection,  $\phi(2\theta_i - 2\theta_n)$  is the peak shape function,  $A$  is an absorption factor and  $y_{b,i}$  is the contribution from the background.

The method relies on a least squares refinement which changes the variable parameters to minimise  $S_y$ . It is worth remembering that this method requires an existing structural model that is already close to the solution of the structure i.e., a model of the structure that is close to the truth, as Rietveld refinement is not an *ab initio* method of structure determination. The least-squares refinement produces a set of equations that include the derivative of the calculated intensities,  $y_{i(c)}$ , with respect to each refinable parameter, for all  $i$  increments in  $2\theta$ . The solution to the equations is found from the inversion of the normal matrix with elements  $M_{jk}$  defined as

$$M_{jk} = -\sum_i 2\omega_i \left[ (y_i - y_{i(c)}) \frac{\partial^2 y_{i(c)}}{\partial x_j \partial x_k} \left( \frac{\partial y_{i(c)}}{\partial x_j} \right) \left( \frac{\partial y_{i(c)}}{\partial x_k} \right) \right] \quad (2.4)$$

With  $\omega_i = 1/y_{i(c)}$ ,  $x_j$  and  $x_k$  being the adjustable parameters. Given the number of refinable parameters,  $m$ , this produces a matrix  $m$  by  $m$ . The changes in any given parameter,  $x_k$ , are defined as

$$\Delta x_k = \sum M_{jk}^{-1} \frac{\partial S_y}{\partial x_k} \quad (2.5)$$

It is this non-linearity of the method that particularly requires the initial model for the solution to be close to the answer as large difference can lead to divergence of the refinement or lead the refinement into a local minimum thereby giving an incorrect

structural refinement. Small shifts from the initial model are applied to the refinable parameters and the normal matrix,  $M$ , is redrawn, the process repeated until  $\frac{\partial S_y}{\partial x_k} \rightarrow 0$ , thus minimising the value of  $S_y$ . This is the basic least-squares algorithm, which is applied by all Rietveld software programs, although there are slight changes unique to each software package. Some of these changes are designed to prevent the refinement from diverging and to bounce the refinement out of local minimum, for example, by randomising specific parameters on convergence based on the error in their value and then continuing the algorithm. If on this, and subsequent, randomisations the model converges to the same solution it is possible to be confident that the calculated structural model is in the global minimum. In the work presented here the Rietveld software package used was Topas Academic. Further details of this software can be found elsewhere [7].

#### 2.2.4.1 Peak Shape

From the discussion of the Rietveld method it is clear that the peak shape function plays an important role when refining a structural solution. Therefore the choice of an appropriate peak shape, which best fits the experimental peak shape, is important. The appropriate peak shape for the constant-wavelength angle-dispersive diffraction carried out in this work is a mix of Gaussian and Lorentzian distributions. For more unusual types of diffraction experiment, such as time of flight neutron diffraction, other more sophisticated peak shapes are used e.g. with exponential leading and trailing edges. With appropriate definition of the instrumental peak-shape profile it is possible to infer information about the crystallite size and strain diffraction peak-profiles. However, it is more typical to rely on modifications of analytical peak shape functions embedded in the Rietveld software packages as it is frequently difficult to define adequately the instrumental peak shape given the complicated incident beam optics associated with many diffractometers. The peak shape functions available in Topas Academic are defined in table 2.2. As table 2.2 shows these peaks have variable parameters that define the peak, including its variation with  $2\theta$  angle and some of these are refinable in Topas. In addition to the peak-shapes shown in table 2.2, other modifications can be made to the PearsonVII and the Pseudo Voigt, both of which can be split and defined separately for each side (low-angle and high-angle) of the peak. In principle, this method allows for any asymmetry of the peak shape to be accounted for.

Peak Shape Function	Definition
Gaussian	$G(x) = \left( \frac{2\sqrt{\ln(2)/\pi}}{FWHM} \right) \exp\left( \frac{-4\ln(2)x^2}{FWHM^2} \right)$
Lorentzian	$L(x) = \left( \frac{2/\pi}{FWHM} \right) \frac{1}{\left( \frac{1+4x^2}{FWHM^2} \right)}$
Pseudo Voigt	$F(x) = \eta L(x) + (1-\eta)G(x)$
2θ dependence of the Peak	
Pseudo Voigt	$FWHM = \textcolor{red}{h}a + \textcolor{red}{h}b \tan \theta + \textcolor{red}{h}c / \cos \theta$ $\eta = \textcolor{red}{l}ora + \textcolor{red}{l}orb \tan \theta + \textcolor{red}{l}orc / \cos \theta$
Modified Thompson-Cox-Hastings (TCHZ)	$FWHM = \left( \Gamma_G^5 + C_1 \Gamma_G^4 \Gamma_L + C_2 \Gamma_G^3 \Gamma_L^2 + C_3 \Gamma_G^2 \Gamma_L^3 + C_4 \Gamma_G \Gamma_L^4 + \Gamma_L^5 \right)^{0.2}$ $\eta = C_5 \left( \frac{\Gamma_L}{FWHM} \right) - C_6 \left( \frac{\Gamma_L}{FWHM} \right)^2 + C_7 \left( \frac{\Gamma_L}{FWHM} \right)^3$ $\Gamma_G = \sqrt{\textcolor{red}{U} \tan^2 \theta + \textcolor{red}{V} \tan \theta + \textcolor{red}{W} + \textcolor{red}{Z} / \cos^2 \theta}$ $\Gamma_L = \textcolor{red}{X} \tan \theta + \textcolor{red}{Y} / \cos \theta$

Table 2.2 Definitions of two of the peak shapes used in Topas Academic and other Rietveld refinement programs. The two peak shapes have very different dependence on the peak position, 2θ. The refinable variables, which are used in the Rietveld Method, for each of the peaks are highlighted in red. [8]

#### 2.2.4.2 Goodness-of-fit parameters

In addition to the value of  $S_y$  which is minimised by the least square fitting of the Rietveld algorithm there are several calculated indicators that gives the user an idea of the quality of the refinement and how well the structural model has reproduced the experimental diffraction pattern. Examination of these values helps identify not only whether the refinement is stuck in a local minimum but also if the initial structural model used in the refinement is correct. A selection of these ‘R-values’ are given in table 2.3. One additional parameter to keep in mind when examining the results of any refinement is the goodness of fit parameter,  $\chi^2$ , defined as  $wR_p/R_{\text{exp}}$ . This value should never be below 1 as this would imply that the refinement is trying to extract more information from the

experimental pattern than is present in the data. The R-expected and weighted R-factor have analogous, background-corrected expressions which take into account the value of the background at each of the increment positions. The R-expected value is a measure of how well one can expect the data to be fitted by the refinement given the number of parameters and the number of increments. This  $R_{\text{exp}}$  value can become unrealistically small when dealing with high-resolution powder diffraction scans as, in these cases, the number of increments,  $i$ , increases in a manner not described correctly by the statistics. The  $R_{\text{Bragg}}$  value describes how well the intensities of the extracted Bragg reflections from an individual phase within the pattern are modelled. This becomes increasingly important as the number of phases within the pattern increases especially where peaks from different phases overlap. If there are phases within the pattern which are not modelled in the refinement then the other R-values will become larger whereas the  $R_{\text{Bragg}}$  value will not change as it is phase specific.

Fit Parameter	Definition
R-Expected	$R_{\text{exp}} = \sqrt{\frac{i - m}{\sum_i w_i y_i^2}}$
Weighted R-Factor	$R_{\text{wp}} = \sqrt{\frac{\sum_i w_i (y_i - y_{i(c)})^2}{\sum_i w_i y_i^2}}$
R-Bragg	$R_{\text{Bragg}} = \frac{\sum_k  I_k - I_{k(c)} }{\sum_k I_k}$
Goodness-of-fit	$GOF = \chi^2 = \frac{R_{\text{wp}}}{R_{\text{exp}}} = \sqrt{\frac{\sum_i w_i (y_i - y_{i(c)})^2}{i - m}}$

Table 2.3 A selection of the “R-values” which give an indication of the quality of the fit in Rietveld refinement. Many of the variables have been previously define with the exception of  $I_k$  and  $I_{k(c)}$  which are the observed and calculated intensities of the kth reflection. [8]

### 2.2.5 High resolution x-ray diffraction

In high-resolution x-ray diffraction (HR-XRD), the aim is to examine in detail the characteristics of diffraction peaks from single crystal samples or epitaxial films. This is commonly undertaken by investigating  $\omega/2\theta$  rocking curves and reciprocal space maps (RSM's). Within this thesis, HR-XRD is used to determine various parameters of layered samples: here, the layers in question are GaNSb grown on both GaSb and GaAs substrates and InNSb grown on InSb. HR-XRD allows for both out-of-plane (symmetric) and in-plane (asymmetric) scans to be performed around the corresponding reciprocal lattice points. These scans allow for the out-of-plane and in-plane lattice parameters of the crystal structure to be calculated. Whilst a reciprocal space map (RSM) is required to calculate the in-plane lattice parameter, the type of scan that is required to determine the out-of-plane lattice parameter is dependent on the relaxation of the layer atop the substrate. If the relaxation of the layer is known, then only a rocking curve (RC) is required. If the layer is assumed to be 100% strained on the substrate then the in plane lattice parameters of the layer will be the same as those of the substrate.

The high resolution diffractometer used during this work is a PAN'alytical MRD diffractometer utilising a high-power copper anode x-ray source producing  $\text{CuK}\alpha$  radiation produced using a high tension circuit operating at 45kV and an electron current of 40mA. Figure 2.2 shows a schematic representation of the diffractometer. There are three main components to the diffractometer; the source and incident beam optics, the sample stage, and the diffracted beam optics and detector. The incident beam optics consists of a hybrid monochromator, using four germanium crystals each cut to the 220 plane. This produces  $\text{CuK}\alpha_1$  ( $\lambda=1.5406\text{\AA}$ ) monochromatic x-rays, with less than 0.1% intensity of  $\text{CuK}\alpha_2$  radiation, and also focuses the x-ray beam to increase the intensity of the incident beam with only a small reduction of the resolution that would be expected from a dedicated four-bounce monochromator. The footprint of the x-ray is set to be narrow in the horizontal direction to maintain the high resolution of the diffractometer and is set wide in the vertical direction to maximise intensity by irradiating as much of the sample as possible. The diffracted beam optics consist of a triple-axis (referring to a third crystal in the beam path after the traditional 2 crystals used in a monochromator) three-bounce analyser crystal, which reduces the angular acceptance of the diffracted beam into the detector thereby further increasing the resolution of the experiment and allowing for more precise determination of both the straight-through beam and the diffracted peak positions. This small angular



acceptance reduces the need for collimating slits as the analyser crystal will not accept divergent x-rays from the sample, thereby also reducing the background count rate.

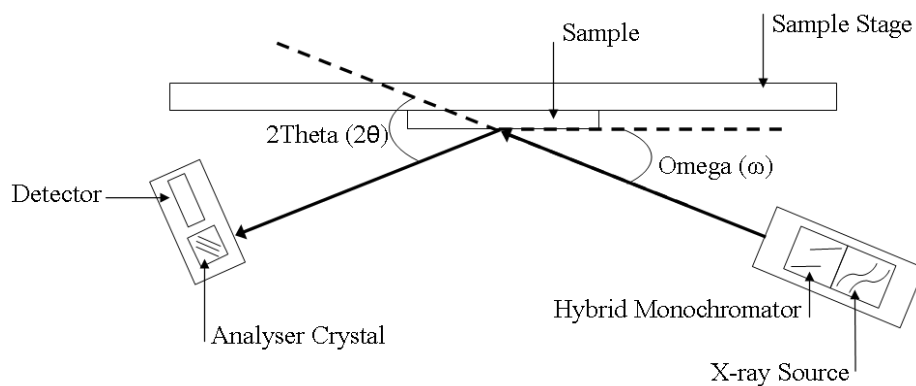


Figure 2.2 The arrangement of the various components which make up the HR-XRD diffractometer used in this work. The diffractometer is used in reflection mode which reduces the number of lattice points which can be accessed but allow for easier alignment of the crystal as well as greater diffracted intensity from the layer.

The sample stage has five degrees of freedom, each of which can be independently set in such a way that the sample is always co-axial with the omega axis. The arrangement of these five axes is shown in figure 2.3. The values of x and y are set such that the sample is in the optimum position relative to the x-ray beam, giving the maximum diffraction intensity from the sample. The z-axis is set so that the height of the sample i.e. the position of the outward-facing surface of the sample is in the half-cut position of the beam. The resolution of these axes, x, y and z are 0.01mm, 0.01mm and 0.001mm respectively. The other two axes are phi ( $\phi$ ), the rotation of the sample and psi ( $\psi$ ), the tilt of the sample, both of which can be controlled to a resolution of 0.01°. These two axes, plus the omega ( $\omega$ ) axis, allow for the intended diffraction plane to be accessed. As shown in figure 2.2, omega is defined as the angle between the incident x-ray beam and the surface of the sample and ideally the out-of-plane orientation of the crystal should be parallel to the surface of the sample. The 2theta ( $2\theta$ ) angle is the angle between the continuation of the incident and diffracted beam. Both of these angles have a controllable resolution of 0.0001°. Moving both omega and 2theta to maintain a constant off-set between omega and theta requires moving the 2theta axis at twice the angular velocity of omega. A rocking curve (RC) is produced when the value of  $\omega$  is kept constant and  $\omega/2\theta$  is scanned across the desired reflection. An RSM is collected by building a series of RC scans each time varying the off-set value between  $\omega$  and  $\theta$ . The area covered by this type of scan can be seen in figure 2.4. Whilst the data is collected as a series of  $\omega/2\theta$  scans to build up an  $\omega$  vs.  $\omega/2\theta$

area scan, it is possible then to convert this scan on to reciprocal space axes. This conversion is accomplished by the software program PANalytical X'Pert EpiTaxy.

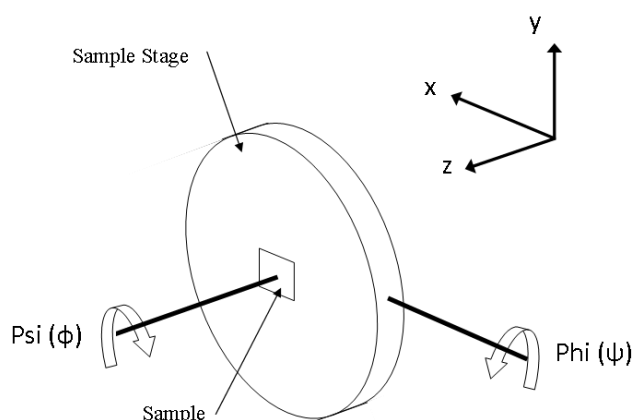


Figure 2.3 A schematic view of the degrees of freedom of the sample stage which allow for the orientation of the crystal to access the possible lattice point.

#### 2.2.5.1 Reciprocal Space Maps

The complete reciprocal space map of a material is made up of a series of points that represent the various planes of the crystal lattice; these points are defined by the surface normal vectors of the crystal planes. Not all of these points are accessible in the experiment; access to these points is restricted by two physical constraints, namely, the x-ray wavelength and the incident angle,  $\omega$ . Scanning in an  $\omega/2\theta$  range, the scan cannot access crystal planes with a d-spacing less than  $\lambda/2$ . In addition, the diffractometer cannot access crystal planes that the incident x-ray beam cannot illuminate, i.e. where  $\omega < 0$  and  $\omega > 2\theta$ . Figure 2.4 shows the area of the RSM where these restrictions apply and also shows how the  $\omega$  and  $\omega/2\theta$  physical scanning directions relate to the RSM directions.

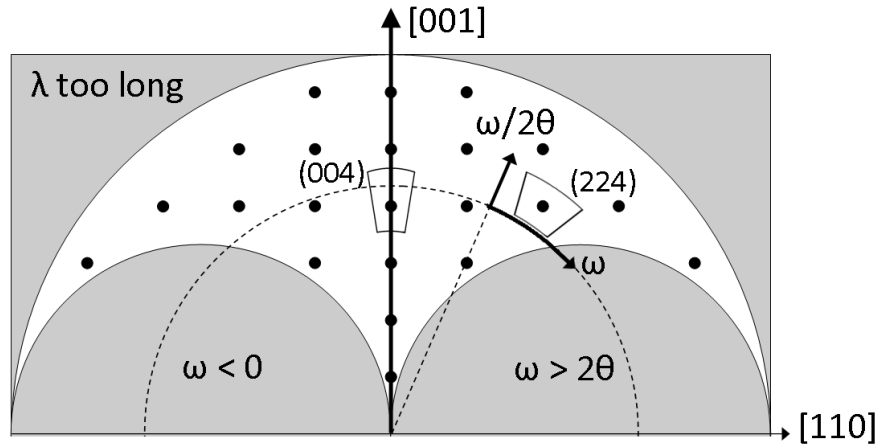


Figure 2.4 A schematic view of the accessible reciprocal space points from a (001) orientated crystal in HR-XRD reflection mode as shown in figure 2.3. Also shown are the scan axes along which the RSM's are collected as well as the positions of the [004] and [224] RSM points.

An out-of-plane and an in-plane RSM needs to be collected to determine the in-plane,  $a_x$ , and the out-of-plane,  $a_z$ , lattice parameters of the layer. Given these lattice parameters, it is possible to calculate the relaxation and composition of the layer. As alluded to earlier, it is possible to calculate either the relaxation or the composition of the layer from only the (004) rocking curve. However, for this to be achieved, the other parameter has to be known beforehand. For example, if  $a_z$ , calculated from the (004) rocking curve, and the composition of the layer are known, it is possible to calculate the value of the in-plane lattice parameter,  $a_x$ , from the change in  $a_z$ , compared to the bulk material, and how this change will deform the material in the x and y directions. This is given by the Poission's ratio of a given material. Knowing both  $a_z$  and now  $a_x$  it is possible to calculate the relaxation of the layer. If both the composition and the relaxation of the layer are unknown, both the out-of-plane (004) and in-plane (224) RSM are needed to determine  $a_z$  and  $a_x$  directly. The in-plane lattice parameters  $a_x$  and  $a_y$  are assumed to be equal as the substrate is cubic and will cause general bi-axial relaxation of the layer. (Section 2.2.5.2)

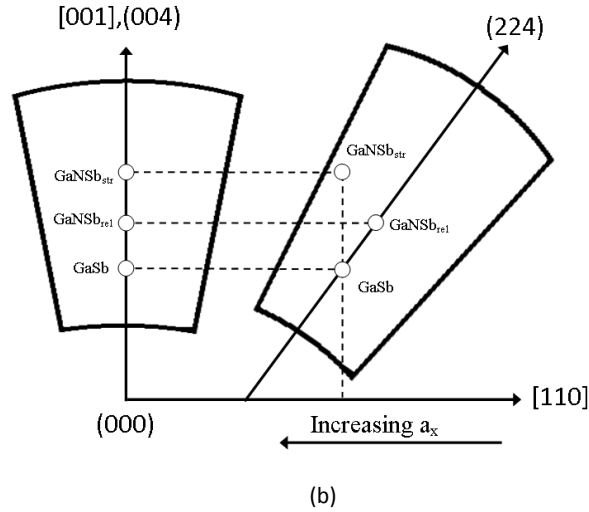
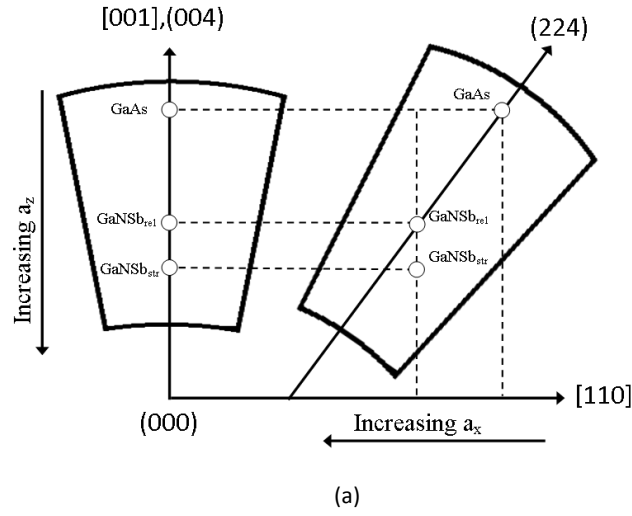


Figure 2.5 A schematic view of the (004) and (224) RSM's showing the positions of the peaks (open circles) of the substrates (a) GaAs and (b) GaSb, and where a generic GaNSb layer peak would be found if it were fully relaxed (rel) or fully strained (str).

Figure 2.5 shows the positions of the peaks (represented by circles) for the (004) and (224) RSM's of a layer of GaNSb, which is grown on either GaSb or GaAs. The relative positions of the peaks from each reflection for the substrate and the layer are shown as well as the effect increasing  $a_x$  and  $a_z$  has on the positions of these peaks. The effect that the relaxation of the layer has on the position of the layer peak in both RSM's is also shown. Note that if the layer is fully relaxed then the (224) layer peak will lie on the [224] lattice vector. If the strained peak lies on the left of the [224] vector, then this indicates that the layer is under bi-axial tensile strain (figure 2.5(b)) and if to the right of the vector, that the sample is

under compressive strain (figure 2.5(a)). This is the case for samples of GaNSb grown on GaSb and GaAs respectively. Under compressive strain the  $a_x$  lattice parameter of the layer is smaller than  $a_z$  and the reverse is true for tensile strain. These two cases are shown diagrammatically in figure 2.6. The (004) RSM shown in figure 2.5 shows that regardless of the composition or the relaxation of the layer, the peak always lies on the [004] vector. The layer peak will appear closer to the GaAs peak as the nitrogen content increases, i.e. a reduction in the  $a_z$  lattice parameter. Similarly the relaxation of the layer will also move the layer peak closer to the GaAs peak. From the analysis of the (004) RSM, the vertical component of the shift in the layer peak in the (224) RSM can be determined and, therefore, the change in  $a_x$ . This is only valid if either the relaxation or the composition of the layer is known. Where both are unknown, the relative positions of the layer peaks are compared to the positions of the substrate peak to allow for the determination of both relaxation and composition. The high number of dislocations between the layer and the substrate caused by the high degree of lattice mismatch can lead to distortions in the layer peak shape. This spreading of the peak in the omega direction is caused physically by the creation of small mono-crystalline blocks within the layer, each with slightly different orientations, which arise from the interface with a dislocation; this effect is referred to as mosaic spread. There are other effects which cause a spread in the peak in the omega direction such as the surface roughness of the layer at the interface. [9] This explains why the substrate peak is sharp and well defined, indicating few defects and high crystalline quality, compared to that of the layer, which typically has distortions from defects and roughness.

#### 2.2.5.2 Relaxation and composition

In order to determine both the composition as well as the relaxation of the layer the in-plane lattice parameter,  $a_x$ , and the out-of-plane lattice parameter,  $a_z$ , have to be determined;- this is achieved using the method described above. (Section 2.2.5.1). The composition of the layer is determined by Vegard's law. [10] In this work, both the linear approximation of Vegard's law (equation 2.6) and a more precise version are used. The latter version can be applied to semi-conductor materials by examining the bandgap energies of the various end member materials as well as composite materials and leads to the determination of the so-called 'bowing parameter'. In the case of GaNSb, this bowing parameter is 0.028, [11] and the full representation for this version of Vegard's law is given in equation 2.7.

$$a_{GaNSb} = xa_{GaN} + (1-x)a_{GaSb} \quad (2.6)$$

$$a_{GaNSb} = xa_{GaN} + (1-x)a_{GaSb} - 0.028x(1-x) \quad (2.7)$$

Using known values of the lattice parameters of both GaSb,  $a_{GaSb}$ , and cubic-GaN  $a_{GaN}$ , as well as the calculated, relaxed, lattice parameter of the layer  $a_{GaNSb}$ , it is possible to determine the proportion of nitrogen within the sample,  $x$ . In order to determine the relaxed lattice parameter for the layer the amount of strain within the layer has also to be calculated. This is achieved by the analysis given below.

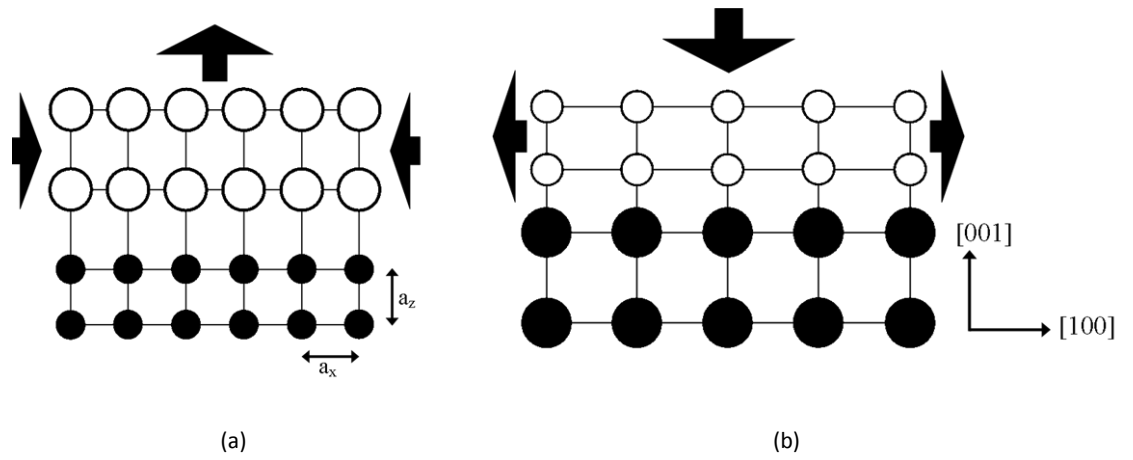


Figure 2.6 the tetragonal distortion of the layer (open circles) on the substrate (filled circles) for the case (a) where the layer is under compressive strain- for example GaNSb grown on GaAs, and (b) under tensile strain- GaNSb grown on GaSb. The arrows indicate how the bulk lattice parameters of the layer change under each of the strain conditions.

Any crystalline material that is grown on a substrate with a different lattice parameter will be strained. This difference in lattice parameters will force each mono-layer of the deposited material to arrange itself best to match the in-plane lattice parameters of the substrate material. (Figure 2.6) The mismatch between the layer and the substrate can be described by the ratio ( $f$ ) calculated from the unstrained lattice parameters of the layer,  $a_{bulk}$ , and the substrate,  $a_{substrate}$  as defined in equation 2.8. The greater this ratio the greater the expected amount of strain within the layer. The sign of this ratio will indicate whether the layer undergoes compressive or tensile strain, a negative value indicates tensile strain.

$$f = \frac{a_{substrate} - a_{bulk}}{a_{substrate}} \quad (2.8)$$

In a layer of GaNSb, if the nitrogen atoms are assumed to be randomly distributed with the structure, the induced strain will have no preference for either the [100] or the [010] direction within the plane of the crystal. Therefore, the strain that is induced will be the same in both directions and assumed to be a bi-axial strain distribution. As a result of this, both in-plane lattice parameters  $a_x$  and  $a_y$  can be considered to be the same. To compensate for this strain of the layer material in the xy plane, the GaNSb layer will deform out of the plane of the sample. The out-of-plane lattice parameter will be tetragonally distorted when compared to the in-plane parameters; the direction of this distortion is shown in figure 2.6. The relationship between the lattice parameters is dependent on the elastic moduli,  $C_{11}$  and  $C_{12}$ , of the layer material, as defined in equation 2.9.

$$a_z = a_{bulk} + \frac{2C_{11}}{C_{12}}(a_{bulk} - a_x) \quad (2.9)$$

Where  $a_z$  and  $a_x$  are as defined above and  $a_{bulk}$  is the cubic lattice parameter of the unstrained material. Assuming bi-axial strain, as described above, the value of  $a_x$  can be the strained value in either the <100> or the <010> direction. This expression can be then be described using the definition of Poisson's ratio ( $\nu$ ) given in equation 2.10 which describes the strain expected in one direction given an applied strain in the perpendicular direction.

$$\nu = \frac{C_{12}}{C_{11} + C_{12}} \quad (2.10)$$

The Poisson's ratio of a layer varies in accordance with Vegard's law in a similar way to the lattice parameter of the layer. Combining equations 2.9 and 2.10 gives the out-of-plane lattice parameter as a function of Poisson's ratio; this is the constant that is used in the fitting of the RSM data.

$$a_z = a_{bulk} + \frac{2\nu}{1-\nu}(a_{bulk} - a_x) \quad (2.11)$$

The strain within the layer ( $\epsilon$ ), with respect to the substrate strain, which is expected to be zero, is defined in equation 2.12. As the thickness of the layer increases the amount of strain energy stored in the layer increases also. All parameters have the same definitions as given above and R is the relaxation of the layer.

$$\epsilon = f(1-R) = \frac{a_x - a_{bulk}}{a_{substrate}} \quad (2.12)$$

From examining equation 2.12, if  $a_x > a_{bulk}$  then strain has a positive value and the layer is under tensile strain, with the opposite being true if the layer is under compressive strain. Following on from this, the relaxation of the layer can be therefore defined as:

$$R = \frac{a_{substrate} - a_x}{a_{substrate} - a_{bulk}} \quad (2.13)$$

When the relaxation value is greater than 100%, the layer is said to be over-relaxed and, as shown in graphically in figure 2.6, if  $a_{bulk} > a_{substrate}$  then the layer is under compressive strain, similarly, if  $a_{bulk} < a_{substrate}$  the layer is under tensile strain.

## 2.2.6 Single-Crystal diffraction

### 2.2.6.1 Data Collection

The single-crystal experiments conducted in this work were performed on an Oxford Diffraction diffractometer, which utilises a large 2-dimensional charged-coupled device (CCD) detector. Again a copper x-ray source was used producing  $CuK\alpha$  radiation which is then monochromated using a graphite crystal before being collimated to produce a parallel x-ray beam with a small spot size. Single-crystal diffraction involves collecting a significant portion of the Ewald sphere of a crystal. Unlike a polycrystalline material, where there is a random orientation of crystallites allowing only a simple theta/2theta scan to access all crystallographic planes, a single-crystal has to be oriented relative to the detector so that individual planes can be accessed in three dimensions. This is achieved using a four-circle, kappa-geometry goniometer that moves the crystal, which is mounted on a glass fibre and aligned to the centre of the incident x-ray beam, through space. A data collection run involves moving the crystal to a particular orientation and using the detector to collect a frame containing all the available Bragg reflections given that orientation of the crystal. The next frame is the collected by moving one or more of the goniometer axes and illuminating the crystal, for a prescribed exposure time. This is then repeated at other orientations until the desired proportion of the Ewald sphere is collected. The proportion of the Ewald sphere that is collected is known as the completeness of the experiment this value is also referenced to the desired resolution, i.e. the minimum d-spacing, of the experiment. For example, collecting a hemisphere of the Ewald sphere corresponds to a completeness of 50%. The other value that is important when designing the optimum experiment is the redundancy of the reflections collected. This is the average number of times each reflection is collected in different frames. The higher this redundancy the more precise the data



collection has the potential to be and the more reliable the collected intensities and the subsequent structural solution. The individual frames from the data collection are then integrated to produce an inventory of reflections collected and the corresponding intensity of the reflection, averaged over the redundancy of the experiment. The variations in the intensity of the individual frames contribute to a measure of the quality of the integration and therefore the quality of the crystal. This internal R-factor is defined as:

$$R_{\text{int}} = \frac{\sum_n |F_{n(o)}^2 - \langle F_{n(o)}^2 \rangle|}{\sum_n F_{n(o)}^2} \quad (2.14)$$

Where  $F_{n(o)}^2$  is the intensities of the individual peaks, for a given reflection, and  $\langle F_{n(o)}^2 \rangle$  is the averaged intensity. Clearly for ideal data from an ideal crystal this  $R_{\text{int}}$  value would be equal to zero as for every individual peak for a given reflection  $F_{n(o)}^2 = \langle F_{n(o)}^2 \rangle$ .

#### 2.2.6.2 Structural Refinement

It is entirely possible to find the structural solution for a single crystal given a data collection of adequate quality, namely, one with appropriate d-spacing resolution, completeness and redundancy as well as an appropriately small internal R-value. However, the work in this thesis has not required the use of any of these *ab initio* structural solution techniques as the crystal structure of the materials studied here were already known or could be inferred from the structures of similar materials. The structural refinement of single-crystal data is very similar to that of powder diffraction using Rietveld refinement in that it is a least-squares refinement process that compares a model with the data. In single-crystal refinement, instead of a calculated intensity for each increment of the pattern, a full matrix of structural factors is refined i.e. the intensity of each individual Bragg reflection in reciprocal space. Again a residual,  $R_s$ , is defined which is then minimised. (Equation 2.15) Where  $F_{n(c)}$  is defined as the calculated structure factor of a reflection with indices n.

$$R_s = \sum_n [F_{n(o)} - F_{n(c)}]^2 \quad (2.15)$$

There are several other R-values that help define the quality of any structural refinement:- these include  $R_{\text{obs}}$  which corresponds to only the observed data- that is a peak which has an intensity of over three times the standard deviation,  $I > 3\sigma$ . The definitions of these R-

values are given in table 2.4. The goodness-of-fit parameter is of a similar form to that defined for the Rietveld method; however in this case,  $i$  represents the number of reflections and not the number of increments, with  $m$  again representing the number of matrix elements.

Fit Parameter	Definition
R-Factor	$R_{obs} = \frac{\sum_n \ F_{n(o)} - F_{n(c)}\ }{\sum_n F_{n(o)}}$
(Observed) R-Factor	$R_{obs} = \frac{\sum_{n(I>3\sigma)} \ F_{n(o)} - F_{n(c)}\ }{\sum_{n(I>3\sigma)} F_{n(o)}}$
Goodness-of-fit	$GOF = S = \sqrt{\frac{\sum_n w_n (F_{n(o)}^2 - F_{n(c)}^2)^2}{i - m}}$

Table 2.4 Various quality of fit (R) factors which apply to the least squares refinement of single crystal diffraction data.

## 2.3 Complementary Techniques to Diffraction

In addition to x-ray diffraction, which form the bulk of the analysis used during this work, additional experimental techniques were used and a brief description of each of these techniques is given below.

### 2.3.1 Secondary Ion Mass Spectroscopy (SIMS)

SIMS is a technique that allows the composition of a material to be profiled as a function of depth. By knowing the rate at which the primary ion beam is eroding the sample it is possible to confirm the depth of a given layer within a sample.

In this study, relatively low energy SIMS was performed by an Atomika 4500 SIMS profilometer with a primary, oxygen ( $O_2^+$ ), beam of energy 4keV. This energy gives a depth resolution in the nanometre range. The SIMS data presented in this work were collected by Dr. Richard Morris, a member of the Analytical Science Projects group in Physics at the University of Warwick.

SIMS involves irradiating the sample with the primary ion beam. The energy of this beam has to be sufficient to ionize the atoms at the surface of the sample. The primary beam is usually at normal incidence to the surface of the sample but this angle between the beam and the surface can be changed to reduce the erosion rate. [12] The area of the sample that is exposed to the beam is 250 $\mu\text{m}$  by 250 $\mu\text{m}$ . The ions of atoms within the sample are not detected directly; it is the secondary ions which are sputtered off the surface of the sample that are analysed. The secondary ions, in this case various oxide ions, are detected by a quadrupole mass spectrometry (QMS). The QMS is selective and only detects ions with a specified charge mass ratio; this allows for the characterisation of different chemical species emanating from the sample. By analysing the rate at which these different ionic species are detected (the current density) the concentrations of various atoms within the layer can be calculated.

Whilst not used in this work, as only a comparison was required and not absolute values, the erosion rate of the sample can be determined by using a line profiler to find the depth of the crater that is formed as a result of the sputtering of the secondary ions. Using the erosion rate, the current density and the ion concentration it is then possible to profile a sample's chemical composition as a function of depth of the layers in the sample.

The resolution of this technique can be limited by several factors such as surface roughness and unanticipated reactions between the incident beam and the atoms in the surface. The surface roughness can cause deflections in the secondary ion beam resulting in these ions not reaching the QMS thus altering the results. There is also the possibility of the incident ion beam pushing the surface atoms deeper into the sample resulting in these atoms not been seen until later in the SIMS scan. This effect has the potential to make it appear that atoms have naturally diffused deeper into the sample than is really the case and possibly even into what appears to be another layer within the sample. The effect of this can be mitigated by reducing the energy of the incident beam and changing the incident angle of the beam to one of a grazing incidence geometry.

### 2.3.2 Nuclear Magnetic Resonance (NMR)

NMR can be a complementary technique to XRD and can be used to confirm local details of a structure that cannot be conclusively verified by XRD. In this work, the main use of NMR is to confirm the inclusion of various atoms within the crystal structure of materials. Many of the materials examined in this work are constructed of very light elements and therefore

have few electrons, i.e. low x-ray scattering factors; therefore, it is frequently difficult to confirm the substitution of these light elements in materials using XRD alone. NMR is used to investigate the structure of a material by examining the short-range order i.e. order on the length-scale of the chemical bond in the material and whether this short-range order is consistent with the corresponding short range interactions expected from the assumed crystal structure of the sample.

NMR relies on the intrinsic, quantum mechanical, property of spin, which is a property of the nucleus of atoms. This spin is related to the magnetic moment,  $\mu$ , of each of these atoms given by equation 2.16 and is only evident in atoms with a non-zero net spin.

$$\mu = \gamma I \quad (2.16)$$

Where the value  $\gamma$  is the gyromagnetic ratio and is a constant for each isotope of each type of atom nucleus. When no external magnetic field is applied then the magnetic moments within a sample are randomly oriented. When an external magnetic field (**B**) is applied, the magnetic moments will prefer to align with the field and produce a net magnetisation within the sample. By convention in the laboratory reference frame this magnetic field is said to be in the z-direction such that the field can be defined as **B** = (0,0, $B_0$ ) where  $B_0$  is the magnitude of the magnetic field. Whilst the magnetic moments would prefer to be perfectly aligned with the magnetic field, in reality they precess [13] around the field,  $B_0$ , at a frequency, which is defined as the Larmor frequency,  $\omega_0$ , such that

$$\omega_0 = -\gamma B_0 \quad (2.17)$$

Due to the random orientation of these moments they appear to form a cone around the magnetic field axis and this leads to a net magnetisation aligned with the magnetic field (**B**).

The angular momentum associated with the nuclear spin of the nucleus is quantised and, therefore, the values of magnetic moment are also quantized, given the relationship in equation 2.16. The levels at which the magnetic moment can be quantised are restricted and can only vary in integer steps from  $-I$  to  $I$ . This results in a new parameter,  $m$ , the magnetic quantum number, which can have any of these values. Therefore the number of unique values  $m$  can take is  $2I + 1$  each of which corresponds to different energy levels in the magnetic field  $B_0$ , which are given by

$$E = -\gamma \hbar B_0 m \quad (2.18)$$

As a result there is a splitting of the energy of the different nuclear spin states when placed in a magnetic field, this is the Zeeman effect, and the states are referred to as Zeeman states. There are  $2I + 1$  states for each nucleus and the difference in energy between these states is  $\Delta E = \gamma \hbar B_0$  this relationship allows higher-strength magnetic fields to increase the splitting in these energy levels. This energy difference corresponds to photons in the radio frequency (r.f.) range.

These Zeeman states are affected by the local environment in which the nucleus resides resulting in the splitting of these states further into additional discrete energy levels. These local effects can be categorised as chemical shift, dipolar interaction, j-coupling and quadrupolar interactions. [14]

In order to collect this information, an r.f pulse at the Larmor frequency of the nucleus in question, is applied to the sample. The nuclei interact with this energy and the spins rotate around to the y-axis resulting in a change in the direction of the net magnetic moment within the material. As the nuclei now precess around a different axis, it is possible to detect the weak r.f. signal from these magnetic moments. The characteristics of this signal give details of the local environment of the nuclei. This signal will soon decay as a result of two factors; transverse and longitudinal relaxation. After the r.f. signal is applied, the coherent precession of the nuclei will start to de-phase due to the thermal motion of the individual nuclei. The rate of this decay is proportional to  $\exp\left(-t/T_2\right)$  where  $T_2$  is known as the transverse relaxation time. In addition to this, the net magnetic moment decays back to its ground state, aligned along the z-axis, with the rate at which this longitudinal decay occurs proportional to  $\exp\left(-t/T_1\right)$ , where  $T_1$  is the longitudinal relaxation time.

The weak r.f. signal that is detected is a free induction decay (FID) signal in time space and contains all the frequencies present in the sample. These frequencies are extracted by performing a Fourier transform of the FID to produce an NMR spectrum. As mentioned above, there are several interactions that affect the local magnetic environment of the nuclei: chemical shift, dipolar interaction, j-coupling and quadrupolar interactions, all of which will be encoded in the NMR spectrum.

Chemical shift is dependent on the local magnetic environment produced by the electronic configuration of neighbouring atoms; this means that nuclei on crystallographically equivalent sites within the sample should experience the same chemical shift. Quadrupolar

interactions occur as a result of the nuclei's electric quadrupole moment interacting with the electric field gradient produced by the surrounding electrons. This is only observed in quadrupolar nuclei ( $I > \frac{1}{2}$ ) and only when these nuclei are in asymmetric environments.

Dipole and J-coupling interactions are a result of through-space and indirect coupling, through bonding electrons, of dipole moments of neighbouring atoms, respectively. More information on these effects can be found here. [13-15]

The most useful parameter for observing the local environments of the target nuclei is chemical shift. Since the absolute chemical shift will be dependent on the magnetic field strength of the specific NMR apparatus used, these shifts are referenced to the chemical shift of a standardised material. This material usually has a high concentration of the target nucleus and is either in solution or on a highly symmetric crystallographic site. The result of using a standard material for a nucleus is well-resolved sharp peak in the NMR spectrum of the reference material. Chemical shift,  $\delta$ , is then defined relative to the observed frequency of both the reference and the sample.

$$\delta = \frac{\nu_{sample} - \nu_{reference}}{\nu_{reference}} \quad (2.19)$$

In most cases the interactions that affect the NMR spectrum, such as electric shielding and dipole interactions, are dependent on crystallographic orientation, which causes broadening of the peaks observed in the NMR spectra. As the angular dependence of these interactions is of the form  $3\cos^2\theta - 1$ , they can be removed by spinning the sample at an angle which satisfies the condition  $3\cos^2\theta - 1 = 0$ . This technique is known as magic-angle spinning (MAS), which involves spinning the rotor (containing the sample) around an axis orientated at the 'magic angle' ( $54.74^\circ$ ) to the applied field.

As a result of the signal decay and the weakness of the signal, the r.f. pulse is repeatedly reapplied and the results are aggregated until a signal with adequate signal-to-noise ratio is collected. The length of the applied r.f. pulse is important as this determines the angle that the net magnetic moment is rotated by relative to the z-axis. There is a linear relationship between the pulse length and this tip angle and a larger tip angle gives a stronger r.f. signal but it will take longer for this signal to decay longitudinally. This leads to the second important parameter during NMR experiments, the pulse delay; this is the time between repeated pulses. In this delay the spins of the nuclei are allowed to decay to the ground

state whilst the signal is collected. The delay has to be sufficient to allow the detection of all environments some of which may have longer longitudinal decay times and will, therefore, not be observed in the NMR spectrum if a shorter pulse delay time is used. Both the pulse length and the pulse delay times effect the overall length of any NMR experiment.

### 2.3.3 Thermal Analysis (TA)

Thermal analysis techniques allow properties of a sample to be investigated as they change with temperature. These techniques help identify any type of chemical reaction or structural phase change, as they either require input of energy, in the form of heat (endothermic) or release energy (exothermic). The main TA technique used during this work is Differential Scanning Calorimetry (DSC) which is concerned with the amount of heat that is required to increase the temperature of the sample. This is subtly different to another TA technique, Differential Thermal Analysis (DTA) which measures the temperature of the sample when exposed to a constant heat flow. Both these techniques traditionally measure the response of the sample relative to a reference material which should ideally have a well defined heat capacity over the range of temperatures that are to be investigated; additionally the reference sample should not undergo any structural phase change over the temperature range in question. In the case of DTA the difference in temperature between the sample and the reference is recorded and in DSC the difference in the amount of heat required between the sample and the reference is investigated. However in the experiments conducted in this work no reference sample was used, instead an initial data collection over the same thermal cycle as that of the sample was collected to identify any anomalous heat signatures from the equipment. These data were then used to correct the data collected subsequently to ensure that the response seen is from the samples only. A DSC experiment results in a curve of heat flux plotted against either temperature or time. On a cautionary note, there are differing conventions on what sign the heat flow should take when discussing the type of event, either exothermic or endothermic.

## 2.4 Air and Moisture Sensitive Samples

Many of the materials studies in this work are both air and moisture sensitive. As a result of this, these samples have been stored and manipulated, as well as loaded for experiments, in a Belle Technology anaerobic dry glove box using methods devised for the purposes of the work in this thesis. This nitrogen-filled glove box maintains an inert

atmosphere at a pressure of 2bar (30psi) above atmospheric pressure to minimise the ingress of air, and maintains consistent oxygen and water content of <10ppm by volume. The glove box is supplied from an in-house nitrogen source produced from the boil-off from cryogenic nitrogen storage tanks. This nitrogen is supplied at a pressure of 2bar and can be supplied to the glove box at a rate of 30 litres per minute. The nitrogen supply is controlled by a pressure sensitive valve and helps maintain the pressure within the glove box. In addition, the atmosphere in the glove box is re-circulated at a rate of three quarters of a cubic metre per minute through both oxygen and moisture removal cartridges. There are two oxygen removal cartridges (R3-11G) which consist mainly of copper oxide (CuO) and magnesium-silicon (Mg-Si). These materials react with any residual oxygen in the gas flow from the glove box and have to be periodically regenerated to maintain their functionality. The other two cartridges contain moisture sieves (4Å zeolite), which are designed to trap H<sub>2</sub>O molecules present in the gas stream. Similarly to the oxygen removal cartridges, these have periodically to be regenerated to remove any H<sub>2</sub>O from the zeolite. Whilst one of these cartridges is being regenerated, the other three are capable of maintaining the atmosphere in the glove box. Before the re-circulated gas is returned to the glove box, it passes through a series of particulate filters to remove any dust or powder from the atmosphere. The glove box contains a small temperature controlled furnace built in the physics department as part of this work and unless otherwise stated, all air-sensitive samples were synthesised in this furnace under the inert nitrogen atmosphere. Samples were prepared for x-ray analysis by filling a glass capillary and were then sealed either with hot wax or a mechanical capillary sealing device, which uses a series of rubber o-rings under compression to seal the funnel end of the glass capillary. This device can be removed and reused without damage to the capillary. Similarly, for other experimental techniques, the samples for investigation were also loaded into an appropriate vessel in the inert atmosphere of the glove box. Samples for thermal analysis were loaded into small aluminium pans with aluminium lids which were pressure sealed to the pan. Samples for NMR were loaded into 4mm diameter rotors and the lids for the rotors were pressed into position before the rotors were removed from the atmosphere of the glove box. Samples and apparatus were added and removed from the glove box through a transfer chamber which is purged with nitrogen from the same supply as described above, before the inner airlock door was opened.



## References

- [1] T. Hahn (ed.), International Tables for Crystallography, Volume A, space-group symmetry. New York: kluwer Academic Publishers (1995)
- [2] M. T. Dove, Structure and dynamics: an atomic view of materials. Oxford University Press (2003)
- [3] C. Giacovazzo (ed.), Fundamentals of Crystallography. Oxford University Press (1992)
- [4] H. M. Rietveld, Acta Cryst **22** (1967) 151-152
- [5] H. M. Rietveld, J. Appl. Cryst. **2** (1969) 65-71
- [6] R. A. Young (ed.), The Rietveld Method. Oxford University Press (1993)
- [7] A. A. Coelho, J. Appl. Cryst. **38** (2005) 455
- [8] Topas Academic Technical Reference v4.1 (2006)
- [9] D. Bowen and B. K. Tanner, High Resolution X-ray Diffraction and Topography. 1<sup>st</sup> ed. London: CRC (1998)
- [10] A. R. Denton, N. W. Ashcroft, Phys. Rev. A, **43** (1991) 3161-3164
- [11] PANalytical X'pert Epitaxy Software
- [12] P. C. Zalm, C. J. Vriezema, D. J. Gravesteijn, G. F. A. van de Walle, W. B. de Boer, Surface and Interface Analysis, **17** (1991) 556-566
- [13] M. J. Duer, Solid-State NMR Spectroscopy. Blackwell SciencePublishing (2004)
- [14] M. Levitt, Spin-Dynamics. John Wiley & Sons (2000)
- [15] K. Mackenzie, M. Smith, Multinuclear Solid-State NMR of Inorganic Materials. Pergamon (2002)

## Chapter 3

# Di-sodium Amide Borohydride

### 3.1 Introduction

One of the various complex metal hydrides that have been considered for use as an on-board hydrogen storage material is di-sodium amide borohydride,  $\text{Na}_2\text{NH}_2\text{BH}_4$ . This material has a relatively high theoretical hydrogen weight percent of 7.87 Wt% and has the potential for use as a viable hydrogen storage material as it falls within the long range targets set by the DOE, US Department of Energy, which are seen as the benchmark in this research area. (Table 1.2) This material was first synthesised at Birmingham University by Chater *et al.* in 2006 [1]. They showed that  $\text{Na}_2\text{BH}_4\text{NH}_2$  had a primitive cubic structure and showed that hydrogen could be desorbed from the material at temperatures around 290°C but gave no evidence of the material's crystal structure. Since then an additional study [2] in 2010, expanded on the previous work and not only deduced the crystal structure of the cubic phase (hereafter C-phase) but also determined the crystal structure of a hitherto unreported orthorhombic phase (hereafter O-phase), which they showed was a low-temperature polymorph of  $\text{Na}_2\text{NH}_2\text{BH}_4$ . That study also showed how the symmetry of the low-temperature structure is modified to derive the high-temperature structure and that there is a temperature-driven phase transition between the low-temperature, O-phase, and the high-temperature, C-phase. Both studies show, through vibrational spectroscopy, that the  $[\text{BH}_4]^-$  and  $[\text{NH}_2]^-$  remain intact, if somewhat distorted, this provides the justification for calling the material  $\text{Na}_2\text{NH}_2\text{BH}_4$  as opposed to the more conventional naming of  $\text{Na}_2\text{NBH}_6$ . Although the 2010 study shows x-ray diffraction (XRD) data for each polymorph, which are used as the starting point for the structural determination in this work, very little detail regarding these structures as a function of temperature was given in either of these studies. In this chapter, the nature of this phase change is described in detail thus explaining the crystallographic behaviour of the material across the phase transition. This is important to understand as any device which utilizes this material might reasonably be expected to perform in variable-temperature environments.

The C-phase of  $\text{Na}_2\text{NH}_2\text{BH}_4$  has a perovskite structure,  $Pm\bar{3}m$ , with the sodium atoms forming an octahedron around the amide ion  $[\text{NH}_2]^-$  with the borohydride ions,  $[\text{BH}_4]^-$ , at

the vertices of the unit cell. As the sodium ions having a valence of +1, the octahedral sites have to be only 2/3 filled to achieve charge balance (figure 3.3(a)). [2] The O-phase belongs to space group  $Pbcm$  (figure 3.3(b)) and is a modification of the perovskite structure with distortions to the cubic symmetry of the C-phase. The borohydride ions which are located at the corners of the cubic unit cell have been rotated into a kite shape when viewed along the 001 direction with two sets of adjacent, equal-length, sides with the shorter sides making an angle greater than the longer sides. In addition to this, the sodium octahedra around the amide ion have tilted along the c axis one clockwise and the other anticlockwise relative to the C-phase structure thus effectively doubling the unit cell in this direction. As well as rotating relative to the next octahedron in the 001 direction, the bonds between the sodium ions in the  $ab$  or (001) plane of the O-phase are no longer at right angles as they would be in the C-phase structure, this angle has decreased as the ions are moved from the special positions occupied in the C-phase. From the comparison between figures 3.1(a) and 3.1(b) the origin of 2/3 filled octahedra of the C-phase can be seen in the O-phase with there only being two sodium ions around each amide ion in the (001) plane.

## 3.2 Experimental Details

### 3.2.1 Synthesis

$\text{Na}_2\text{BH}_4\text{NH}_2$  was synthesised from a mixture of  $\text{NaBH}_4$  (Sigma-Aldrich, >98%, white powder) and  $\text{NaNH}_2$  (Sigma-Aldrich, >95%, white powder) in a 10:9 molar ratio. This ratio was chosen for two reasons: (a) to avoid any un-reacted sodium amide being present in the final sample; (b) to retain an internal reference material in the form of excess sodium borohydride, which is a well-characterized cubic structure ( $Fm\bar{3}m$ ,  $a = 6.131(1)\text{\AA}$ ) over the majority of the temperature range to be investigated.[3] As the starting materials and the resulting products are highly air- and moisture- sensitive, the materials were all handled and stored under an inert atmosphere (nitrogen filled glove box; <10ppm  $\text{O}_2$ , <10ppm  $\text{H}_2\text{O}$ ). The powder was finely ground and mixed in the appropriate ratio and sealed in a glass capillary, 0.7mm dia., then heated to 190°C and cooled. All subsequent powder analysis was undertaken on this sealed capillary sample.

Single crystals of  $\text{Na}_2\text{BH}_4\text{NH}_2$  were formed from powder produced using this same route by reheating the powder sample to above its melting point, 220°C, and cooling through the liquid to solid phase change at a rate of 10°C/hr whilst in the inert atmosphere of the glove box. In order to examine the results of this process, the resulting products were trapped under oil, removed from the protective atmosphere of the glove box and examined under a

microscope to identify any single crystals that were potentially suitable for structural studies. These were then flash-frozen under a stream of nitrogen gas at 100K, which was provided by an Oxford Cryosystems “Cobra”, to solidify the oil around the crystal. The supply of 100K nitrogen was maintained throughout the measurement both to protect the crystal from oxygen in the atmosphere and to maintain the oil in a solid state around the crystal thereby offering additional protection from ambient atmospheric conditions.

### 3.2.2 Thermal Analysis and Structural Experiments

Differential Scanning Calorimetry (DSC) was used in the temperature range of -150°C to 240°C, just above the melting point of  $\text{Na}_2\text{BH}_4\text{NH}_2$ . 12mg of the starting materials,  $\text{NaBH}_4$  and  $\text{NaNH}_2$  in the appropriate ratio, were sealed in a 40 $\mu\text{L}$  aluminium crucible in a glove box and remained sealed during the DSC measurements. The sample was heated from room temperature up to 240°C then down to -150°C then back up to 240°C and finally down to room temperature. The sample was investigated down to such a low temperature to be sure that no other previously unreported phase transition could be detected.

Room-temperature and high-temperature XRD powder patterns were obtained using a high-temperature capillary stage affixed to a PANalytical MPD high resolution powder diffractometer, and employing  $\text{CuK}\alpha_1$  radiation. Hereafter this experimental setup is known as HT-PXRD. Low-temperature powder diffraction (LT-PXRD) was completed using a custom-built capillary holder on an Oxford Diffraction (Agilent Technologies) Gemini single-crystal diffractometer employing  $\text{CuK}\alpha$  radiation, for consistency with the powder diffraction data collection, with a CCD detector producing a 2-dimensional image of the powder diffraction rings around the centre of the x-ray beam, as shown in figure 3.1. As the diffraction rings, from an ideal powder sample are homogenous around the entire circumference, it is not necessary to collect the data around all 360° of the ring. Additionally, the detector is not large enough to collect the entire powder ring, especially at smaller d-spacings, (higher angle). The physical constraints in the movement of the goniometer also have to be considered, curtailing the relative motion of the detector which can be achieved only in the horizontal direction, meaning that no data can be collected from above or below the capillary. Furthermore to avoid the beam stop support arm from blocking the detector, diffraction data are only collected from one side of the capillary. The slight elliptical shape of the powder rings is because the detector is flat and therefore at higher angle the detector is slightly further away from the sample resulting in the increase in the FWHM of each extracted peak in the 1-dimensional powder pattern, figure 3.4b.

CrysAlisPro [4] data processing software was used to extract the powder pattern from the 2-dimensional data by integrating around the circumference of concentric circles from around the centre of the beam and then normalising for the length of the circumference available. The Rietveld refinements of both the HT-PXRD and LT-PXRD data were performed using Topas Academic 4.1[5]

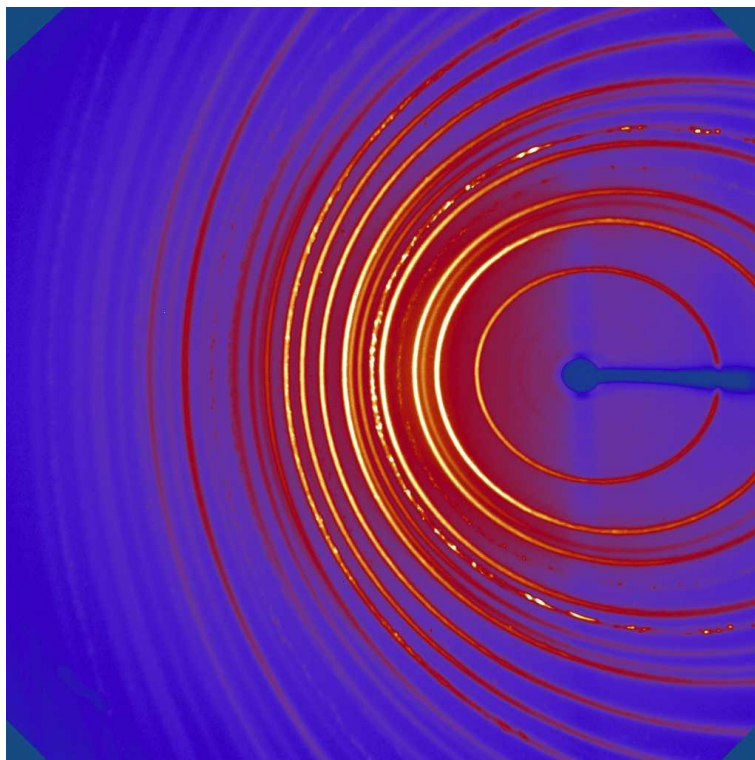


Figure 3.1 X-ray powder diffraction rings collected using a 2-dimensional detector. At high d-spacing almost all of the diffraction ring can be seen however at higher angle only a small arc of the ring can be seen.

The analysis of the single-crystal (CC-XRD) data was achieved using CrysAlisPro. The initial procedure for collecting the single-crystal data involved performing a low angle  $2\theta$  scan as the crystal was rotated around the phi axis of the goniometer. Examining the distribution of the Bragg peaks, as well as the relative intensities, in  $2\theta$  around the inversion centre of the beam determines if the crystal has any inversion symmetry. Using these data, and the assumption that the crystal structure will be one of the structures described above, it was determined that the crystal structure was centrosymmetric. As a result a collection of only one hemisphere of reciprocal space would yield all the data required to determine the crystal symmetry and the structure of the material. Additional symmetry elements allow further reductions in the amount of reciprocal space that needs to be examined for a satisfactory structural refinement. Conducting a short pre-experiment over the entire hemisphere allows for a determination of some of these elements and ultimately the

extent specific unique area of reciprocal space which must be examined. The peak finding and lattice fitting algorithms within the software were able to calculate the most likely lattice type, space group and lattice parameters from the CC-XRD data collected. However there are other factors to take into account it is important to include some redundancy in the measurements that are taken to identify and confirm that for a given equivalent reflection that the intensities and position of these reflections are consistent to verify the determination of the symmetry present in the crystal. These factors have to be balanced against the total time that the sample spends out of the protective atmosphere of the glove box. Whilst the sample is well protected by the flash-freezing it will not last indefinitely. After completing the data collection the same peak searching algorithms and lattice fitting program is employed to firstly confirm the determination of the lattice type and lattice parameters. Then all of the identified peaks are re-indexed using this lattice. The program, by examining the position of systematically absent reflections, determines the most likely space group that the lattice belongs to. Using these data the program indexes each reflection to a specific set of Miller indices, hkl. It is this information, along with the intensity of each reflection, which is exported from CrysAlisPro and used in any future structural refinement.

### 3.3 Experimental Results

#### 3.3.1 Powder Sample

##### (a) Thermal Analysis

From Figure 3.2, we see that during the first heating the reaction of  $\text{NaBH}_4$  and  $\text{NaNH}_2$  to form  $\text{Na}_2\text{BH}_4\text{NH}_2$  appears to be a two-stage reaction between  $130^\circ\text{C}$  and  $150^\circ\text{C}$ . This is not seen in the HT-PXRD data during heating of the same starting materials, which shows that the reaction is complete by  $150^\circ\text{C}$ . The second heating of the sample shows that the reaction isn't fully complete after the first heating as further reaction takes place at the same temperature as before,  $150^\circ\text{C}$ , this time in a single stage. The apparent two-stage reaction observed in the first heating could be a result of abnormal heat flow owing to the ferocity of the reaction, giving rise to an inhomogeneous temperature distribution.  $\text{Na}_2\text{BH}_4\text{NH}_2$  melts and re-crystallizes consistently during both temperature runs: the peaks associated with these events are larger during the second heating and cooling phase which is consistent with the reaction being incomplete during the first heating. There is no evidence from the thermal analysis, of any residual  $\text{NaNH}_2$  after the first heating – however, there must be some present for the continued formation of  $\text{Na}_2\text{BH}_4\text{NH}_2$  during

the second heating. As the melting point of sodium amide is similar to that of  $\text{Na}_2\text{BH}_4\text{NH}_2$  any evidence of sodium amide may be obscured by the low-temperature slope of the response from  $\text{Na}_2\text{BH}_4\text{NH}_2$ . The peaks at low temperature ( $-82^\circ\text{C}$ ) are observed in both pure  $\text{NaBH}_4$  and the mixed sample, proving that these peaks are from the structural phase change in pure sodium borohydride; this is as expected as the mixture is deliberately over doped with  $\text{NaBH}_4$  as to leave no un-reacted sodium amide in the sample after heating. Most interestingly, there is no evidence for the first-order structural phase transition in the DSC data as recently reported by M.Somer *et al.* [2] using similar thermal analysis techniques. This is due to the process that is used in producing the O-phase of the sample, M.Somer *et al.* had to anneal the C-phase at  $70^\circ\text{C}$  for 10 days, the sample in this thermal analysis has only just formed, as C-phase, and so no transition to the O-phase is possible. To achieve the transition from C-phase to O-phase successive heat treatment is required. The process that was used was successive heating, melting and cooling of the C-phase until the O-phase was seen to be present, typically 3 or 4 times. The result is that the C-phase can be seen at low temperatures in the early thermal history of the sample.

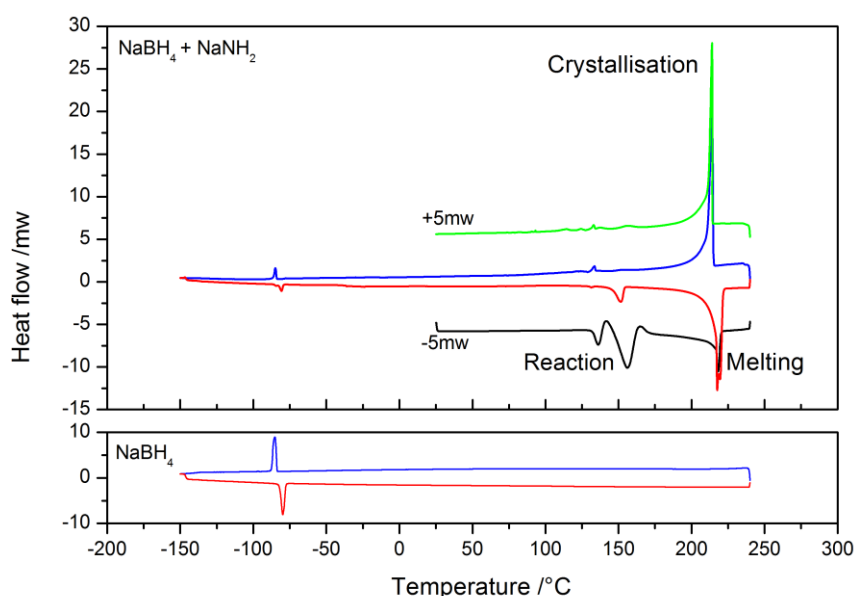


Figure 3.2 Differential thermal scanning calorimetry of the mixture of precursors,  $\text{NaBH}_4$  and  $\text{NaNH}_2$ , which form  $\text{Na}_2\text{BH}_4\text{NH}_2$ . The sample was (a) heated to  $240^\circ\text{C}$  (Black); (b) cooled to  $-150^\circ\text{C}$  (Blue); (c) reheated to  $240^\circ\text{C}$  (Red); (d) finally cooled to room temperature (Green). As a small amount of  $\text{NaBH}_4$  is included as an internal reference, the DSC trace of this sample is included for comparison in the lower box.

(b) X-ray Diffraction

The sample for XRD has been heated to above the melting point and cooled 3 times to access the O-phase of the material. After this annealing of the sample, there is no evidence for the metastable cubic phase (MC-phase) at low temperature. Figure 3.4 shows the powder diffraction refinement of the two structures (O and C phases) giving good agreement between the experimental data and the structures given by Somer et al.[2] The high temperature scan in figure 3.4a was performed at 150°C and the low temperature scan, figure 3.4b, at -170°C to ensure only single phase di-sodium borohydride amide is present.

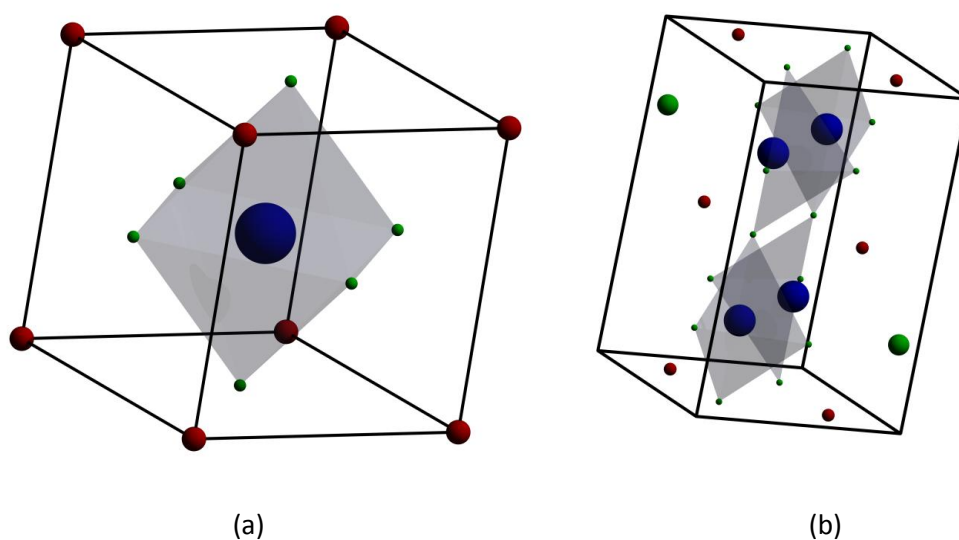


Figure 3.3 The crystal structure of C-phase (a) and O-phase (b) of  $\text{Na}_2\text{BH}_4\text{NH}_2$ . Sodium atoms are represented by the green spheres, Boron the red and nitrogen the blue. For clarity the hydrogen atoms around the nitrogen and boron which form the borohydride and amide ions have been omitted. The grey shaded areas show the shape of the polyhedral around the amide ion formed by the sodium ions.



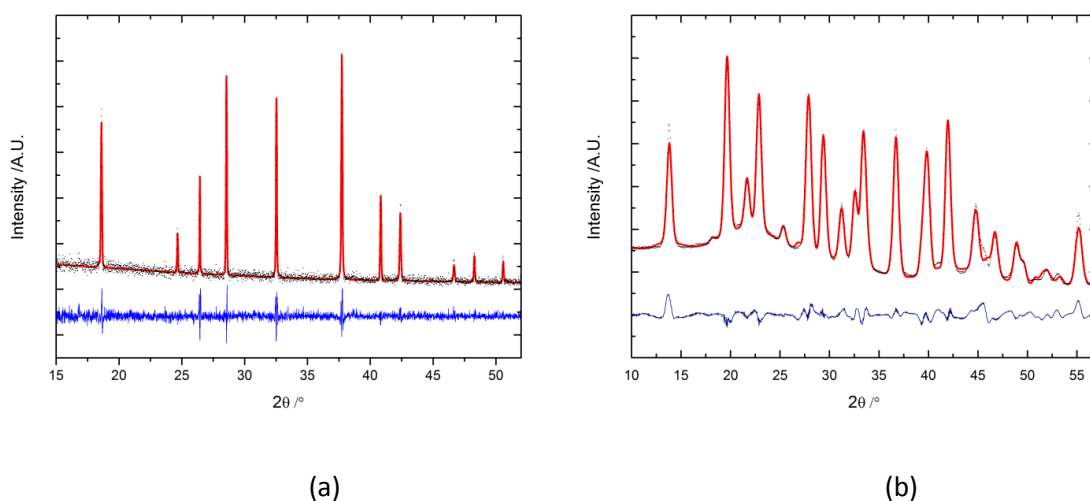


Figure 3.4. Powder refinements of  $\text{Na}_2\text{BH}_4\text{NH}_2$  at  $150^{\circ}\text{C}$  (a) and  $-170^{\circ}\text{C}$  (b). The figures show the experimental data (black), the structural refinement fit (red) and the difference between the experimental data and the fit (blue). Each powder contains an internal reference of Sodium Borohydride the known structure of which has also been accounted for in each scan. The difference in the background and peak shape between the two scans is due to the use of different diffractometers, a high-resolution high-temperature powder diffractometer (left) and a lower resolution single-crystal diffractometer (right) with the powder contained in a glass capillary.

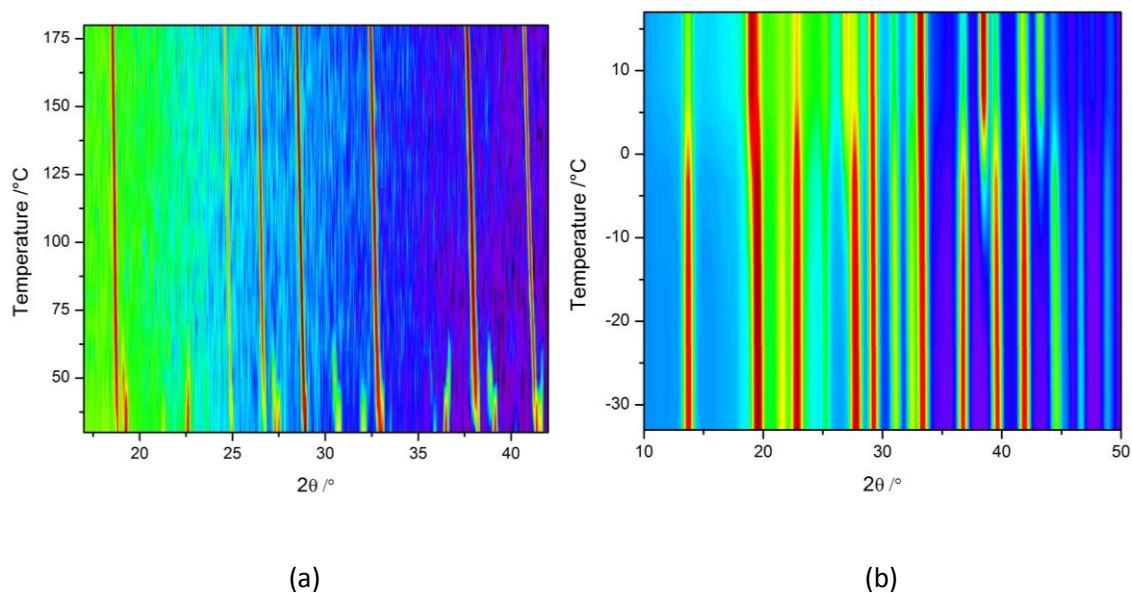


Figure 3.5 XRD stack plots showing the phase coexistence region of  $\text{Na}_2\text{BH}_4\text{NH}_2$  from high temperature runs, between  $30^{\circ}\text{C}$  and  $180^{\circ}\text{C}$ , (a) and low temperature runs down to  $-33^{\circ}\text{C}$  (b).

As previously reported, there are two distinct phases of this material. However, up until now, there has been no x-ray diffraction study performed on this material as a function of temperature. Whilst it is clear that the material only desorbs hydrogen at relatively high temperature, 290°C [1] from the liquid phase, it is probable that it will have to be stored at ambient temperature at times when desorption is not required. As a result the thermal expansion properties of the material have to be known before it could be incorporated into any device expected to operate over such a temperature range. These properties are complicated as there is a known structural phase change at the lower end of this operating temperature range as set out by the DOE targets, given in Table 1.2.

From figure 3.5 it is clear that there is a coexistence region between the high and low temperature phases (C and O phases). Through Rietveld refinement of the individual powder diffraction scans, the temperature range of this coexistence region and the lattice parameters of both phases were determined: a summary of these data are shown in figure 3.6. From here, we see that there is a coexistence region over a wide temperature range, -10 to 70°C, between O-phase and C-phase. At temperatures above 75°C up to the melting point of  $\text{Na}_2\text{BH}_4\text{NH}_2$  (210°C) there is no co-existence of phases and as such, all melting occurs from the cubic phase only- likewise on cooling, all material forms the primitive cubic phase (C-phase).

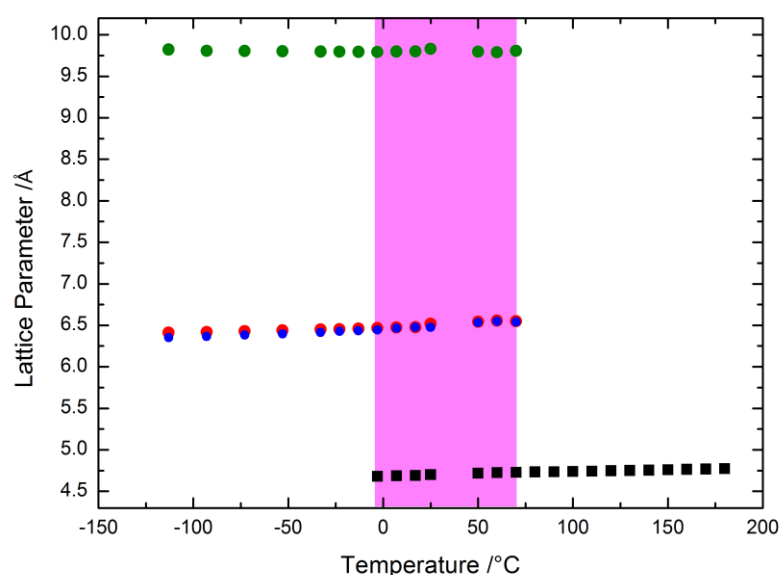


Figure 3.6 The comparison between the lattice parameters of the C-phase of  $\text{Na}_2\text{BH}_4\text{NH}_2$  (black) and the O-phase (circles). The a and b lattice parameters, red and blue respectively, are ca. 6.5Å whilst the c-lattice is ca. 10Å. The co-existence region between the two phases is shown in pink.

Examining the temperature-dependent lattice parameters of these two phases in more detail, it is clear that whereas the a and b lattice parameters of the O-phase exhibit positive thermal expansion as temperature increases, figure 3.7, the c-lattice parameter shows negative expansion, figure 3.8. Closer examination of the a and b lattice parameters show they are expanding at differing rates. Simply looking at the LT-PXRD data, it would seem that these lattice parameters converge at temperatures at the bottom end of the phase co-existence region, at 20°C. However, the HT-PXRD data shows that this is not the case and that indeed the a and b lattice parameters do not converge until the upper limit of the coexistence region at 70°C. The reason for this discrepancy between the two sets of data is that the resolution of the LT-PXRD data is much lower than the HT-PXRD data, as seen in figure 3.4. At the resolution of the LT-PXRD data the 001 peak and the 010 peak cannot be separated; however, they can clearly be seen as two peaks in the HT-PXRD data. Despite this difference in resolution, we can see that the general trend of the lattice parameters as a function of temperature is preserved between the two different sets of data. It is clear that there is definitely a difference in the thermal expansion of each lattice parameter. The variation of the lattice parameters on heating and cooling cycles of the sample are in good agreement, with the values for each temperature being within the experimental error of one another. The evolution of the lattice parameters derived from the LT-PXRD data, appears to be linear with a consistent linear thermal expansion co-efficient between the heating and cooling of the sample. There is one discrepancy at 18°C, (insert figure 3.7), where the lattice parameter variation on heating and on cooling do not agree. As a result of the hysteresis between the two phases, manifest in the relative weight percentages of each phase (associated with the 1<sup>st</sup> order phase change) and the low resolution of this low temperature experiment the Rietveld results between heating and cooling have shown up some discrepancies, such as these lattice parameter variations. These variations are therefore thought not to be physical but only a result of the resolution of the data and the relative amounts of each phase making the refinement unreliable.

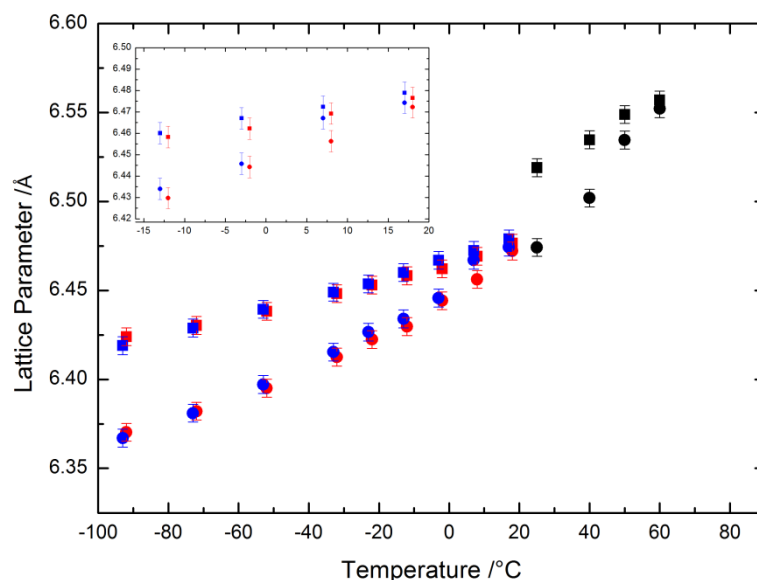


Figure 3.7 a (square) and b (circle) lattice parameter of the O-phase of  $\text{Na}_2\text{BH}_4\text{NH}_2$  during heating (red) and cooling (blue) performed on the LT-PXRD diffractometer. The black data points show the a (square) and b (circle) lattice parameters calculated from the HT-PXRD data during heating.

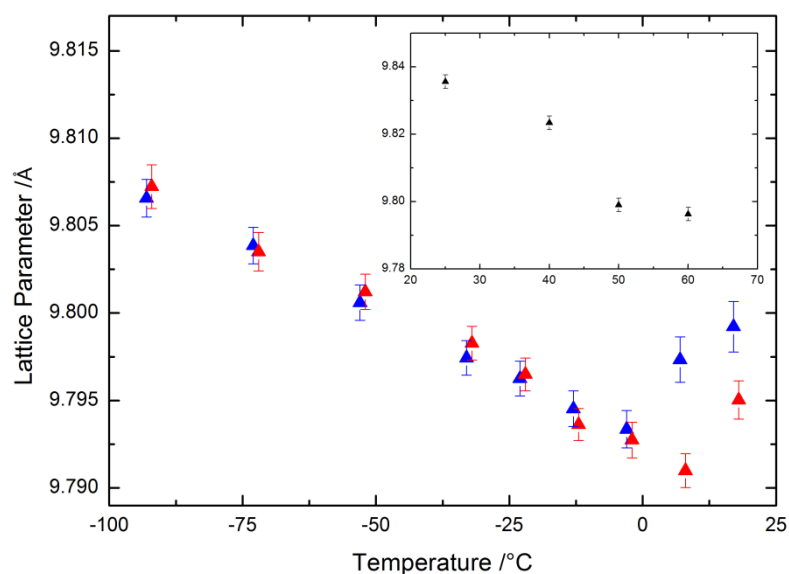


Figure 3.8 c-lattice parameter of O-phase of  $\text{Na}_2\text{BH}_4\text{NH}_2$  during heating (red) and cooling (blue). The insert shows the c- lattice parameter of the O-phase calculated from the HT-PXRD data.

Again the c-lattice parameter shows good agreement between heating and cooling and clearly the overall trend shows negative thermal expansion at temperatures below  $-10^\circ\text{C}$ . As with the b-lattice parameter there is a disagreement between the values as the sample is heated and cooled. Again this is most likely an artefact of the Rietveld refinement due to the result of the difference in the amount of each phase present between heating and

cooling. What is apparent is that the turning point temperature at which the c-lattice parameter switches from negative to positive expansion is consistent between heating and cooling. However when examining the HT-PXRD data (insert figure 3.8) this turning point is not observed and the trend of the c- lattice parameter is to continue negative expansion, albeit at a slower rate, throughout the phase co-existence region. We attribute this discrepancy to the comparatively low resolution of the low temperature diffraction experiment, which is indicated by the large FWHM of the diffraction peaks. The effect is exacerbated when in the co existence region as more peaks are present in the diffraction data leading to overlapping data which is difficult to resolve. Again it is possible to discern the underlying trend in these data that the negative expansion of the c-lattice is continued over the entire coexistence region to the point where all O-phase material has been converted to C-phase. From examining the structural refinement of the data one possible explanation for the negative expansion could be the distortion of the sodium nitrogen chains along the c-axis of the unit cell at temperatures approaching the end of the co-existence region. The positions of the sodium polyhedra relative to the line of the nitrogen atoms are twisted into the ab plane of the cell resulting in the contraction of the c-axis, with a sudden realignment of the sodium nitrogen chains when converting to the C-phase. However by examining the sodium-nitrogen-sodium bond angle along the c-axis, which has been derived from Rietveld refinement of the data, there is no systematic correlation between the sodium nitrogen chains and temperature. The result of these variations in the behaviour of the lattice parameters has resulted in a non-linear volume expansion of the O-phase, the positive expansion of the a and b lattice outweighs the negative expansion of the c-lattice to give an overall positive thermal volume expansion - however this expansion is tempered by the behaviour of the c-lattice parameter, figure 3.9. At the perceived operating temperatures, above  $-40^{\circ}\text{C}$ , of any hydrogen storage device, the thermal expansion of the material is close to linear with the effect of the negative thermal expansion of the c-lattice only having a discernible effect at lower temperatures, far below the temperatures that any such device would be expected to experience in normal operation.

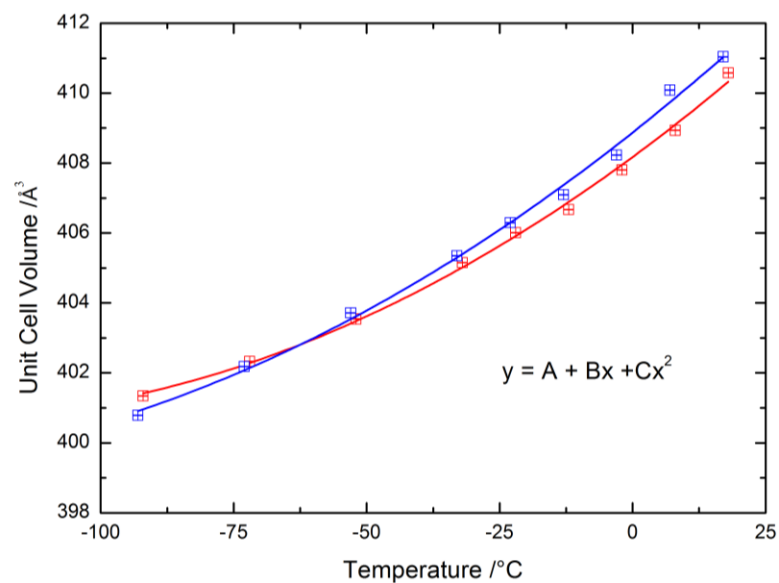


Figure 3.9 unit cell volume of O-phase  $\text{Na}_2\text{BH}_4\text{NH}_2$  calculated from lattice parameters during sample heating (red) and cooling (blue). The volume expansion is fitted to a polynomial resulting in slight differences in the fitting parameters.

Fitting Parameter	Heating	Cooling
A	408(1)	409(1)
B	0.112(4)	0.120(5)
C	0.00042(6)	0.00038(7)
Adj. R-Square	0.9965	0.9953

Table 3.1 volume fitting parameters of low temperature  $\text{Na}_2\text{BH}_4\text{NH}_2$  during heating and cooling along with goodness of fit parameters.

Firstly, as the values in table 3.1 show, there is relatively good agreement between the fitting parameters between the volume change during heating and cooling, as well as this the values show that there is only a small, 0.4%, non-linear contribution to the fitting as a result of the negative expansion described above.

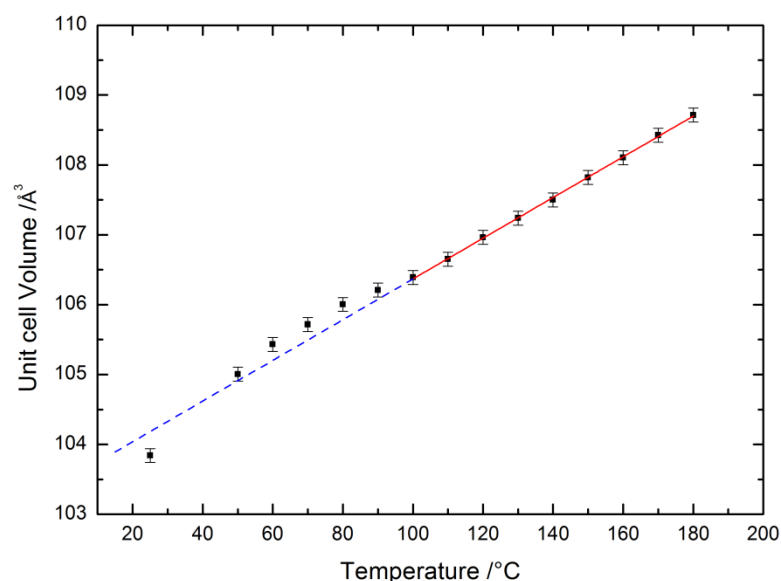


Figure 3.10 cubic unit cell volume of  $\text{Na}_2\text{BH}_4\text{NH}_2$  the red line is a linear fit over the range shown and the blue line is an extrapolation of this line down to lower temperatures.

At high temperatures this material has a primitive cubic (C-phase) structure which exhibits a linear thermal expansion up to the melting point of  $\text{Na}_2\text{BH}_4\text{NH}_2$ ; the calculated volume of the unit cell as a function of increasing temperature is shown in figure 3.10. There is a slight deviation from linearity at temperatures below 80°C, which could be due to the presence of the O-phase as these temperatures are within the co-existence region. This may also be exacerbated by the reliability of the temperature reading of the furnace in this range, where the thermocouple employed is less reliable as it is designed to be effective at high temperature, thermocouples are less suited to low temperature (0-100°C) measurements. From the volumetric comparison between the cubic and orthorhombic cells, there are four formula units per unit cell which is consistent with the structural crystallographic data reported by M. Somer et al.

By examining a sample of non-annealed cubic  $\text{Na}_2\text{BH}_4\text{NH}_2$  it is possible to collect metastable cubic (MC-phase) lattice parameters down to a lower temperature than -10°C. This sample shows no evidence for the low temperature phase at room temperature, unlike the annealed sample. The results from this LT-PXRD experiment are given in figure 3.11, which shows a broadly linear relationship. There is an apparent change in this linearity around -10°C, which is due to the introduction of small amounts of the O-phase. However, the MC-

phase is present to much lower temperatures than the C-phase seen in the annealed samples discussed above. By comparing the results shown in figures 3.10 and 3.11 the expansion of this MC-phase is seen to be very different from that of the C-phase.

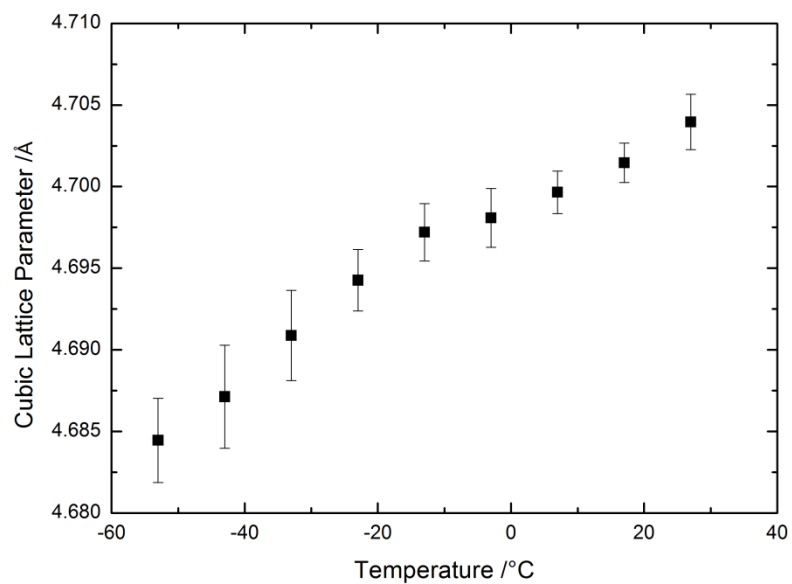


Figure 3.11 Cubic lattice parameters of the MC-phase of  $\text{Na}_2\text{BH}_4\text{NH}_2$

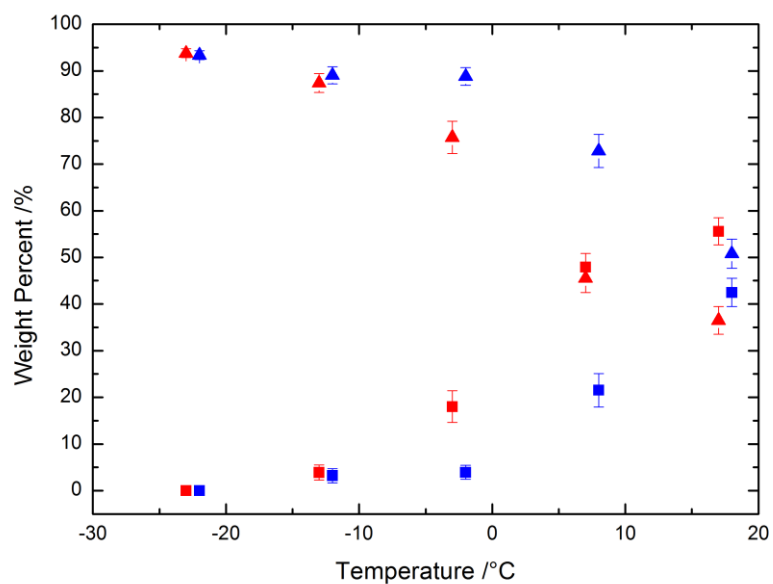


Figure 3.12 Relative Rietveld weight percentages of C-phase (squares) and O-phase (triangles) of  $\text{Na}_2\text{BH}_4\text{NH}_2$  during heating (red) and cooling (blue)



From Rietveld refinement the relative weight percentages of each phase has been determined (figure 3.12). There is a difference between the weight percent of each structural phase between heating and cooling. During heating, the phase change from the O-phase to the C-phase is quicker than the reverse change during cooling and likewise, during cooling, the O-phase is more readily formed. It seems that the reversibility of this phase change is dependent on the direction of the temperature change. This indicates that it is a slow 1<sup>st</sup> order phase change, which is consistent with the large phase co-existence region shown in the x-ray analysis. During cooling Na<sub>2</sub>BH<sub>4</sub>NH<sub>2</sub> becomes orthorhombic at a greater rate than the reverse during heating thereby changing the overall volume of the material differently from when it is heated. The C-phase is formed more readily and has the effect of causing a discrepancy in the overall volume of the material in the phase co-existence region between heating and cooling. This will have an effect on the thermal stability of the material and may affect its usefulness in a hydrogen storage system in temperature variable environments. By combining the relative percentage between the two phases with the volume of each phase at a given temperature, it is possible to calculate the overall volume per formula unit of the material (Equation 3.1).

$$V_{FU}(T) = \frac{V_{orth}}{Z_{orth}} \frac{wt_{(\%)_{orth}}}{100} + \frac{V_{cub}}{Z_{cub}} \frac{wt_{(\%)_{cub}}}{100} \quad (3.1)$$

Where  $V_{FU}$  is the volume per formula unit of the material, the subscript 'orth' relates to the orthorhombic (O) phase and 'cub' the cubic (C) phase, all other symbols have their standard meaning. This discrepancy in the overall sample volume between when being heated and cooled can be seen in figure 3.13 and could have consequences if the material was used in large quantities as the change in the volume of the material would be different for heating and cooling possible leading to degradation of the material through repeated heat cycles.

Figure 3.13 shows that the volume per formula unit during cooling is consistently higher than the corresponding volume during heating over the range of the co-existence region. This is a result of the volume per formula unit of orthorhombic Na<sub>2</sub>BH<sub>4</sub>NH<sub>2</sub> being slightly higher than the corresponding value for the C-phase polymorph. The large discrepancy between the two values at 18°C is a result of the aforementioned differences in the lattice

parameters between heating and cooling. This difference between heating and cooling volumes would only be exaggerated with heating rates greater than those used in these experiments- at the higher rates what would be expected in any practical device, it would be possible that this effect is greatly enhanced. These effects would have to be considered very carefully when designing such a hydrogen storage device. By having to allow more volume for the material to expand into when cooling down from operating temperature the overall volumetric efficiency of any hydrogen storage device would therefore be reduced.

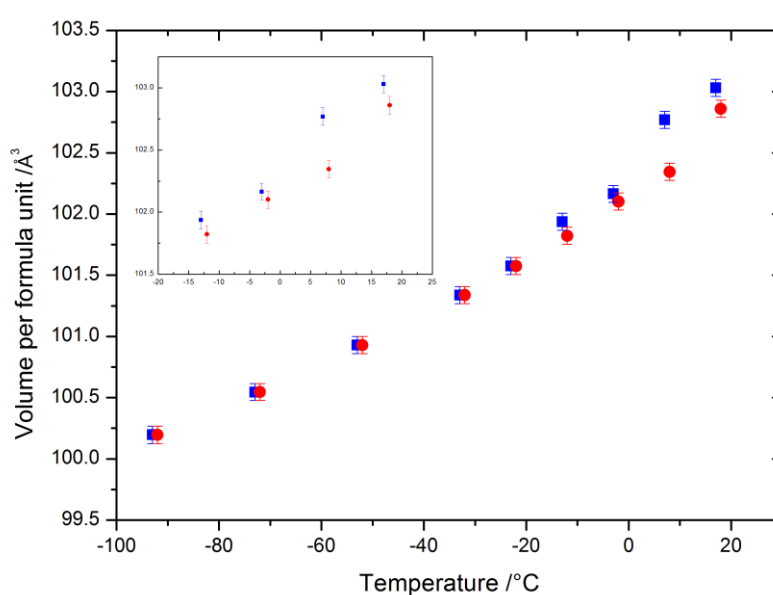


Figure 3.13 volume per formula unit of  $\text{Na}_2\text{BH}_4\text{NH}_2$ , during heating (red) and cooling (blue), calculated from the volume of each polymorph weighted against the weight percent of each phase at a given temperature.

### 3.3.2 Single Crystal Results

From examining the results of single crystal growth, it is apparent that  $\text{Na}_2\text{BH}_4\text{NH}_2$  readily precipitates out of the liquid phase of the sample during cooling. As the sample cools and crystallizes it forms single crystals of the cubic phase. At room temperature single crystals were identified using a polarising microscope quantifying candidates for diffraction according to their optical quality – in particular, optical isotropy as expected for a cubic crystal and lack of strain or cracking. Only crystals of the cubic phase were found, As mentioned above crystals with potential for x-ray diffraction were then quick frozen under 100K nitrogen this had the effect of freezing in the crystal in MC-phase seen in figure 3.11,

as the same powder sample was used to produce these single crystals. At low temperature as seen in the 0kl plane of reciprocal space with all the observable Bragg peaks lying on a cubic lattice, figure 3.14. The results from the refinement of this lattice are given in table 3.2. These results agree well with the results from the structural powder analysis presented by M. Somer et al. [2] even though this crystal is in a MC-phase and not the C-phase examined in [2].

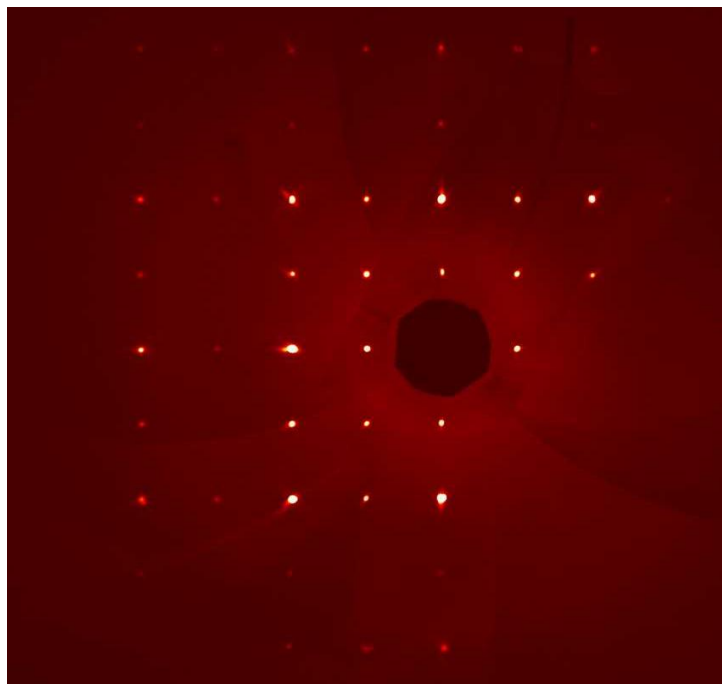


Figure 3.14 The 0kl plane from single crystal diffraction of MC-phase of  $\text{Na}_2\text{BH}_4\text{NH}_2$  at 100K

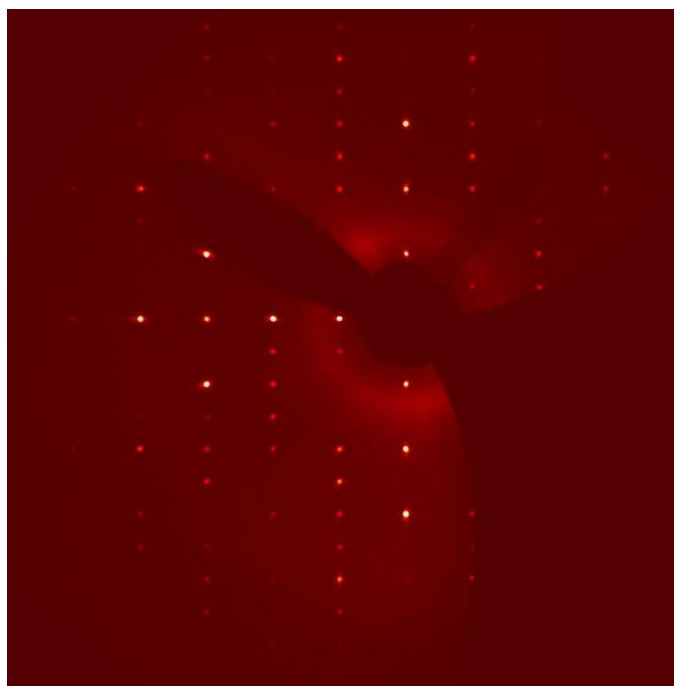


Figure 3.15 The 0kl plane from single crystal diffraction of the O-phase of  $\text{Na}_2\text{BH}_4\text{NH}_2$  at 100K

Crystal System	Cubic	Orthorhombic
Space Group	Pm-3m	Pbcm
Lattice parameter, a, ( $\text{\AA}$ )	4.665(1)	6.475(1)
Lattice parameter, b, ( $\text{\AA}$ )	--	5.253(1)
Lattice parameter, c, ( $\text{\AA}$ )	--	10.741(2)
Unit Cell Volume ( $\text{\AA}^3$ )	101.5(1)	365.4(1)

Table 3.2 The results of lattice fitting of single crystal diffraction

As all the crystals formed from cooling the melt are in the cubic phase, to form an orthorhombic crystal, a cubic crystal was first removed from the oil and stored under a protective atmosphere for several days after which time the crystal was examined using single crystal XRD to determine its crystal lattice. Figure 3.15 shows the reciprocal lattice plane 0kl from the O-phase. The results of the lattice refinement from both polymorphs are presented in Table 3.2. The results for the MC-phase crystal are not consistent with a contraction of the cubic, C-phase, lattice described by the HT-PXRD data in figure 3.10, the unit cell volume in table 3.2 does not follow the linear expansion trend seen in the figure it is considerably higher than would be expected if the graph was extrapolated down to the single crystal measurement temperature. This is further proof of this cubic phase being the metastable, MC-phase, and deviant from the general trends of the C-phase crystal.

Comparing the lattice parameters of this crystal with the MC-phase results given in figure 3.11 the results are consistent with the lattice expansion described there. The results for the O-phase crystal show that the lattice parameters are as expected given the direction of the thermal lattice expansion described above and LT-PXRD results. However, it is difficult to extrapolate a line of fit to the data in figure 3.7 and so the expected lattice parameters at this temperature are difficult to determine. There is a large discrepancy between the expected lattice volume of the O-phase based on the volume thermal expansion given in table 3.1 and the calculated unit cell volume given in table 3.2. This discrepancy could be a result of the unreliable determination of the trend in volume expansion given the low resolution results of the LT-PXRD experiment. Furthermore the relation between the unit cell volumes of the MC-phase and O-phase polymorphs at 100k seems to suggest that there are less than 4 formula units percent in the O-phase or that the MC-phase unit cell volume is higher than it should be- this is most likely the case as the MC-phase is not the native C-phase at these temperatures. Extrapolating the C-phase volume expansion given in figure 3.10 the cubic lattice volume should be much lower at this temperature. The structural refinement of this MC-phase has proved difficult, whilst being mindful of the total experiment length- to reduce the impact of any sample degradation due to exposure to oxygen and moisture, it has been possible to collect data to a significant resolution, down to 0.6Å in d-spacing, with a good level of redundancy over the entire Ewald sphere. However, the internal R-factor for this data has proved less than desirable with an average value of 0.21. This indicates that the quality of the crystal is questionable; in addition to this the internal R-value is greater at lower d-spacing this is due to the very low intensity of these reflections- as the material contains only light elements. Even using the structure of the C-phase as a starting point, it has been not been possible to get a fit with a fitting parameter (R-value) less than 0.25, which makes it impossible to confirm the structure of the single crystal. The most likely cause of this discrepancy is the inherent disorder in the crystal due to the only 2/3 filling of the octahedra; whilst the O-phase would indicate that the partially-filled octahedra are ordered. This is not seen in the single crystal structure most likely as the crystals were not derived from the O-phase and instead were grown out of the melt which will have resulted in a random distribution of filled octahedra sites within the crystal giving the averaged cubic structure seen in figure 3.1(a). The consistency of the results from the O-phase is much better with an average internal r-value of 0.055 and whilst the resolution of the experiment is similar to that of the MC-phase data the redundancy of this data is much lower which may mask the actual quality of the data.

Again, the internal R-values of this data increase at higher d-spacing which is to be expected with a weakly diffracting sample, such as this, over a relatively short experimental exposure time. Attempts to solve the crystal structure of this O-phase have proved as fruitless as the MC-phase. Whilst the structure is not expected to be as disordered as the MC-phase; it has still proved difficult to solve the structure either from the expected structure or from scratch with the best R-values of 0.6 and 0.2, respectively.

### 3.4 Conclusions

Whilst work has been published on the crystal structure of both O and C structural phases of  $\text{Na}_2\text{BH}_4\text{NH}_2$  and also what happens to the material as it is heated above its melting point but no other work has shown the crystallographic properties of  $\text{Na}_2\text{BH}_4\text{NH}_2$  at the various temperatures that would be required if this material was used in a hydrogen storage device. The structure of the material is stable from temperatures ranging from  $-100^\circ\text{C}$  up to  $220^\circ\text{C}$  where the material melts. There are no unreported phases observed between these temperatures and only one phase transition is observed. There is a large co-existence region between the O and C phases which occupies the lower end of the perceived operational temperature range. Whilst the upper and lower temperatures of this region do not change between heating and cooling the relative amount of each phase is dependent on the heat flow around the sample. Due to the slight variation in the density of these two structures this changes the overall volume of the sample between heating and cooling whilst these variations are resolved at either end of the co-existence region. This will affect any potential hydrogen storage device as extra volume will be required to allow for the abnormal expansion during cooling, thereby reducing the overall volumetric efficiency of this material. A metastable cubic phase has been identified that exists within the sample before it has been annealed; this phase can be seen at temperatures below the coexistence region where the C-phase should not be present. The thermal expansion of this metastable phase is very different to the high temperature cubic (C) phase. The single crystal experiment has shown that this metastable phase is present at very low temperatures ( $-173^\circ\text{C}$ ) when rapid cooling is employed. This may have an effect on the usefulness of this material as heating and cooling rates would have to be curtailed as not to damage the macroscopic material structure (cracking) or surrounding substructure from radical changes in unit cell volume. Reduced heating times would result in longer start up times for any hydrogen fuel system and, conversely, it's possible that the cooling of this material would

have to be controlled when the system is shutdown further eroding the energy efficiency of the fuel system.

### 3.5 Further Work

There are several areas of further work which would help create a more complete picture of the behaviour of this material across the phase change region. Higher resolution LT-PXRD would help to confirm the structure of the low temperature (O) phase and the structural mechanism responsible for the negative expansion of the c-lattice in this phase.

There are similarities in the room temperature, C-phase of  $\text{Na}_2\text{BH}_4\text{NH}_2$  and that one of the constituent materials  $\text{NaBH}_4$ . In addition, there is a similar low temperature phase in sodium borohydride the transition to which is seen in figure 3.2. Continuing from this there is a well published pressure induced phase change in  $\text{NaBH}_4$  [6-7] which may be something that can be replicated in this material. High pressure may force the crystal into a new phase which could provide information on the disorder in the room temperature (C-phase) structure and also a combined pressure-temperature study may offer insight into hydrogen desorption from the material at elevated pressure, possibly directly from the solid state.

Another area of additional work is with single crystal samples which offer more information on which to base a structural refinement. This work has shown that it is possible to grow single crystals from the liquid phase the next step would be to try and improve the quality of these crystal, possibly by annealing to try and order the octahedral vacancies this should allow for a more accurate single crystal structural refinement of the MC-phase. Another way to improve the data collected from these single crystals would be to use high intensity synchrotron x-ray diffraction which would allow for greater signal to noise to improve the internal R-values of the data without the need to use longer exposure times. As the material contains only light elements neutron diffraction may also be useful as these elements have a larger scattering cross section than with x-rays. However in this case the samples would need deuterating which may prove difficult given the sample's air and moisture sensitivity and the synthesis method used.

## References

- [1] P.A. Chater, P.A. Anderson, J.W. Prendergast, A. Walton, V.S.J. Mann, D. Book, W.I.F. David, S.R. Johnson, P.P. Edwards, J. Alloys Compd. 446–447 (2007) 350–354.
- [2] Mehmet Somer, Selçuk Acar, Cevriye Koz, Ilkin Kokal, Peter Höhn, Raul Cardoso-Gil, Umut Aydemir, Lev Akselrud, J. Alloys Compd. 491 (2010) 98-105
- [3] Yaroslav Filinchuk, Hans Hagemann, Eur. J. Inorg. Chem. (2008) 3127-3133
- [4] Agilent (2010). *CrysAlis PRO*. Agilent Technologies, Yarnton, England.
- [5] <http://www.topas-academic.net/>
- [6] Y. Filinchuk, A. V. Talyzin, D. Chernyshov, V. Dmitriev, Phys. Rev. B 76 (2007) 092104
- [7] R. S. Kumar, A. L. Cornelius, Appl. Phys. Lett. 87 (2005) 261916



# Chapter 4

## Homoepitaxial Growth of Nitrogen-doped Antimonides

### 4.1 Introduction

The structure of Gallium Antimonide (GaSb) and Indium Antimonide (InSb) is well known as a Zinc Blende cubic crystal structure, space group  $F\bar{4}3m$ , with each atom species tetrahedrally coordinated (figure 4.1). The structure is closely related to diamond, which has a tetrahedrally coordinated structure where all the atoms are of the same species. The cubic lattice parameter and the Poisson's ratio of these materials are listed in table 4.1; these are the parameters used to simulate and fit the data presented in this chapter.

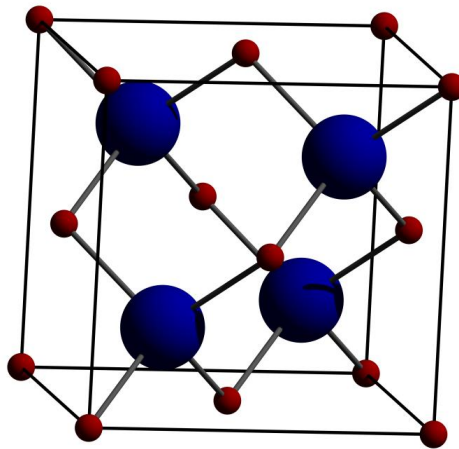


Figure 4.1 The Zinc Blende structure of indium and gallium antimonide. The A-site(red) is defined as the anion position and the B-site(blue) is the position of the cation, in this case antimony.

	Gallium Antimonide, GaSb	Indium Antimonide, InSb
Cubic Lattice Parameter /Å [1]	6.096	6.479
Poisson Ratio [2]	0.313	0.348

Table 4.1 Structural properties of gallium and indium antimonide used in the fitting of the diffraction data presented in this chapter.

In order to modify the band gap of intrinsic semiconductors such as GaSb and InSb, the structure of these materials has to be modified by substituting other elements into the structure. It has been shown that substituting dilute quantities of nitrogen, up to approximately 6%, onto the B site of these materials can significantly reduce the overall band gap. The effect on antimonide materials is larger than that of arsenides because of the greater difference in electronegativity between nitrogen and antimony than that between nitrogen and arsenic. As a result, these materials have seen a renewed interest as a smaller percentage of nitrogen incorporation is required in the structure to produce similar effects to that of the analogous arsenides. [3] The reduced amount of nitrogen inclusion should increase the crystal quality of the resultant layer as less lattice distortion and therefore less stress should be induced in the material. Conversely, the narrower nitrogen incorporation window means that finer control of the growth of these materials is required, as small changes in nitrogen content result in larger changes in the properties of these antimonide materials compared with the arsenic-based ones.

## 4.2 Sample Growth

All of the epilayer samples discussed in this chapter were grown using plasma assisted molecular beam epitaxy (MBE) by Dr Mark Ashwin, a member of the chemistry department at the University of Warwick. Commercially grown, un-doped GaSb(001) and InSb(001) wafers were used as the substrates for sample growth. The wafers were mounted in a Gen II chamber and outgassed at 300°C for the GaSb samples and 200°C for the Indium based materials. After this the oxide layer was thermally removed, under a flux of antimony, at temperatures around 500-570°C for GaSb and approximately 200°C lower for the indium based samples. Reflected high energy electron diffraction (RHEED) analysis was used on the substrate to check the quality of the prepared surface before growth commenced. The gallium and indium flux was provided by a Sumo cell and the antimony by a valved Addon cell with the valve operated at a temperature of 800°C. The nitrogen flux was supplied at ultra-high purity by a SVTA plasma source operating at a constant 500 W and a flow rate of 0.2 standard cubic centimetres (sccm). Substrate temperatures were determined from thermocouple readings or by extrapolating pyrometer readings from above 450°C. Prior to growth of the nitride layer, an appropriate buffer layer of GaSb or InSb was grown on the prepared substrate surface to give an atomically flat surface for the nitrogen containing layer to be grown upon. The GaSb layer was grown at a temperature of 500°C at a rate of  $0.50\mu\text{m h}^{-1}$  with a V:III ratio of 1.5:1. The expected surface reconstruction of this layer (1x3)

was observed using RHEED. Similarly, the same procedure was used to grow InSb buffer layers; however, the growth temperature used was around 370°C. Following buffer layer growth, the nitrogen plasma source was struck in a sealed chamber, to avoid nitrogen contamination of the epilayer surface, and the Ga/In cell temperature set for the required growth rate. Additionally, the required substrate temperature was achieved by cooling the GaSb/InSb substrate from 500/370°C. The Sb cell valve was then adjusted to yield a V:III ratio of 1.5:1 for substrate temperatures above 350°C and 1.2:1 for temperatures below 350°C in order to avoid antimony build-up on the surface during growth. Growth was then commenced by opening the Ga/In cell shutter and nitrogen gate valve and shutter, the epilayer surface being monitored throughout the growth using RHEED, which indicated a well ordered surface. Growth was continued until a nominal thickness of 400nm was achieved after which, growth was stopped, the sample cooled and removed from the growth chamber.

### 4.3 Sample characterisation

The as-grown samples were examined using high resolution XRD by collecting high-resolution rocking curves (RC) around the 004 reflection and reciprocal space mapping of the 004 and 024 reflections, where appropriate. Samples were mounted in a PANalytical X'pert pro MRD diffractometer equipped with a hybrid monochromator to give  $\text{CuK}\alpha_1$  radiation. The diffracted beam optics consisted of a triple-axis analyser crystal and a point detector. In order to collect a rocking curve, the sample was first aligned such that the surface of the sample was parallel with the incident x-ray beam and the height of the sample was adjusted such that it half-cut into the beam. Then the sample was aligned to the 004 reflection of the substrate using the diffracted-beam point detector without the analyser crystal. This was used initially to give a larger angular acceptance into the detector in the  $2\theta$  axis to aid in locating the reflection. The sample was then aligned in  $\omega$ ,  $\phi$ , and  $\psi$  to obtain the optimal intensity from the reflection by aligning the lattice vector with the detector. To determine the  $2\theta$  position more precisely, the analyser crystal was then inserted to improve angular discrimination and, therefore, resolution. Once aligned in all axes, an omega-2theta scan was performed over a range of omega relative to the substrate reflection, resulting in an  $\omega$  range of up to 1° with a step size of 0.0005° and count time per step of 8 seconds. These settings result in a total scan time of 3 hours. An example of this type of measurement is shown in figure 4.2.

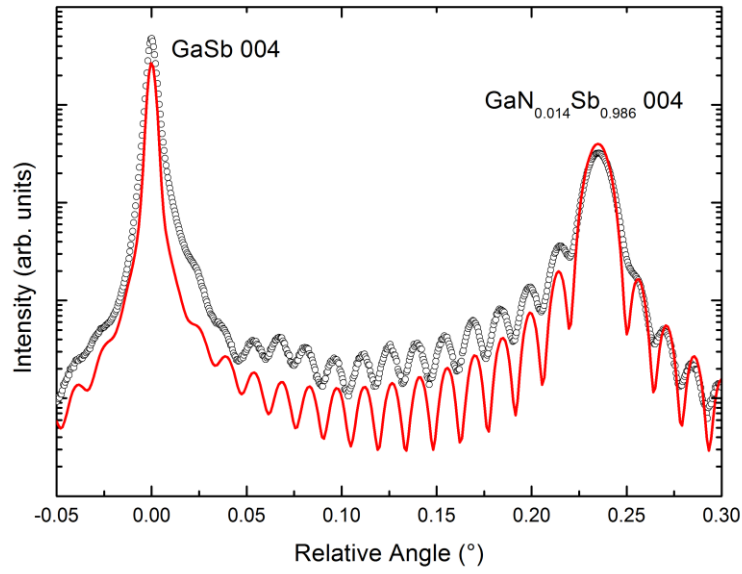


Figure 4.2 HR-XRD(open circles) of the 004 reflection of GaSb substrate with a 1.4% nitrogen containing epilayer, a simulation of the sample is shown, red line.

In order to determine the nitrogen concentration of the epilayer, it is necessary to model the diffraction pattern using the PANalytical X'pert Epitaxy software. Using the angular position of adjacent Pendellösung fringes, it is possible to determine the thickness of the sample,  $t$ , from equation 4.1.

$$\delta\omega = \frac{\lambda \sin(\varepsilon)}{t \sin(2\theta)} \quad (4.1)$$

Where  $\varepsilon$  is the angle between the diffracted beam and the surface of the sample i.e. the average  $2\theta$  minus  $\omega$  values of the fringes and  $2\theta$  is the averaged value of the two adjacent fringes. This thickness value was then used as the starting thickness when modelling the sample using the software. For this the sample was modelled as a 100% strained dilute nitrogen-containing layer on a homoepitaxial substrate. The contraction of the lattice parameter of the nitrogen-containing layer is modelled using Vegard's law using the lattice parameters given in Table 4.1 and end-point lattice parameters of cubic-GaN of 4.50Å [4] and cubic- InN of 4.98Å [5]. An approximate nitrogen incorporation percentage was used to construct the initial model of the sample. Other parameters included in the modelling include an instrument function, a convolution of the beam profile with that of the hybrid monochromator and a variable intensity multiplier, which increases the overall intensity of

the simulation to match the experimental data. Other refinable parameters can be added to the fitting in order to improve the overall quality of the fit such as a background counts term and a signal-to-noise term. However, both of these terms are not needed as the scans have little noise and a flat background (figure 4.2). A least-squares fitting algorithm is then used to vary the three parameters- nitrogen concentration, thickness and intensity- to give the best fit to the observed data. From this fitting the thickness and, more importantly, the nitrogen incorporation percentage for each sample, are extracted, with results as discussed below.

For some of the  $\text{GaN}_x\text{Sb}_{1-x}$  layers, additional x-ray analysis was performed by examining both a symmetric 004 and asymmetric 024 reflections in tandem using reciprocal space mapping (RSM). This allows for additional information about the orientation and relaxation of the epilayer relative to the substrate to be extracted (as detailed in chapter 2). The procedure for conducting these experiments is similar to that for rocking curves discussed above; the sample is again positioned in the half-cut beam with the surface parallel to the straight through beam. The sample is aligned to the asymmetric 024 peak in a similar manner to previously using an open detector for the  $\omega$ ,  $\phi$  and  $\psi$  axes and the analyser crystal for the alignment of  $2\theta$ . At this point the orientation of the sample is changed to align the symmetric reflection 004, which is done in the same way as described above for a rocking curve *except that* the azimuthal angle,  $\phi$ , is fixed between the two measurements.

The size of the area scanned to collect the symmetric RSM was set to  $0.8^\circ$  in the  $\omega$ - $2\theta$  direction with a step size of  $0.002^\circ$  and count time per step of 0.2 seconds. The range in the  $\omega$  direction was  $0.5^\circ$  at a resolution of  $0.002^\circ$ . The scan settings for the asymmetric diffraction peak were a range of  $0.6^\circ$  in the  $\omega$ - $2\theta$  direction, at a resolution of  $0.001^\circ$  and a time per step of 0.25 seconds, and a range of  $0.9^\circ$  in the  $\omega$  direction at a resolution of  $0.005^\circ$ .

## 4.4 Experimental Results

### 4.4.1 InNSb Grown on InSb

Layers of  $\text{InN}_x\text{Sb}_{1-x}$  were grown on InSb substrates as a function of both growth temperature, between  $270^\circ\text{C}$  and  $360^\circ\text{C}$ , and growth rates of  $0.44\ \mu\text{m h}^{-1}$  and  $0.75\ \mu\text{m h}^{-1}$ . The results from the rocking curve experiments are given in figure 4.3, which shows two datasets for different growth rates. All the samples were grown to a nominal thickness of

400nm; this thickness was confirmed, where possible, by modelling the Pendellösung fringes seen in the x-ray profiles as discussed earlier in this Chapter.

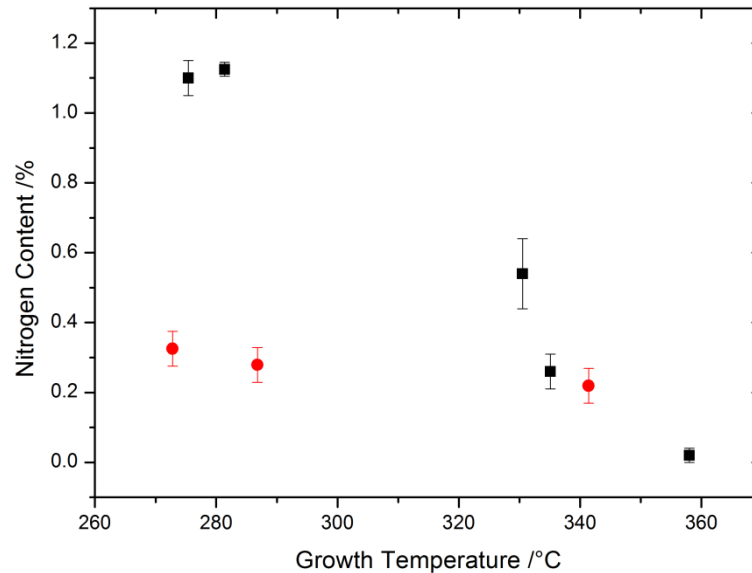


Figure 4.3 Nitrogen incorporation percentages determined from analysis of RC data for InNSb samples grown on InSb at a growth rate of  $0.44 \mu\text{m h}^{-1}$  (black) and  $0.75 \mu\text{m h}^{-1}$  (red).

The figure shows a linear correlation between growth temperature and the amount of nitrogen that can be incorporated into the structure for both of the growth rates examined. This behaviour is consistent with previous studies of this type of growth on other substrates [3]. Samples grown more slowly, at  $0.44 \mu\text{m h}^{-1}$ , show a higher degree of nitrogen incorporation at a given temperature than those grown more quickly. The difference in the amount of nitrogen incorporation is greater at lower growth temperatures leading to a difference in the nitrogen incorporation rate as a function of temperature. This is consistent with studies of  $\text{GaN}_x\text{Sb}_{1-x}$  layers on GaSb which have shown that reducing the growth rate improves the nitrogen incorporation [6]. Therefore, not only is the growth temperature important for the incorporation of nitrogen into the layers, but also the growth rate is also important, especially at lower temperatures. Therefore, the growth rate must be very precisely controlled as even slight changes can have a large effect on nitrogen incorporation. Extrapolating the data in figure 4.3 gives an upper bound for the growth temperature at which nitrogen incorporation is still possible - for samples grown at  $0.44 \mu\text{m h}^{-1}$ , this temperature is  $360(2)^\circ\text{C}$ . Indeed, the sample grown at  $358^\circ\text{C}$  shows a level of nitrogen incorporation,  $0.02(1)\%$ , which is only just detectable using this technique. The upper temperature bound for the samples grown at higher rates is more difficult to

determine as the differences in nitrogen incorporation are small. Additional work would be required to determine this temperature limit more precisely. However, as the goal of this research is to improve the degree of nitrogen incorporation, it is unlikely that this will be pursued further as the higher growth rate is less effective in producing samples with adequate nitrogen incorporation in any case. One area where this growth rate dependence may be used is to control precisely nitrogen incorporation if the rate cannot be adequately controlled by growth temperature alone. This analysis has been helpful in determining the upper temperature limit for nitrogen incorporation, 360(2)°C for InNSb samples. However, it is more difficult to determine the lower temperature limit as no samples have been grown at temperatures where nitrogen incorporation has stopped or even been significantly reduced. Figure 4.3 shows that the samples grown at 270°C exhibit the highest nitrogen content but no layers were grown at temperatures lower than this. Previous work [3,6] has concentrated on temperatures over this range as the nitrogen incorporation in samples over this range has been modelled successfully using kinetic modelling [6]. This modelling showed that the nitrogen incorporation at lower temperatures is expected to remain constant. The temperatures investigated produced samples with desirable bandgap reduction; it was also shown that with increased nitrogen incorporation over the dilute amounts shown in this work causes the bandgap to increase again [3]. Furthermore, additional nitrogen incorporation has a measurable effect on the strain within layer, as it reduces the lattice parameters of the layer relative to the substrate.

By examining the FWHM of the layer peak seen in the RC scans, we have examined both the strain and the crystal quality of the layer (figure 4.4). Clearly, the layers grown at a higher growth rate exhibit a lower FWHM and hence higher crystal quality. This is somewhat counter-intuitive as it would be expected that layers grown at a slower rate give the deposited material a greater chance of reducing strain before additional monolayers are deposited on the sample. However, we have already seen that the layers grown more quickly have less nitrogen incorporation, thereby reducing the lattice mismatch between the substrates and the layer and the resulting epitaxial strain. The layers grown at the lower rate with comparable amount of nitrogen incorporation have a much larger FWHM even given the same lattice mismatch. The strain within the sample layers grown at 0.44  $\mu\text{m h}^{-1}$  seems to be reduced in samples with higher nitrogen content (black, figure 4.4) indicating that despite the larger lattice mismatch, the crystal quality of the layers is improved. This implies that the growth temperature of the layer has a noticeable effect on the quality of the material that is grown, especially at this reduced growth rate. Our results

suggest that the quality of the grown layer is influenced more by the temperature of growth than by the overall nitrogen incorporation. These results suggest that not only is there a trade off between the layer growth rate and the nitrogen content, but also a third compromise in how the growth rate affects the crystal quality. The higher the growth rate the better the quality of the resultant sample, but less nitrogen is incorporated. Therefore, these two effects have to be balanced to produce samples with the closest to the desired properties. The best sample investigated here was grown at  $0.44\mu\text{m h}^{-1}$  at a temperature of  $275^\circ\text{C}$  to give a high incorporation of nitrogen (c.a. 1.1%) with a low FWHM of c.a.  $0.013^\circ$ .

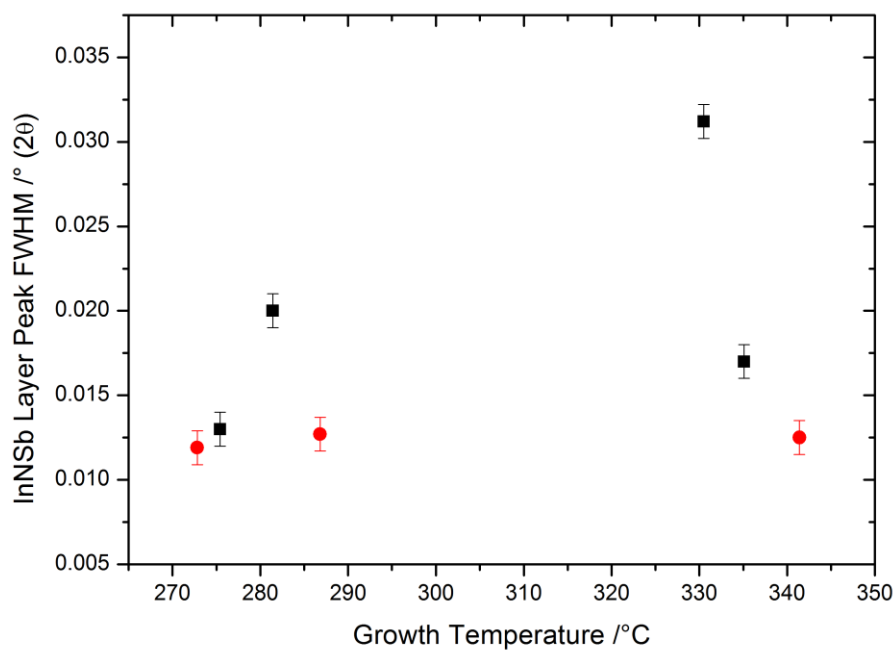


Figure 4.4 FWHM of the InNSb layer peak seen in the RC x-ray scans from samples grown at  $0.44\mu\text{m h}^{-1}$  (black) and  $0.75\mu\text{m h}^{-1}$  (red).

#### 4.4.2 GaNSb Grown on GaSb

Layers of  $\text{GaN}_x\text{Sb}_{1-x}$  grown on GaSb were also studied, initially in a similar manner to the  $\text{InN}_x\text{Sb}_{1-x}$  system, namely by examining the 004 diffraction peak using x-ray RC scans. The initial results of this analysis are given in figure 4.5, which shows that, like in the  $\text{InN}_x\text{Sb}_{1-x}$  system, there is again a strong correlation between growth temperature and nitrogen incorporation. This relation has been seen in previous studies of samples grown in this temperature range [3,6]. Whilst these have shown a turnover point in nitrogen incorporation at lower temperatures, this is not observed in the work presented here.



There are several differences between this data and the corresponding results for the  $\text{InN}_x\text{Sb}_{1-x}$  layers. The cut off temperature for nitrogen incorporation is higher and the degree of nitrogen incorporation at a given temperature is greater. The nitrogen inclusion temperature, extrapolated from the graph, is  $405(5)^\circ\text{C}$ , which is significantly higher than that for the  $\text{InSb}$  analogue and the amount of nitrogen inclusion per degree is calculated as  $0.016(1)\%$  for every  $^\circ\text{C}$  reduction from the cut-off temperature. In the case of the  $\text{InN}_x\text{Sb}_{1-x}$  layers this rate is only  $0.013(1)\%$  per  $^\circ\text{C}$ .

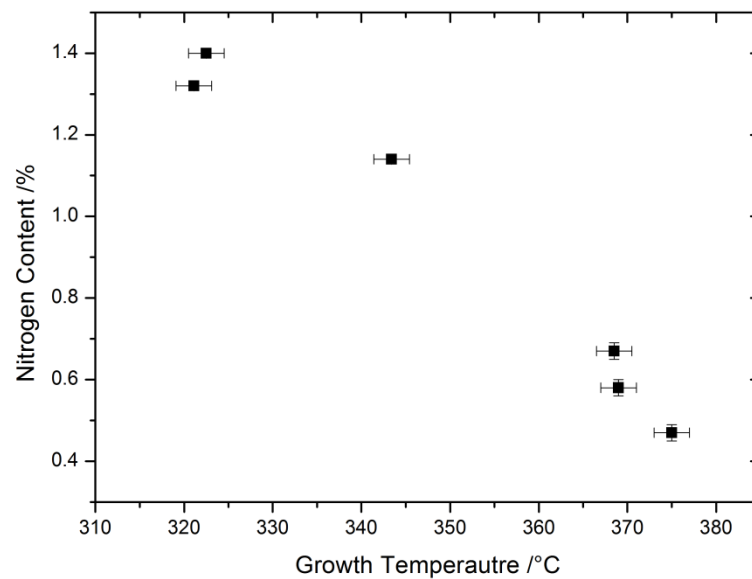


Figure 4.5 Nitrogen percentage incorporation of  $\text{GaN}_x\text{Sb}_{1-x}$  layer grown on GaSb at  $0.44 \mu\text{m h}^{-1}$  over various growth temperatures.

Examination of the layer peak FWHM from the RC scans show that in the case of the  $\text{GaN}_x\text{Sb}_{1-x}$  system there is no variation in the FWHM over the range of temperatures examined. This is different from the case in the  $\text{InSb}$  system where there are large variations in the FWHM (figure 4.4). This consistency in the  $\text{GaN}_x\text{Sb}_{1-x}$  system indicates that the strain within the  $\text{GaN}_x\text{Sb}_{1-x}$  layer is constant and that growth temperature does not affect the amount of in-built strain within the layer. Additionally, the amount of strain exhibited in the layers is not affected by the increased nitrogen incorporation; clearly the lattice mismatch between the layer and substrate in the GaSb system does not induce as much strain as the  $\text{InSb}$  system even though the lattice mismatch as a function of nitrogen content is consistent between the two materials ( $0.015\text{\AA}$  per N%). This indicates that the GaSb materials have a more resilient crystal structure than that of the  $\text{InSb}$ ; the Ga-Sb bonding is less susceptible to induced strain than the In-Sb bonds in that system.

#### 4.4.3 Relaxation of GaNSb Grown on GaSb

The use of a single rocking curve to determine the nitrogen content in these systems is dependent on the assumption that the layer is 100% strained. To determine if this assumption is valid, further investigation of the  $\text{GaN}_x\text{Sb}_{1-x}$  layers grown on a GaSb substrate were undertaken using reciprocal space mapping. Data were collected about the 004 and 224 diffraction peaks to determine not only the nitrogen incorporation into the sample, but also the relaxation of the lattice of the layer relative to the substrate. In a 100% strained layer, the in-plane lattice parameters of the layer are perfectly epitaxial with the substrate. The tetragonal distortion that is induced leads to a decrease in the out-of-plane lattice parameter and so can lead to discrepancies in the determination of the nitrogen content if the relaxation of the layer is not, as assumed, 100% strained. An example of the RSM's collected during this study is given in figure 4.6 and shows the positions of the relevant peak in both the symmetric and asymmetric reflection. The results of the analysis of these RSM are shown in table 4.2.

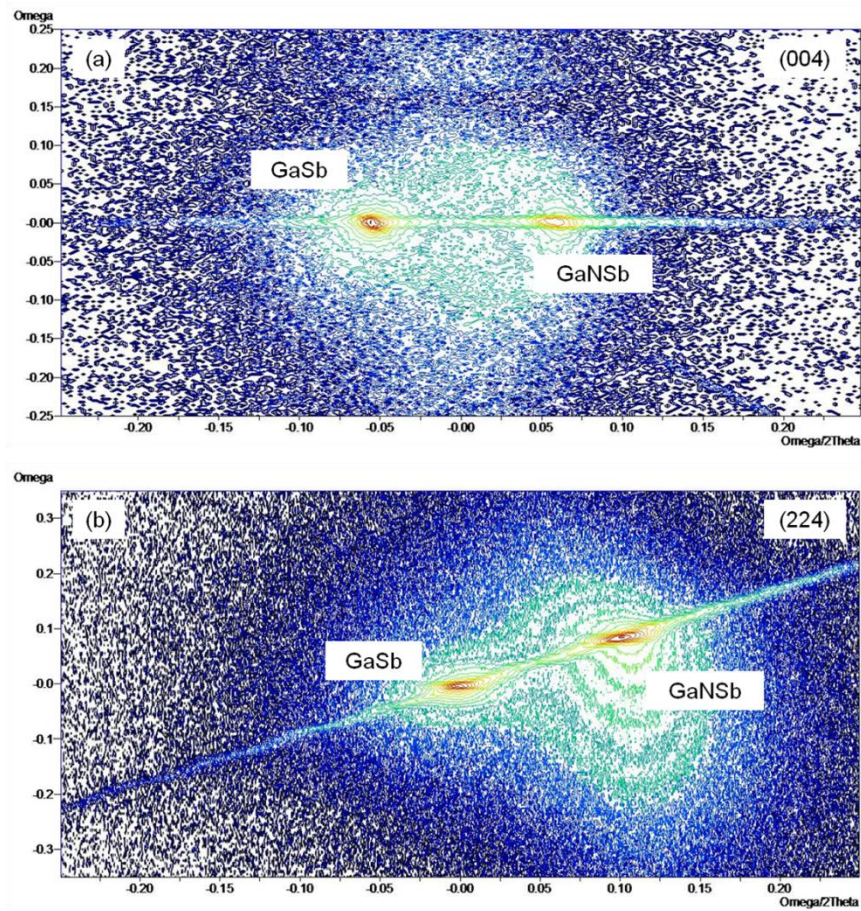


Figure 4.6 Example RSM around the symmetric 004 diffraction peak (a) and the asymmetric 224 peak (b) the data is shown in the physical axes over which it was collected,  $\omega$ - $2\theta$  and  $\omega$ .

Sample Growth Temperature	Nitrogen content (%) assuming R=0%	Lattice relaxation, R, /%	Nitrogen content (%) given relaxation R
321(2)	1.32(1)	0.4(1)	1.32(1)
323(2)	1.40(1)	-1.4(1)	1.45(1)
369(2)	0.58(2)	2.2(1)	0.48(2)
368(2)	0.67(2)	7.6(1)	0.71(2)
343(2)	1.14(1)	0.2(1)	1.13(1)
375(2)	0.47(2)	6.0(1)	0.44(2)

Table 4.2 Difference in nitrogen incorporation determined by RC assuming R=0%, and the RSM analysis giving lattice relaxation and nitrogen incorporation for various GaNSb layers grown at the given temperatures

The results in table 4.2 show that the assumption that the lattice is 100% strained is not valid. The values of the relaxation vary up to 7.6 % and, interestingly, one layer is unexpectedly over-relaxed implying that the in-plane lattice parameters of the layer are larger than both the bulk nitrogen-containing material and the substrate. Whilst this one result maybe an erroneous point, for the other results, having non-zero relaxation, leads to differences in the actual nitrogen incorporation of the layer. The differences in calculated nitrogen content are also given in table 4.2. As described above, increases in lattice relaxation would increase the out-of-plane lattice parameter, but this lattice parameter has not changed, therefore the only explanation is that more nitrogen is included in the lattice than would be expected if the layer was 100% strained. The increased lattice relaxation leads to decrease in the calculated nitrogen incorporation value, as seen in table 4.2. Whilst small deviations in the lattice relaxation result in very small changes in the nitrogen content, which are within the errors of the values calculated from rocking curves alone, this is exaggerated as the lattice relaxation is increased. For example, when the layer relaxation approaches 7.6%, the calculated amount of nitrogen incorporation has increased by 6% from that determined by RC analysis alone. This change is related to a change in the orientation of the samples which can be seen in the RSM results but not in the RC scans.

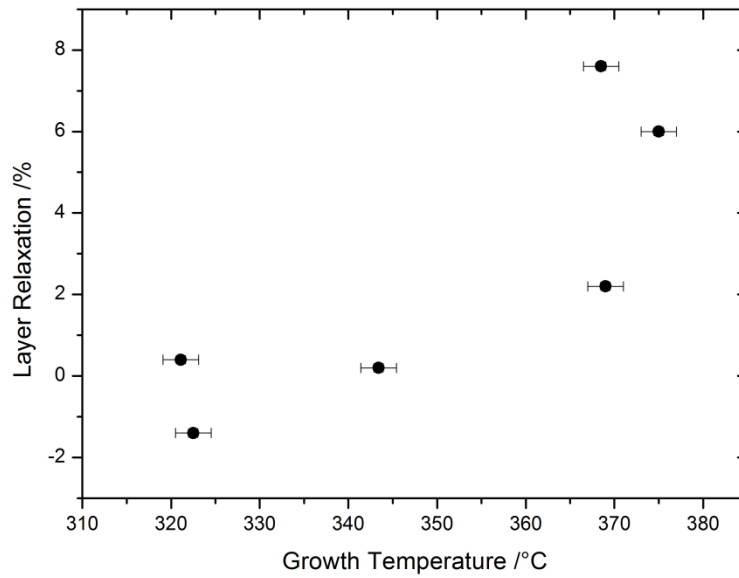


Figure 4.7 Lattice relaxation determined from RSM scans of  $\text{GaN}_x\text{Sb}_{1-x}$  layers grown at various temperatures

Figure 4.7 shows that there is a positive correlation between the relaxation of the lattice and the growth temperature of the sample. As the growth temperature is increased, the samples exhibit greater lattice relaxation. This may be because the ions in the layers grown at higher temperatures have more thermal mobility allowing for the layer to relax relative to the substrate. This is clearly not related to the degree of nitrogen incorporation, as samples grown at these elevated temperatures contain less nitrogen and, therefore, exhibit lower lattice mismatch between the substrate and layer.

The result of these analyses show that the assumption that the layer is 100 % strained is incorrect and leads to incorrect calculations of nitrogen content from the RC analysis. The difference in calculated nitrogen content is most prevalent at high temperatures where nitrogen incorporation is low and lattice relaxation is at its greatest. The deviation in these nitrogen results could also be seen at higher nitrogen incorporation levels (lower temperature) if the layers are consistently over-relaxed.

#### 4.4.4 Crystal quality of GaNSb Grown on GaSb

From the RSM scan around the 004 diffraction peak, the FWHMs of the layer peak in both scan directions,  $\omega$  and  $\omega$ -2 $\theta$  were determined, these values give information about how the layer has grown and the resultant crystalline quality of the layer. The  $\omega$ -2 $\theta$  FWHM is consistent with the FWHM determined from the RC scans, showing that the FWHMs of the

layers are very similar over the range of samples. As there is no trend in these results, this again indicates that the strain within the layers is constant over all the growth temperatures. This can be explained as the growth of the samples allows for mixing of the ions before they are deposited on the substrate. This mixing allows the nitrogen ions to be evenly distributed within the structure. Therefore the strain is reduced as the nitrogen inclusion is spread throughout structure and results in very little variation in the lattice parameter within the material. The strain seen in the layers is induced by the substrate and this strain is constant and independent of the nitrogen content; hence the lattice mismatch between the layer and substrate, which indicates that the GaSb structure can resist this mismatch better than the InSb material.

The  $\omega$  FWHM from the scans shows that there is a trend in the results which is shown against the nitrogen content and growth temperature of the GaNSb layer (figures 4.8 and 4.9). Figure 4.8 shows that as the nitrogen content of the layers increases, the  $\omega$  FWHM decreases. As this FWHM is an indication of the amount of mosaic spread within the layer, it shows that the layers with higher nitrogen content have fewer areas of mis-orientation and fewer grain boundaries. The formation of separate grains within the grown material is usually a way of reducing inbuilt strain within the layer; however, the layers with the greatest lattice mismatch are found here to have the lowest mosaicity. Conversely and unexpectedly, the samples with less nitrogen content exhibit signs of greater mosaic spread indicative of a greater spread in the orientations of the grains within the sample. These two results indicate that the resultant quality of the crystal is related to the growth conditions, rather than the resultant nitrogen content. This is further seen in figure 4.9, which shows that the mosaic spread of the samples is greatly increased at higher growth temperatures. The higher temperatures induce greater strain within the material during growth and then as the samples are cooled this strain is released in the form of lattice relaxation and increased mosaic spread. These effects are less evident in samples with higher nitrogen content as the samples are grown at lower temperatures. This may be the result of a difference in the thermal expansion between the layer and the substrate, which causes the difference between the lattice parameters of the layer and substrate to become larger as the sample cools, resulting in greater transient thermal strain that is then reduced by these mechanisms.

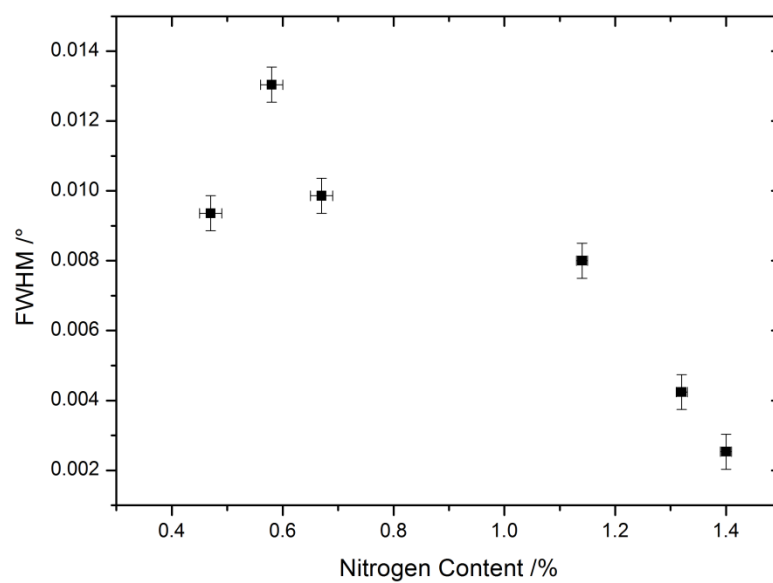


Figure 4.8  $\omega$  FWHM of 004 diffraction peak from GaNSb layer determined from RSM scans as a function of nitrogen content also determined from the RSM analysis

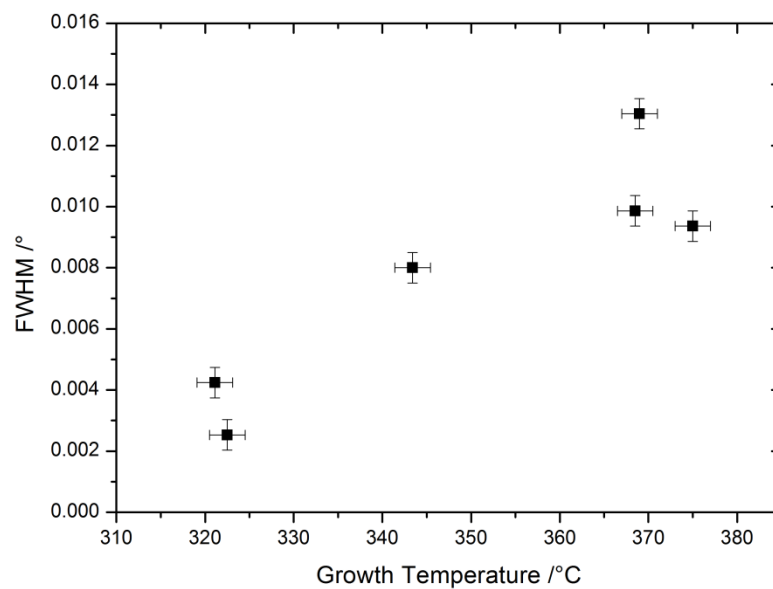


Figure 4.9  $\omega$  FWHM of 004 diffraction peak from GaNSb layer determined from RSM scans as a function of the growth temperature of the layer

## 4.5 Conclusions

Clearly, from this analysis it is possible to predict the amount of nitrogen inclusion for both InSb and GaSb materials for a given growth temperature and a given growth rate. Whilst both dilute nitride systems based on InSb and GaSb exhibit a linear relation between growth temperature and nitrogen incorporation there are some important differences between the  $\text{InN}_x\text{Sb}_{1-x}$  and  $\text{GaN}_x\text{Sb}_{1-x}$  layers. The upper cut-off temperatures for nitrogen incorporation in these two materials are different with the  $\text{GaN}_x\text{Sb}_{1-x}$  system able to include nitrogen at higher growth temperatures than that of the  $\text{InN}_x\text{Sb}_{1-x}$  system. The rate of nitrogen inclusion is also greater in the GaSb system than InSb, as the growth temperature is reduced more nitrogen can be incorporated into samples based on GaSb. The effect of growth rate on the layers, however, has similar effects; the amount of nitrogen inclusion is reduced as the growth rate is increased. The  $\text{InN}_x\text{Sb}_{1-x}$  layers are more susceptible to strain during growth than the samples based on  $\text{GaN}_x\text{Sb}_{1-x}$  which maybe as a result of reduced intermixing of the antimony and the nitrogen ions during growth.

Previous studies have assumed that the lattice of the layer is perfectly strained with the substrate; however this work has shown that this is not the case and that there are small variations in the lattice relaxation of the layer which changes the actual amount of the nitrogen incorporation identified compared to a simple RC analysis alone. Whilst these variations in determined nitrogen content are small at low concentrations of nitrogen, it becomes more pronounced at higher nitrogen levels if the strain within the layer lattice causes the layer to over relax. In this case the nitrogen incorporation is over estimated in the RC analysis. Therefore, relying on RC analysis alone to determine nitrogen content gives inaccurate results thereby not producing the expected changes in the bandgap of the material. These are important effects that have to be accounted for before any such semiconductor material can be tuned to a specific wavelength.

From the analysis of the quality of the grown materials by examination of the FWHM of the Bragg peaks it appears that materials with greater amounts of nitrogen inclusion have better crystalline quality. This may seem counter intuitive given the greater amount of lattice mismatch but the quality is primarily related to the growth temperature of the layer and not the nitrogen content. Therefore the samples with greater amounts of nitrogen are naturally better quality than those with less nitrogen. This is fortuitous as the greater bandgap reduction is seen at higher nitrogen content and the effects on the bandgap from poor crystal quality are reduced.

## 4.6 Further Work

In this study only a limited number of samples were examined in each of these systems. Further samples would need to be investigated to confirm some of the results seen in this work, particularly the effect growth temperatures has on the quality of the layers and how this quality can be improved. Additionally, there are areas where further samples would increase the scope of the conclusions reached, for example, samples grown at various growth rates would help further determine what effect the growth rate has on the degree of nitrogen incorporation. This is particularly true for the InSb based systems where few studies have examined lower growth rates. The effect of growth rate has been investigated in other work [6] but this only examined the effect of growth rate at two growth temperatures. This should be expanded to determine the effect of growth rate over a wide range of temperatures. Whilst the range of temperatures investigated are in the range which is determined to have the greatest effect on the bandgap of the material [3], it is also important to extend this range to lower temperature to see if nitrogen incorporation at these temperatures is possible and what effect these lower growth temperatures have on the quality of the grown samples. This would also allow for further investigations into the effect of growth temperature on the quality of the grown samples and whether it would be possible to grow samples at lower temperature with the same nitrogen content but even better crystal quality. These layers, grown at lower temperatures will also help determine whether samples at these temperatures do in fact over relax and what effect this has on the actual nitrogen content within the sample.



## References

- [1] B.G. Yacobi, Semiconductor Materials: An Introduction to Basic Principles. New York: Kluwer Academic Publishers (2003)
- [2] S. Adachi (ed.) Handbook on Physical Properties of Semiconductors, Volume 2: III-V Compound Semiconductors. New York: Kluwer Academic Publishers (2004)
- [3] L. Buckle, B. R. Bennett, S. Jollands, T. D. Veal, N. R. Wilson, B. N. Murdin, C. F. McConville, T. Ashley, J. of Crystal Growth **278** (2005) 188-192
- [4] I. Vurgaftman, J. R. Meyer, J. Appl. Phys. **94** (2003) 3675
- [5] D. Bagayoko, L. Franklin, G. L. Zhao, J. Applied Physics **96** (2004) 4297
- [6] M. J. Ashwin, T. D. Veal, J. J. Bomphrey, I. R. Dunn, D. Walker, P. A. Thomas, T. S. Jones, AIP Advances **1** (2011) 032159

## Chapter 5

# Annealing of GaNSb Samples Grown Hetroepitaxially on GaAs

### 5.1 Introduction

It is assumed that during the growth process, plasma assisted molecular beam epitaxy, that any nitrogen incorporated into the samples is located on the B site of the semiconductor material. This is desirable as it is the nitrogen on this site that is functional in reducing the optical bandgap of these materials. Whilst it has been shown that the amount of substitutional nitrogen, i.e. nitrogen on the crystallographic B site (hereafter SubN), incorporated into the structure is dependent on the growth temperature of the MBE process (chapter 4), what has not been shown is whether some of the nitrogen deposited during the growth process occupies interstitial sites within the structure of gallium antimonide. This interstitial nitrogen (hereafter IntN) plays no function in reducing the band gap of the material and only serves to reduce the quality of the as-grown crystal structure. This leads to unforeseen effects on the other properties of the material such as its thermal expansion properties, which could lead to a greater mismatch between the sample and the substrate and its susceptibility to physical degradation such as cracking during thermal shocks. As this IntN incorporation is not fully understood or controllable, it leads to inconsistencies in repeated growth runs, which can mean samples grown under the same conditions have differing concentrations of IntN, again affecting their physical properties. The aim of this work is to understand if any IntN is incorporated into the structure of these samples when they are grown and, more importantly, if this IntN can displace antimony and be incorporated onto the crystallographic B site through annealing. If so, this would lead to an increase in the SubN incorporation, thereby enhancing the desirable bandgap modification post-growth without having to resort to the growth of an entirely new sample. Within this study, the effect of annealing the as-grown samples at various temperatures is investigated to understand if this treatment will allow the IntN to mobilise and become SubN instead. Given that any changes in the SubN and IntN incorporation over time will reduce the efficiency of any devices based on these materials, how these materials would react to possible elevated operating temperatures is also investigated.

## 5.2 Sample Growth and Annealing

Samples of GaNSb were grown on an [001] orientated GaAs substrate. Use of this substrate gives heteroepitaxial growth and hopes to avoid the effects of relaxation from annealing. 2" (5cm) diameter wafers of three different samples were grown using plasma assisted MBE at QinetiQ using the equipment and method described in [1] under conditions that were designed to produce nitrogen contents of 1.5%, 1.0% and 0.5%. Each sample was grown to a nominal thickness of 2 $\mu$ m to ensure that the grown material would be completely relaxed. The range of nitrogen incorporation was chosen to give a good representation of the different nitrogen concentrations that have been grown and investigated previously. [1,2] Each of these 2" wafers was then cleaved into 8 sections and these were individually annealed. The annealing process involved heating the sample to the desired temperature and holding at this temperature for no more that 300 seconds before cooling again to room temperature. To avoid the out-diffusion of excess amounts of gallium and antimony, the samples were surrounded by powdered GaSb to maintain the equilibrium of ions in the sample and avoid the formation of vacancies in the crystal structure of the material. The samples were annealed under vacuum rather than air to avoid any possible introduction of nitrogen into the sample from the surroundings. The temperatures to which each of the constituent sub-samples were annealed are listed in table 5.1.

Sub-sample Number	High Nitrogen Content Sample (HNCS) Annealing temperatures /°C	Medium Nitrogen Content Sample (MNCS) Annealing temperatures /°C	Low Nitrogen Content Sample (LNCS) Annealing temperatures /°C
2	360(5)	380(5)	395(10)
3	410(5)	425(5)	435(10)
4	460(5)	475(5)	485(10)
5	460(5)	475(5)	485(10)
6	510(5)	525(5)	535(10)
7	560(5)	575(5)	585(10)
8	610(5)	625(5)	635(10)

Table 5.1 Annealing temperature for each of the three samples investigated. The temperatures of the sub-samples from each of the three samples are different due to the difference in growth temperature.

The first temperature at which each sample is annealed is its growth temperature, which accounts for why the starting temperatures in Table 5.1 are different for the high, medium and LNCs. Table 5.1 also shows that for each sample sub-samples 4 and 5 were treated to the same annealing conditions, albeit during separate annealing runs, in order to investigate if the results from these samples are consistent. This is only a small contribution to what would need to be a more comprehensive investigation into whether the results of annealing can be duplicated reliably to provide a controlled and predictable method for improving the nitrogen content and crystal quality of these materials.

## 5.3 Experimental Details

### 5.3.1 X-ray Diffraction

Several x-ray diffraction experiments were performed on each of the sub-samples listed in table 5.1. First, each sample was individually aligned in the diffractometer such that the sample surface was in the half-cut beam position and parallel with the beam. The sample was then aligned to the 004 reflection of GaAs by manipulating the 4-circles of the diffractometer until the reciprocal lattice vector of the reflection was aligned with the detector. At this point,  $2\theta$ - $\omega$  rocking curve scans were performed over an appropriate range to include the GaNSb(004) peak and the GaAs(004) substrate peak. In addition, Reciprocal space mapping (RSM) was performed around a symmetric peak, the 004 reflection again, and an asymmetric diffraction peak, in this case the 224 reflection. For these scans the sample was first aligned to the 224 reflection in  $\phi$ ,  $\psi$  and  $\omega$  to align the lattice vector and maximise intensity. Whilst maintaining the same  $\phi$  position, the 004 reflection was aligned, again to maximise the intensity of the GaAs substrate peak. The range of reciprocal space scanned in each of these RSM's was adequate to include both the substrate peak and the layer peak. The size was tailored using the assumption that the layer would be approximately 100% relaxed, which is particularly important for capturing the full extent of the asymmetric reflection RSM. For the symmetric RSM scans the resolution of the  $\omega$ - $2\theta$  direction is set to  $0.002^\circ$ , over a range of  $3.6^\circ$ , with a count time per step of 0.15 seconds. This scan is then repeated after the value of  $\omega$  is changed by  $0.01^\circ$  over a range of  $\omega$  of  $1.01^\circ$  resulting in 102  $\omega$ - $2\theta$  scans producing the RSM. The asymmetric RSM was collected using an  $\omega$ - $2\theta$  range of  $4.5^\circ$  with the same resolution as above, with a count time per step of 0.2 seconds. 114 of these individual  $\omega$ - $2\theta$  scan produce this RSM with an  $\omega$  step size of 0.01 resulting in an  $\omega$  range of  $1.13^\circ$ .

### 5.3.2 Secondary Ion Mass Spectroscopy (SIMS)

SIMS measurements were performed on a selection of the sub-samples to determine the absolute nitrogen content of the associated layers for comparison with the nitrogen content calculated from the x-ray analysis. A sample of GaNSb grown on GaSb with known nitrogen content was used as the reference for all subsequent measurements. The primary ion beam used in these experiments was oxygen ( $O_2^+$ ) with energy of 4keV at an incident angle of  $60^\circ$ . Using a quadrupole mass analyser to select an appropriate mass-to-charge ratio, both ON and  $NO_2$  ions were investigated to determine the nitrogen content as a function of depth. In addition to this, the other atoms from the sample were investigated to determine the depth profile of antimony, arsenic and gallium within the sample. This was achieved by examining the detection rates of ionised  $Sb_2O_3$ ,  $As_2O_3$  and both GaO and  $Ga_2O$ , respectively.

## 5.4 Experimental Results

### 5.4.1 X-ray Analysis of Nitrogen Content

As a first step, the out-of-plane lattice parameters were investigated. With only up to 2% nitrogen incorporation expected in the GaNSb layers, there is expected to be a large mismatch between the layer and substrate as the cubic lattice parameters of the substrate (GaAs) and GaSb are  $5.653\text{\AA}$  and  $6.096\text{\AA}$  respectively.[3] The initial assumption is that because of the thickness of the layer and the large lattice mismatch, the layer is 100% relaxed on the substrate. Under this assumption, only the out of plane, symmetric, reflection is required to determine the lattice parameter and, therefore, the nitrogen content of the layer. An example of this type of scan (figure 5.1) confirms the large mismatch between the layer and the substrate. The absolute position of the layer peak is not used to calculate the lattice parameter of the layer. Rather, the substrate position is calculated from the published lattice parameter [3] and the separation between this peak and the layer peak is used to calculate the position of the layer peak and therefore the difference in d-spacing between the layer and substrate. This difference in d-spacing is then used to calculate the lattice parameter of the nitrogen containing layer. This method helps to eliminate any systematic errors from variations in the peak positions related to the initial configuration of the diffractometer and the alignment of the sample.

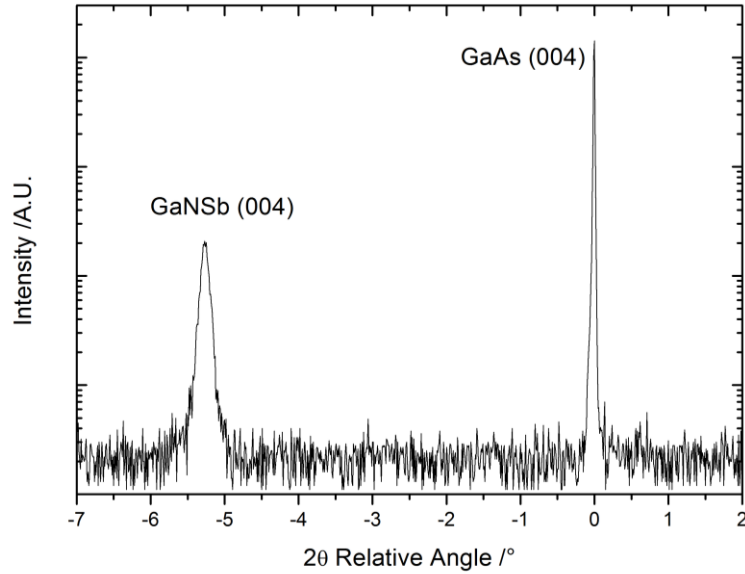


Figure 5.1.  $2\theta$ - $\omega$  scan of the 004 reflection of the MNCS annealed at 735°C. The scale shows the large mismatch between GaAs and GaNSb, c.a. 5° in  $2\theta$ . This separation is used to calculate the lattice parameter of the GaNSb sample.

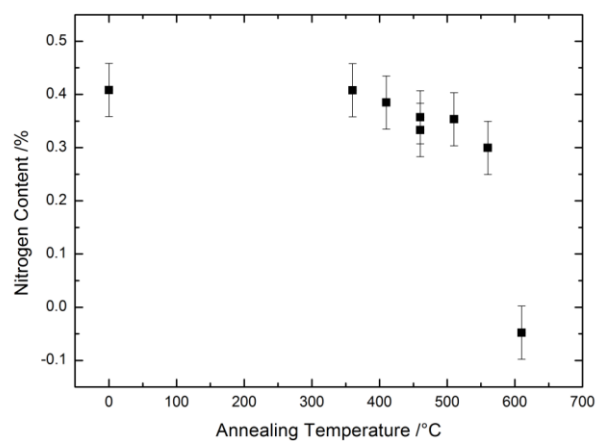
Using this calculated lattice parameter and assuming the layer is 100% relaxed then Vegard's Law is used to calculate the appropriate nitrogen content of the layer, using a cubic-GaN lattice parameter of 4.50Å. [4] As the nitrogen content of these layers is expected to be only up to 2 %, and the change in lattice parameter therefore small, a linear approximation of Vegard's Law is used to estimate the nitrogen incorporation. The results of the calculations are given for each of the annealed group of sub-samples in figure 5.2.

Figure 5.2 shows that there is very little change in the nitrogen content for each of the samples as they are annealed up temperatures approaching 600°C. However, the final annealing of each sample shows a significant drop in the relative amount of nitrogen. This indicated that at temperatures above the penultimate annealing temperature of 560°C, 575°C and 585°C, for the high, medium and LNCSSs, respectively, there is an observable increase in the mobility of the nitrogen, which therefore allows the ions to diffuse out of the structure. It is possible that these ions are substituted by antimony ions that diffuse into the layer from the surrounding GaSb powder. This diffusion and substitution of ions potentially has an effect on the crystal quality of the layer and this is indicated in the shape of the 004 peak (section 5.4.2). These results indicate that there is a maximum annealing temperature above which any possible increase in the nitrogen content from interstitial sites and improvement in crystal quality is outweighed by the increased diffusion of nitrogen out of the sample.

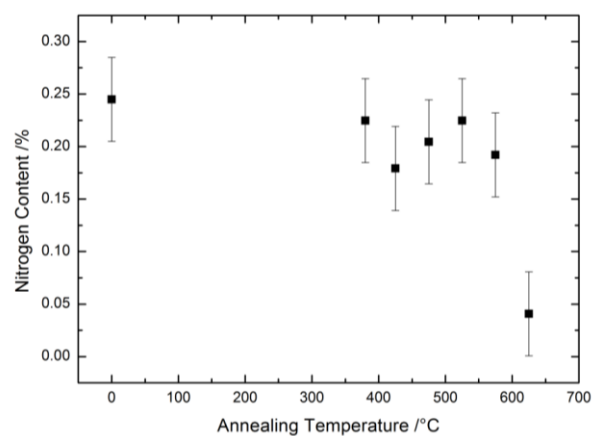
Figure 5.2 also shows that the two sub-samples from each sample that have undergone the same annealing at the same temperature are sufficiently similar to suggest that different parts of the same sample respond consistently when annealed at the same temperature.

Examining the amount of nitrogen present in the as-grown samples (sub-samples 1), it is clear that the nitrogen concentrations present do not correspond to the expected values based on the temperature at which they were grown and the previously published results. [1] In addition to this, all of the nitrogen incorporation values for the LNCS are negative values (Figure 5.2(c)). This implies that the separation between the layer and the substrate is greater than that which would be seen if the layer were simply pure GaSb. Since this is not possible, we conclude that the assumption of 100% relaxation is incorrect and the sample must be at least partially strained on the substrate. Whilst this means that the absolute nitrogen content calculated in figure 5.2 is inaccurate, the general trends of the behaviour are likely to be valid if we assume that the relaxation of all the annealed samples is broadly similar.

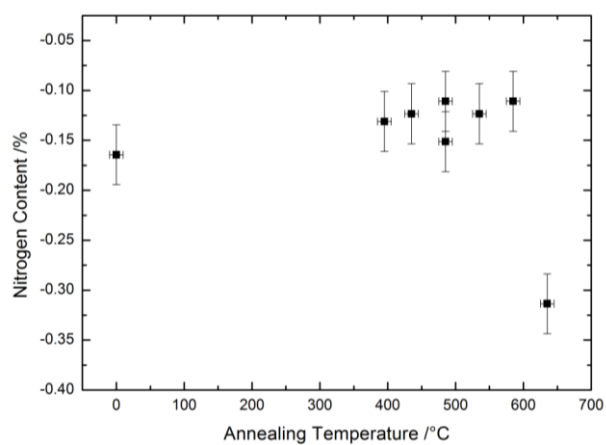
Detailed examination of Figure 5.2(a) shows a drop in the nitrogen content at lower annealing temperatures. This is also seen, albeit to a lesser degree, in the medium content sample, Figure 5.2(b), which implies that this out-diffusion of nitrogen is more pronounced in samples that start with more SubN within the structure of the sample. Therefore, the increased amount of SubN in the starting structure of GaNSb apparently increases the subsequent rate of out-diffusion. This argument suggests that there is an upper limit to the amount of nitrogen that a sample can retain when it is annealed; this could indicate that compositions that are designed with higher concentrations of nitrogen to access shorter wavelengths in the solar spectrum cannot be annealed, even at relatively low temperatures, without losing nitrogen from the structure and therefore adversely affecting the bandgap.



(a)



(b)



(c)

Figure 5.2. The calculated nitrogen content of (a) the HNCS, (b) the MNCS and (c) the LNCS after various annealing temperatures.



To investigate the amount of relaxation in the samples, analysis of the RSM's was undertaken using PANalytical X'pert Epitaxy software. The software uses the separation between the substrate and layer peaks from both the symmetric and asymmetric reflections together with the lattice parameters of the layer composition end-members and the substrate lattice parameter as reference. An example of these types of  $\omega$ - $2\theta$  vs.  $\omega$  scan is given in figure 5.3 which shows the positions of the various peaks in both the symmetric and asymmetric scan. The elasticity of the layer material is also taken into account as it is important to know how the layer deforms under the biaxial strain induced by the substrate.

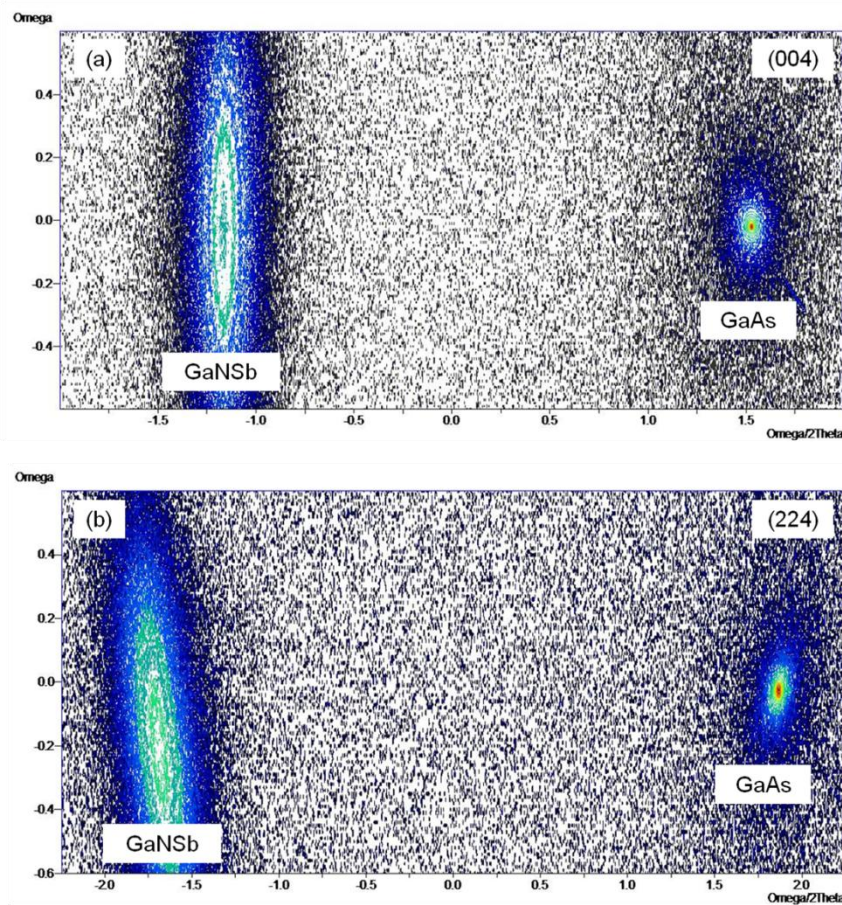
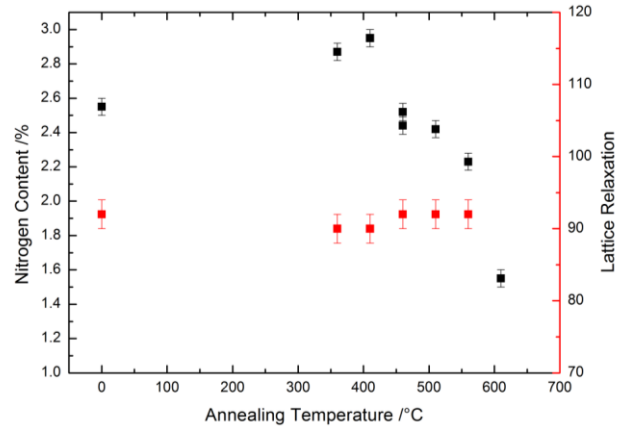


Figure 5.3 Example symmetric (a) RSM scan of around the 004 diffraction peak of GaAs and (b) the asymmetric RSM, showing the relative positions of the GaNSb layer peak and the GaAs substrate peak.

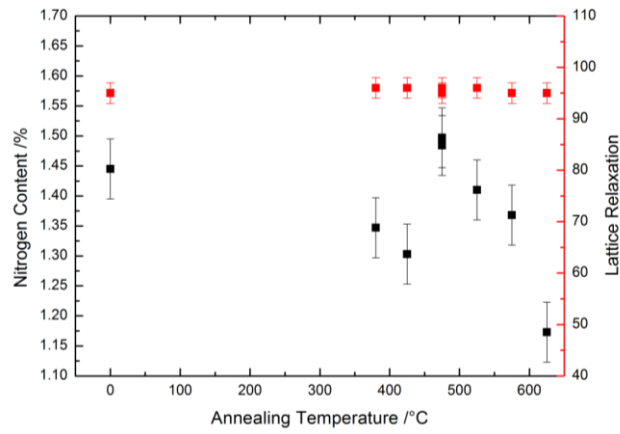
The calculated Poisson's ratio for the bulk materials GaSb [5] and cubic GaN [6] are incorporated in X'pert Epitaxy. However, the elasticity of the layer varies depending on the amount of SubN, which is one of the unknown quantities we are seeking to determine. The position of the asymmetric peak will move towards the 224 vector in reciprocal space if the sample is more relaxed until at 100% relaxed the layer peak is superimposed on the 224

vector. By contrast, the effect of nitrogen incorporation reduces the separation between the substrate and the layer peaks along the 224 vector. Both of these effects are used to determine the relaxation and nitrogen content of the layer given the method described in section 2.2.5.1. Additionally, the 004 RSM helps to inform the determination as the separation of the layer and substrate peak is a combination of the effects of relaxation, which in this case reduces the separation between the peaks, and the reduction in separation induced by the nitrogen. The substrate peak positions were assumed to correspond to the calculated position given by the reference lattice parameter- similar to the analysis used to produce Figure 5.2. The results of these analyses of the RSMs are shown in figure 5.4.

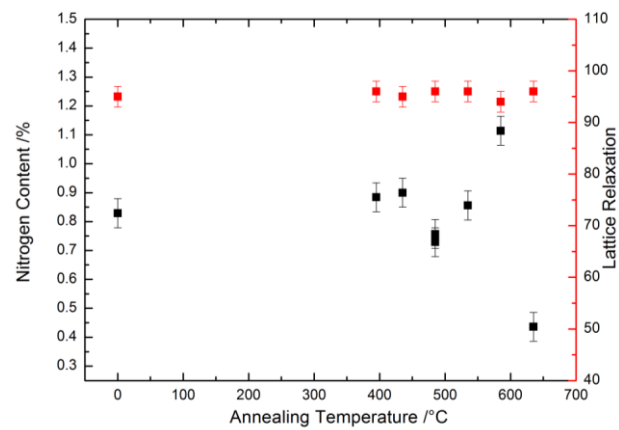
Examining figure 5.4 there are several items of interest. Firstly, the calculated as-grown nitrogen content of each sample is significantly higher than the content initially calculated using only Vegard's law. The nitrogen contents shown in this figure are much closer to the expected nitrogen content of each of the samples based on their growth temperatures, with the exception of the HNCS which has nominally 2.5(5)% nitrogen content (the expected nitrogen content was 2%). As seen in the initial analysis (Figure 5.2) there is evidence that the highest annealing temperatures do lead to a noticeable reduction of the nitrogen content by 90%. Similarly, this reduction is evident at lower annealing temperatures in the samples with higher as-grown nitrogen incorporation. Figure 5.4(a) shows a more noticeable reduction in nitrogen incorporation than in the MNCS, again implying that the increased amount of initial SubN in the structures helps allow the nitrogen to diffuse out of the structure at a lower annealing temperature. The exception to this is seen in the LNCS where there appears to be a maximum in the nitrogen content towards the higher annealing temperatures. This broadly agrees with the initial analysis that shows a slight increase of nitrogen content at higher annealing temperatures. This increase in nitrogen content as a result of annealing implies that there must initially be IntN incorporated into the sample during growth. All the samples exhibit some increase in the SubN inclusion upon annealing indicating that the incorporation of IntN into the samples when grown is a general phenomenon.



(a)



(b)



(c)

Figure 5.4. The nitrogen content (black) and the lattice relaxation (red) of (a) the HNCS, (b) the MNCS and (c) the LNCS after various annealing temperatures calculated using X'pert Epitaxy software which takes into account the relaxation and elasticity of the sample when determining the nitrogen content.

The results suggest that one improvement to the growth technique would be to reduce IntN incorporation by further controls over the nitrogen plasma flow during MBE. For this to be possible, additional understanding of the expected SubN incorporation into the sample for given growth conditions is required to balance the flow of nitrogen to ensure that no surplus nitrogen remains to be incorporated onto interstitial sites. From Figure 5.4 the annealing temperature required to maximise the SubN incorporation into the sample increases as the initial amount of SubN in the sample is reduced. For example the nitrogen content of the sample with c.a. 2.5% nitrogen peaks at an annealing temperature of only 410°C whilst the medium and low concentration samples peak at annealing temperatures of 475°C and 585°C, respectively. This mimics the trend of the temperature variation of the out-diffusion phenomenon discussed earlier; it can therefore be suggested that the structure of GaSb with more SubN initially incorporated, subsequently allows for easier atomic diffusion under annealing, in this case *into* the crystal structural sites from the interstitial sites. Re-stated, this means samples grown with higher initial nitrogen content can be annealed at lower temperatures to maximise the SubN content. This is useful as it is known that there is increased out-diffusion from such samples as they are annealed at successively higher temperatures. Balancing these two effects, an optimum annealing temperature can in principle be found, as a function of as-grown nitrogen content, where the nitrogen content can be maximised without being so high that the nitrogen will start diffusing out of the sample. Once annealed at this optimum temperature, the sample will contain the most SubN and reduced IntN further improving the physical properties of the sample. The annealing of the sample in this way reduces the number of ionic vacancies in the sample as the nitrogen and antimony diffuse in to occupy these positions. Fewer defects in the layer reduces the deleterious effect on the bandgap of on any semiconductor device which they are used in. [7]

The initial analysis of the samples did not show any increase in the nitrogen over the range of annealing temperatures, at least for the high and medium content samples, which adds further credibility to the supposition that the samples are not fully relaxed and, therefore, that strain must be taken into account during the analysis. Figure 5.4 gives the values of the lattice relaxation determined by the RSM analyses. The relaxation of all of the samples is calculated to be 95(4)%. Whilst the relaxation is broadly consistent across all of the annealing temperatures, there are some subtle variations that have a striking effect on the calculated nitrogen content. This is particularly true when comparing the trend of the results for the MNCS (Figure 5.4). The initial analysis, using just Vegard's law, does not

show any of the variation in nitrogen content seen in the more sophisticated RSM analysis thereby demonstrating that this sort of simple analysis is inadequate. Given the only slight, 95(4)%, variation of lattice relaxation between the annealing temperatures, it is expected that the trend in the nitrogen content between analysis techniques would be similar. However, it is very important that the relaxation of these layers is accurately determined as slight variations in the relaxation can have a striking effect on the calculated nitrogen content as these two parameters are coupled to the elasticity of the layer material, which in itself is a function of the nitrogen content, (section 2.2.5.1). The values of lattice relaxation have to be accurately determined in order to determine the nitrogen incorporated into the sample with confidence down to an accuracy of 0.01% nitrogen.

The relaxation between the as grown sub-sample and the sub-samples which have been annealed at high temperature shows very little variation indicating that the initial relaxation of the layer when grown is not changed by the annealing process. The small amount of strain in the samples could not be removed by annealing at temperatures up to c.a. 600°C.

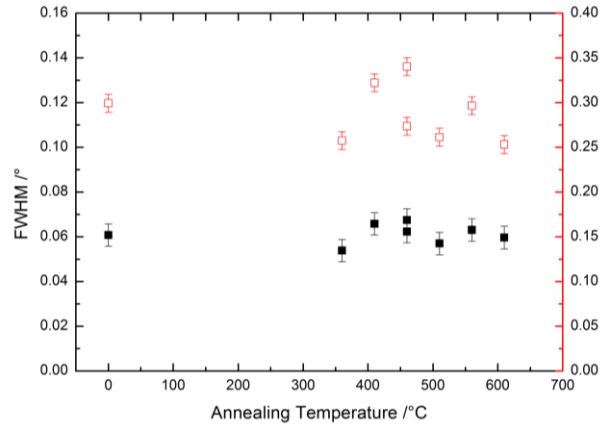
Reassuringly the results for both sub-samples that were treated to the same annealing process are consistent. Both the nitrogen content and the lattice relaxation results for both samples agree too, within experimental error. This is true for all three sample sets indicating that the behaviour of the samples from annealing is consistent regardless of the underlying nitrogen content.

#### 5.4.2 Crystal Quality determined by X-ray Analysis

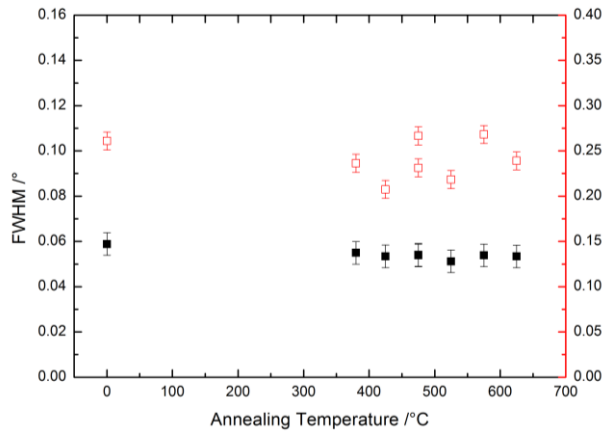
From the analysis described above it is clear that the annealing of the various samples has changed the structures of the materials at the atomic level. The trend is for the SubN content initially to increase, and then noticeably decrease as the annealing temperatures of the sub-samples are increased. Whilst these changes in nitrogen content have been investigated, it has been assumed that any subsequent crystallographic vacancies have been filled by antimony ions, because of the chemical environment in which the samples were annealed. These changes in the chemical composition of the samples result from the ease of diffusion within the structure and this will ultimately affect the quality of the material. This phenomenon is examined here by measuring the width of the 004 peak from the GaNSb layer as extracted from the 004 RSM to yield the FWHMs in both the  $\omega$ -2 $\theta$  and  $\omega$  directions. The  $\omega$ -2 $\theta$  FWHM is used to determine an estimate of the range of lattice d-spacings resulting from effects such as the inhomogeneous distribution of nitrogen

throughout the structure and any residual strain in the layer, which has not been removed by lattice dislocations at the interface, caused by the layer-substrate lattice mismatch. The  $\omega$  FWHM is used to assess the degree of mosaic spread in the layer, which arises from slight changes in the orientation of the crystal growth. Annealing the samples may remove some of this spread, or may result in more spread from the propagation of grain boundaries caused by microscopic changes in different areas of the layer arising from changes in nitrogen content, both interstitial and substitutional. The results of this analysis are given for each sample and associated sub-samples in figure 5.5 which shows the results as a function of annealing temperature.

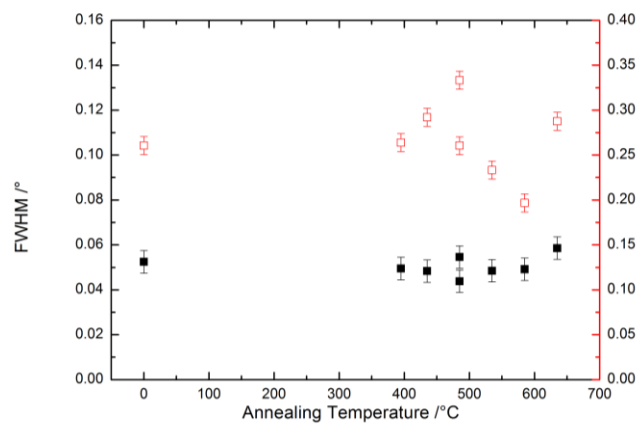
From figure 5.5 it is apparent that there is no significant change in the  $\omega$ -2 $\theta$  FWHM of the 004 layer peak between the as grown sub-sample and any of the annealed samples. There is also very little change in the  $\omega$ -2 $\theta$  FWHM values over the range of annealing temperatures. These observations suggest (1) there is little, if any, change in the strain brought about by annealing; (2) there is little, if any, dependence of the strain on the annealing temperature. Both (1) and (2) indicate that the variation in lattice spacing is consistent regardless of the annealing process implying that the distribution of nitrogen within the sample is broadly homogeneous even in the as-grown samples and that the annealing does not change this distribution significantly. If there were any inhomogeneity inbuilt into the as-grown sample, it would be reasonable to expect that the annealing of the sample would allow for the redistribution of the nitrogen, given that the analysis in section 5.4.1 has proved that nitrogen ions are able to diffuse. If this were the case there should be a corresponding reduction in  $\omega$ -2 $\theta$  FWHM at the annealing temperatures where the nitrogen diffusion is maximised, i.e. where the nitrogen incorporation percentage is at its maximum, but this is not observed.



(a)



(b)



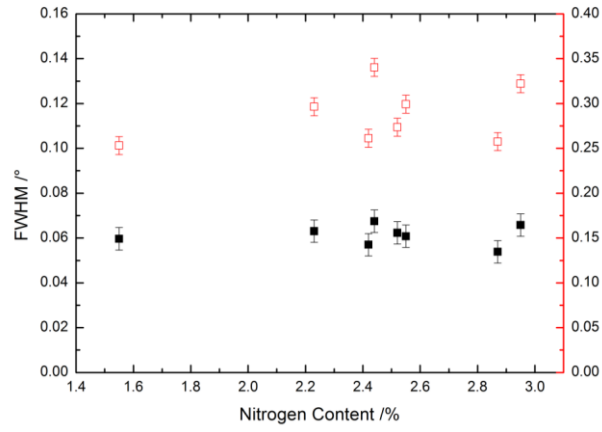
(c)

Figure 5.5. The  $\omega-2\theta$  FWHM (black) and the  $\omega$  FWHM (red) of (a) the HNCS, (b) the MNCS and (c) the LNCS as a function of the annealing temperature of each sub-sample.

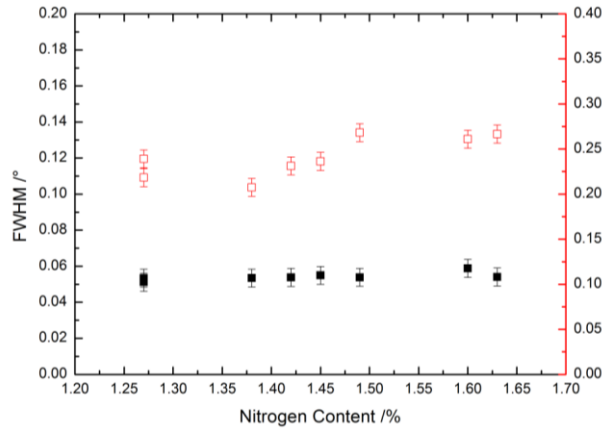
The  $\omega$ -2 $\theta$  FWHM results are not only similar across the range of the annealing temperatures but they are also very similar across the range of samples from the high nitrogen content (0.060(10)°) to the low (0.052(10)°). This slight change can be attributed to the increased amount of substitutional nitrogen incorporation, as the higher nitrogen content will increase the strain within the layer. Clearly the homogeneity of nitrogen incorporation is unaffected by the amount of SubN initially incorporated into the sample and therefore the growth temperature of the sample. This can be rationalised given the method of growth, MBE, which allows for a large degree of intermixing of the ions before they are deposited on the substrate.

As expected, the  $\omega$  FWHM of the 004 GaNSb reflection is greater than in the  $\omega$ -2 $\theta$  direction as it is easier for the layer to become mis-orientated during growth and the subsequent relaxation of the layer by increasing mosaic spread. These effects can be exacerbated as the thickness of the layer increases and more strain energy is stored in the layer. There are greater fluctuations in the  $\omega$  FWHM than in  $\omega$ -2 $\theta$  FWHM. These fluctuations in the  $\omega$  FWHM, 0.10° in the HNCS, 0.08° for the MNCS and 0.16° for the LNCS, show no correlation with the initial nitrogen content in each sample. There appears to be no correlation in these  $\omega$  FWHM values with some of the annealed values being greater than the as grown sub-sample and some being smaller. It is possible these fluctuations arise from discrepancies in the initial alignment of the samples: for example, a small misalignment of the tilt angle of the sample results in larger-than-minimum  $\omega$  FWHM. There is also a discontinuity in the  $\omega$  FWHM values for the two sub-samples that were annealed under the same conditions. Given that until now all analyses have shown these two sub-samples being consistent, these inconsistencies together with the lack of correlation suggest that other undetermined and uncontrolled conditions, possibly associated with the annealing or maybe not, are affecting the orientation mismatch. Clearly it is not just the annealing temperature which is effecting the orientation and likewise the diffusion of ions within the sub-samples during annealing is not having a systematic or reproducible effect on the orientation.

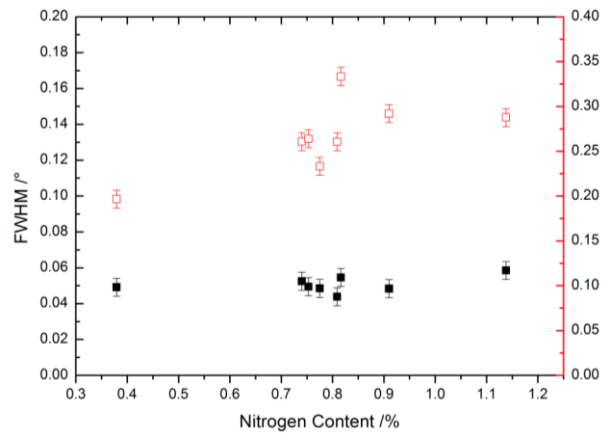




(a)



(b)



(c)

Figure 5.6. The  $\omega$ -2 $\theta$  FWHM(black) and the  $\omega$  FWHM(red) of (a) the HNCS, (b) the MNCS and (c) the LNCS as a function of the nitrogen content as calculated by X'pert Epitaxy.

As the increased SubN has been incorporated from interstitial sites (section 5.4.1) and the orientation of the layer maybe affected by the inclusion of ions in interstitial sites it is important to examine the effect of nitrogen content on the  $\omega$  FWHM. The changes in nitrogen content have an effect on not only the diffusion rates within the sample but also the availability of interstitial sites. These sites could be populated either by residual nitrogen or displaced/diffused antimony ions. The results of the comparison between nitrogen content, as determined by the second analysis given in section 5.4.1, and the  $\omega$  FWHMs of the 004 GaNSb peak are given in Figure 5.6.

As expected, the values of  $\omega$ -2 $\theta$  FWHM are invariant as a function of nitrogen content. This reinforces the conclusion from above that there is a homogeneous distribution of nitrogen atoms within the lattice structure of the sample, thus validating the use of Vegard's law when determining the nitrogen content of the sample in the analysis given in section 5.4.1. This homogeneous distribution is invariant across the range of nitrogen concentrations, from c.a. 2.5%, seen in the HNCS and c.a. 0.4%, seen in the LNCS, as well as being invariant regardless of the annealing temperatures to which the samples are exposed.

Figure 5.6 shows that there is a trend for the  $\omega$  FWHM to increase as the nitrogen content of the sample increases. This trend is seen across all three samples and this positive correlation between the nitrogen content and the range of orientations can be attributed to (a) additional nitrogen allowing the lattice to be more easily distorted and (b) with less IntN present there are more interstitial site available to be potentially occupied by antimony ions. These antimony ions are either displaced by nitrogen substitution or ions diffused into the structure from outside sample. With the larger atomic radius of the antimony ions [8] the distortions of the lattice are more pronounced producing mis-orientations. The thickness of the sample then exaggerates this effect as there are more interstitial sites which can be filled and the sites closer to the top surface of the sample are less effected by the influence of the substrate and more so by the already mis-orientated layer below.

### 5.4.3 SIMS Analysis of Nitrogen Content

From the analysis performed in sections 5.4.1 and 5.4.2 it is clear that within the samples the effect of annealing has changed the composition of the samples by allowing for diffusion of nitrogen both within the sample and out of the sample as well as diffusion of antimony ions, which have been displaced by the nitrogen, both out of the sample and into interstitial sites within the sample. SIMS has been utilised to determine the absolute

amount of nitrogen within each sample and to see how this nitrogen content changes as a result of the annealing process and how these absolute values compare with the results calculated in section 5.4.1. The nature of SIMS analysis allows for the secondary ion yield to be profiled as a function of depth, given a constant erosion rate, to establish any diffusion between the layer and the substrate of the sample. Diffusion, if any, into the GaAs layer will help verify the ease with which both nitrogen and antimony can diffuse out of the layer.

The SIMS results of the nitrogen content through the depth of a selection of the sub-samples from the LNCS are shown in figure 5.7(c). The sample, which should have only a nominal nitrogen content of 0.85%, consistently has a total nitrogen content above this value at c.a. 1.5%. The sub-sample annealed at the highest temperature has increased nitrogen content above the levels seen by the x-ray analysis, which indicates that annealing at this temperature should have removed nitrogen from the layer. Whilst it may be possible that this increase in nitrogen level has resulted from additional inclusions of nitrogen on to interstitial sites, which would not be seen in the x-ray analysis, it is unclear where this additional nitrogen could have originated. One possibility is contamination of the furnace during the annealing process. There is also a large amount of nitrogen diffusion into the substrate, which would be consistent with nitrogen contamination at high temperature during annealing.

Figure 5.7(a) shows the SIMS analysis for a selection of sub-samples from the HNCS. The as-grown sample appears to contain up to double the amount of nitrogen that is present in any of the other sub-samples. The other sub-samples show consistent nitrogen content of c.a. 1.75% which is below the nitrogen content results from the x-ray analysis of between 2.95% and 1.55%. This is most likely due to a slight error in the absolute nitrogen content of the reference sample, which is further exacerbated by the relatively small amount of nitrogen present in the samples and the difficulty in ionising it with the primary ion beam. More importantly, the relative concentrations compared between the sub-samples are of interest. The as-grown nitrogen content is much higher than the other sub-samples in this high nitrogen content sample. Due to the lower growth temperature associated with this sample, larger amounts of IntN could have been incorporated into the structure during growth. This higher rate of IntN inclusion is not seen in samples grown at higher temperatures. Therefore, the lower growth temperature allows more nitrogen incorporation not only onto substitutional sites but also into interstitial sites. The growth of

HNCSs therefore requires, counter intuitively, a reduced nitrogen flow rate as the nitrogen can be more easily incorporated into substitutional sites at these lower temperatures. The excess of IntN in the as-grown sample have been reduced by the annealing process to a level of total nitrogen which is constant throughout the other sub-samples. The clear interface between the layer and the substrate indicates that this excess nitrogen has not diffused into the substrate layer below and must have diffused out of the sample completely. The consistency of the nitrogen content within the other sub-samples implies that the increase and then decrease of SubN within the layer as a result of the annealing is from the conversion of IntN into SubN and then back again and therefore no nitrogen is diffused out of the sample as a whole. This is also seen in the lack of nitrogen diffusion into the substrate, clearly after an initial annealing which removes any excess IntN the level of total nitrogen reaches an equilibrium which then remains constant. The effect of different annealing temperatures is to change the ratio of substitutional to IntN; referring back to the x-ray analysis there is an optimal temperature which maximises this ratio and therefore the amount of SubN. For the high, medium and LNCSs these annealing temperatures are 410(25)°C, 475(25)°C and 585(25)°C respectively. Annealing above these temperatures results in the diffusion of nitrogen away from substitutional sites back into interstitial sites.

The SIMS profile for the MNCS, figure 5.7(b), does not show any evidence for the inclusion of additional IntN in the as-grown sub-sample, most likely because the growth temperature of this sample was higher than the HNCS. All of the sub-samples shown in this figure have a nominal total nitrogen content of 1.25%, close to the nominal nitrogen amount seen in figure 5.7(a), thus indicating that the optimum amount of nitrogen inclusion into the sample is not dependent on the growth temperature and that the growth temperature only effects the initial ratio of substitutional to IntN which can then only be marginally changed by annealing at an appropriate temperature. There is a much less obvious interface between the layer and the substrate which signifies that there is more nitrogen diffusion into the substrate than in the previous sample. This diffusion is evident in the as-grown sample and as such the additional diffusion seen in this sample is a result of the growth of the sample and not the annealing - further evidence that there is very little diffusion of the nitrogen out of the layer of the sample, indeed some of the profiles from the annealed sub-samples show a more distinct interface resulting from nitrogen diffusing back into the layer.

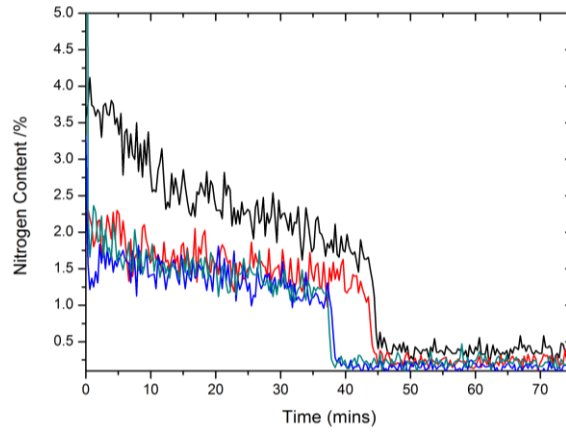


Figure 5.7(a) The SIMS profile of nitrogen content of sub-sample 1(Black), 3(Red), 5(Blue) and 8(Green) of the HNCS, given as a function of the time the sample is exposed to the primary beam.

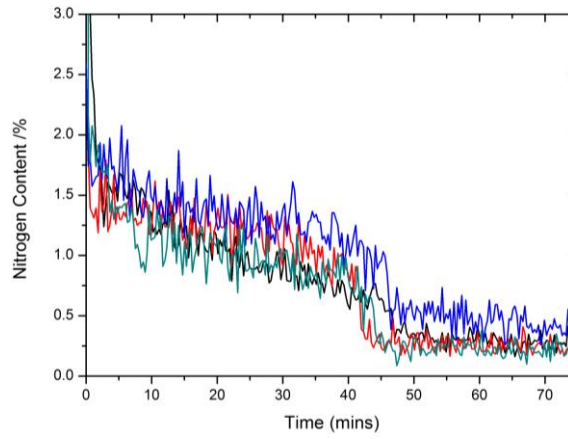


Figure 5.7(b) The SIMS profile of nitrogen content of sub-sample 1(Black), 4(Red), 5(Blue) and 8(Green) of the MNCS, given as a function of the time the sample is exposed to the primary beam.

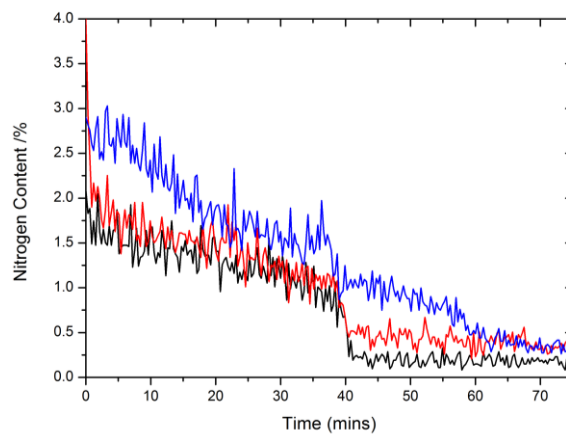


Figure 5.7(c) The SIMS profile of nitrogen content of sub-sample 1(Black), 7(Red) and 8(Blue) of the LNCS, given as a function of the time the sample is exposed to the primary beam.

The characteristics of the SIMS profiles for the LNCS, figure 5.7(c), are very similar to those of the medium content sample, there is a similar level of total nitrogen within the sample and this doesn't change between the as-grown sample and the annealed sub-samples. There is a similar profile of the diffusion of nitrogen into the substrate of the sample but again this amount of diffusion is seen in the as-grown sample and doesn't change much as a result of annealing except for the possible contamination discussed above.

By examining the antimony ion yield from the SIMS analysis it is possible to understand the effect annealing has had on the interface between the grown layers and the substrate. The results also give an idea of the mobility of the antimony and the possibility of how these ions may affect the quality of the sample. The assumptions described above with regard to the distortions of the lattice being a result of antimony effectively swapping with nitrogen within the sample from substitutional sites to interstitial sites and how this change results in the increases seen in the  $\omega$ FWHM, figure 5.6.

Figure 5.8 shows well defined interfaces between the antimony containing layer and the substrate, which indicates very little diffusion of the antimony ions into the substrate. The diffusion that is seen in the samples is less pronounced in the HNCS whereas more antimony diffusion is seen in the LNCS. In the case of the annealing of the high-content samples there is a reduction in the amount of antimony diffused into the substrate, indicating that the annealing process have helped improve the interface between the two parts of the sample. This is also true of the medium-content sample in which annealing has improved the interface, with the exception of the sub-sample with the maximum amount of SubN in it, where the diffusion of antimony into the substrate is most pronounced. The same is seen in the high-content sample where the sub-sample with the maximum SubN in it has a relatively high amount of antimony diffusion into the substrate. However the reverse is true in the low-content sample where more diffusion is seen as a result of annealing, most likely as a result of the poorly defined interface created during the growth of the sample. Figure 5.8 shows there is the possibility of antimony easily diffusing around the sample, the increased amount of antimony diffusion within sub-samples with maximum SubN would indicate that there is more interstitial antimony inclusion in these samples and therefore adding to the distortion of the lattice and, therefore, the resulting shape of the 004 peak in the x-ray data.

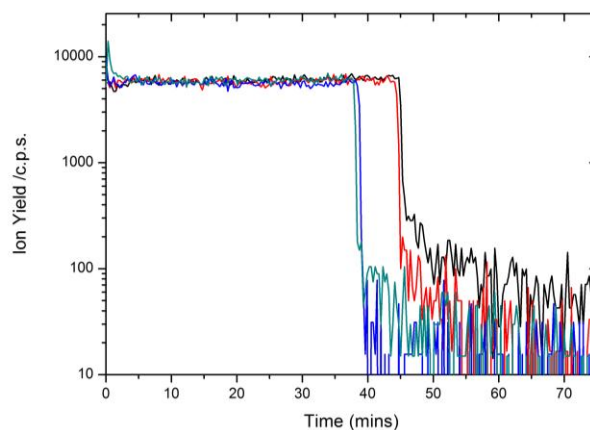


Figure 5.8(a) SIMS profile of antimony ion yield from sub-sample 1(Black), 3(Red), 5(Blue) and 8(Green) of the HNCS, given as a function of the time the sample is exposed to the primary beam.

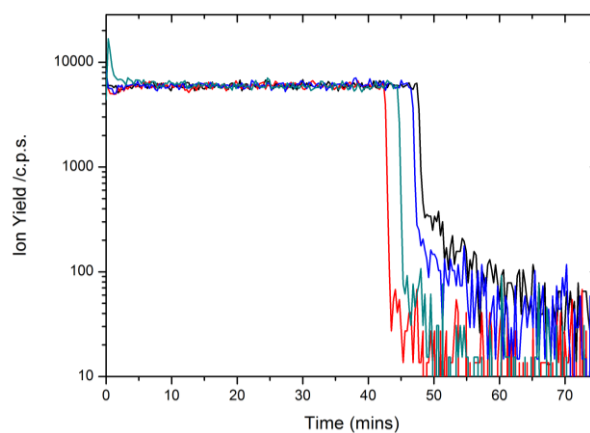


Figure 5.8(b) SIMS profile of antimony ion yield from sub-sample 1(Black), 4(Red), 5(Blue) and 8(Green) of the MNCS, given as a function of the time the sample is exposed to the primary beam.

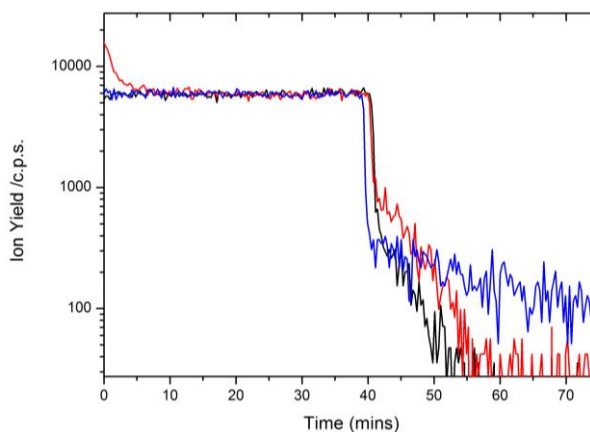


Figure 5.8(c) SIMS profile of antimony ion yield from sub-sample 1(Black), 7(Red) and 8(Blue) of the LNCS, given as a function of the time the sample is exposed to the primary beam.

## 5.5 Conclusions

From the results discussed in this chapter a clear picture of the nature of these types of samples has been developed and what effect the annealing of these samples has on the amount of SubN. From the co-analysis of both SIMS and x-ray results, it is clear that the total amount of nitrogen within all the samples, regardless of the growth temperature or annealing temperature, is constant and the only differences that the growth temperature has on the composition of the sample is to (a) force the inclusion of additional IntN into the sample at low growth temperatures and (b) to change the initial ratio of nitrogen in substitutional and interstitial sites. This ratio, in (b), can then be subsequently affected by annealing. The annealing temperature which will maximise this ratio in favour of SubN is dependent on the initial ratio when the layer was grown and therefore on the growth temperature of the sample. The higher the growth temperature, the higher the annealing temperature required. However, above this annealing temperature the ratio will then further change in favour of reducing the amount of SubN. The rate of this change is dependent on the amount of SubN already within the structure - the higher the amount of nitrogen on substitutional sites the more mobile the nitrogen is and the more rapidly it returns to an interstitial site. This movement of the nitrogen within the sample is complemented by the antimony, which seems to trade with the nitrogen ions resulting in more interstitial antimony in the structure when the amount of SubN is high; this leads to greater distortions of the lattice due to the interstitial antimony, as the SubN increases.

## 5.6 Further Work

There is one area in this work which needs further clarification - where these IntN site are situated within the sample. Quantitative analysis of the IntN content will help verify that the total concentration of nitrogen within the samples is indeed constant and that there is a corresponding, mirrored, change in the amount of IntN to that seen in the substitutional analysis provided by the x-ray analysis. One method for achieving this would be to examine the local vibrational modes (LVM) within the layer. LVM analysis is a variation on other forms of vibrational spectroscopy and in this type of sample would utilise FTIR in the long wavelength infrared range. LVM would show how the IntN is coupled with the other atoms in the material or whether there is diatomic nitrogen in the interstitial sites of the layer. In addition to this examining a wider range of samples will help to variety the identified trends and confirm that these effects are seen over the entire range of nitrogen inclusion that is possible into these types of structures. Re-annealing the sub-samples which show a



reduction in SubN content to try and improve the ratio of substitutional to IntN would help show any reversibility that could be utilised for when these materials start to degrade over continual use. The work shown here could be further extended by annealing the samples at higher temperatures in order to find a point at which the nitrogen within the layer is no longer constant and does in fact start diffusing out of the sample into the surrounding environment and thus cannot be reincorporated into the substitutional site by re-annealing, this could help determine the upper operating limit of any device which would utilise these materials.

## References

- [1] L. Buckle, B. R. Bennett, S. Jollands, T. D. Veal, N. R. Wilson, B. N. Murdin, C. F. McConville, T. Ashley, J. of Crystal Growth **278** (2005) 188-192
- [2] M. J. Ashwin, T. D. Veal, J. J. Bomphrey, I. R. Dunn, D. Walker, P. A. Thomas, T. S. Jones, AIP Advances **1** (2011) 032159
- [3] B.G. Yacobi, Semiconductor Materials: An Introduction to Basic Principles. New York: Kluwer Academic Publishers (2003)
- [4] I. Vurgaftman, J. R. Meyer, J. Appl. Phys. **94** (2003) 3675
- [5] G. Gökoglu, J. of Alloys & Compounds **478** (2009) 653-656
- [6] M. E. Sherwin, T. J. Drummond, J. Appl. Phys. **69** (1991) 8423-8425
- [7] F. Tuomisto, J. -M. Mäki, C. Rauch, I. Makkonen, J. Cryst. Growth **350** (2012) 93-97
- [8] J. C. Slater, J. Chemical Phys. **41** (1964) 3199

## Chapter 6

# Sodium Lithium Borohydride

### 6.1 Introduction

Low molecular weight borohydride materials have been considered as possible hydrogen storage materials for various reasons including their abundance, relative ease of synthesis and their cost. However, whilst these borohydrides constructed with low molecular weight ions such as lithium, calcium, sodium and aluminium, have good hydrogen storage weight percentages, their low atomic numbers allow for strong ionic bonding, which is difficult to overcome to liberate hydrogen.

Once such candidate material is sodium borohydride ( $\text{NaBH}_4$ ), which has a relatively high hydrogen weight percent (10.66%) and is a viable candidate as a hydrogen storage material. However, the aforementioned strong ionic bonding means that its hydrogen desorption temperature (550°C [1]) is too high for use as an onboard storage material according to the targets set by the DOE (table 1.2).  $\text{NaBH}_4$  crystallizes in the well-known sodium chloride structure, a face centred cubic structure ( $Fm\bar{3}m$ ,  $a = 6.131(1)\text{\AA}$ ) with sodium ions on the unit cell vertices and face centres and borohydride ions ( $\text{BH}_4$ )<sup>-</sup> placed on the cell edges equidistant from the sodium ions and at the unit cell centre. (figure 6.1(b)) This tightly-packed unit cell reinforces the bonding between the ions. Another possible hydride material is the lithium analogue, Lithium Borohydride,  $\text{LiBH}_4$ . Despite its chemical similarity to the sodium compound,  $\text{LiBH}_4$  has a significantly different crystal structure.  $\text{LiBH}_4$  crystallizes in a highly orthorhombic structure ( $Pmna$ ) with large lattice parameter ratios of  $a/b = 1.618$  and a  $b/c = 0.6522$ . By examining the structure of  $\text{LiBH}_4$ , it is clear that lower symmetry leads to varying interatomic distances between the lithium ions and the borohydride ion, ranging between 2.48 to 2.54 Å, as opposed to the constant contact distance in  $\text{NaBH}_4$  of 3.06 Å. In addition to this, the tetrahedral coordination of hydrogen around the central boron atom is distorted leading to varying H-B distances ranging from 1.04 Å – 1.29 Å. A graphical comparison between the structures of these two borohydrides is given in figure 6.1. The purpose of our study is to combine these two different structure types – in a manner similar to the solid-solution approach adopted in other areas of Functional Materials - to enhance particular physical properties. Through this combination,

we aim to improve the hydrogen desorption properties of  $\text{NaBH}_4$  by destabilising the structure with lithium inclusions, thereby not only reducing the hydrogen desorption temperature of the resulting material relative to pure  $\text{NaBH}_4$ , but also increasing the hydrogen weight percentage contained in the sample. The mixed (Li,Na) borohydride samples are then to be examined by a number of techniques including PXRD both at ambient and high temperature, solid-state NMR and differential thermal analysis. The PXRD experiments were performed on samples both made *in situ* i.e. formed from the mixtures of the constituent materials sealed in a capillary and heated during x-ray powder diffraction analysis, and *ex situ* i.e. by heating and annealing the constituent starting materials in the furnace in the inert atmosphere of the glove box, to form the required compound. The solid-state NMR and DTA experiments were performed only on *ex situ* samples. In each case, the phase formation conditions for the *ex situ* synthesis were established *via* the *in situ* P-XRD experiments.

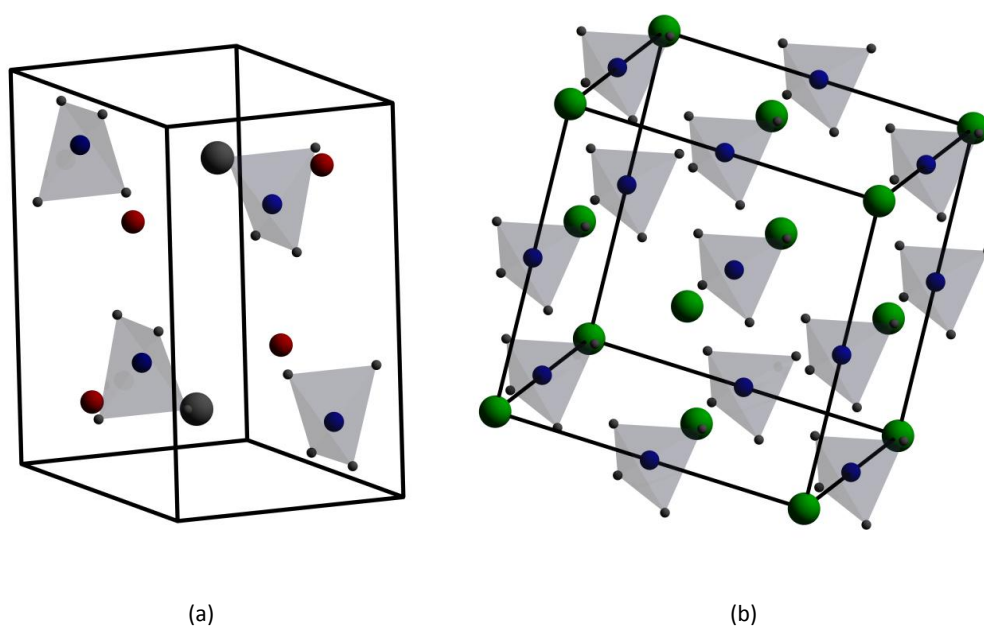


Figure 6.1 The crystal structures of (a)  $\text{LiBH}_4$ , showing the positions of the lithium atoms (red) with the unit cell and at varying distances to the borohydride tetrahedra. (b)  $\text{NaBH}_4$  cubic structure, showing sodium atoms (green) on the face centres and vertices with the tetrahedra equidistant. (Boron:blue, Hydrogen:grey)

## 6.2 Experimental Details

In order to investigate the initial reaction between these two materials,  $\text{NaBH}_4$  and  $\text{LiBH}_4$ , they were mixed together in equal molecular ratios sealed in a capillary under an inert atmosphere and investigated using *in situ* HT-XRD. For the *in situ* synthesis the samples

were heated at a rate of 10°C per minute and allowed to stabilise at the desired temperature for 15 minutes before x-ray scans were collected over an angular  $2\theta$  range of 10-70°, with each scan taking 2 hours to collect. The rate at which the sample was cooled was also 10°C per minute and again at each temperature the sample was allowed to stabilise for 15 minutes. The initial *in situ* synthesis data were collected up to temperatures of 220°C and then at various temperatures as the resultant sample was cooled. *In situ* synthesis of samples with a specific molar ratio were examined up to temperatures of 260°C using the same heating, cooling and dwell times as for the initial synthesis. For these samples if the room temperature scan after heating did not show a phase pure NaBH<sub>4</sub> structure, the sample was reheated whilst still *in situ* to various temperatures, (table 6.1) at the rates shown above, where the sample was allowed to dwell for up to an hour before being cooled again to room temperature, when phase purity was checked again using x-ray diffraction.

Three different compositions, hereafter Li-0.1, Li-0.2, and Li-03, (Table 6.1) were chosen for the *ex situ* synthesis. Whilst other compositions of mixed lithium sodium borohydride were initially investigated using *in-situ* HT-XRD, only samples up to 43% lithium (sample Li-0.3) could be synthesised phase pure. Other compositions showed some inter-mixing of ions but never to the degree shown in these 3 samples, where a signal phase could be formed. As a result, only these three samples were investigated further to identify any effect that the presence of lithium may have.

In the *ex situ* synthesis, the starting materials, LiBH<sub>4</sub> and NaBH<sub>4</sub>, were thoroughly mixed together at the appropriate molar ratio before been added to a glass container and inserted into the glove box furnace. The samples were heated, held at temperature and cooled corresponding to the details given in table 6.1. The samples were all heated to these temperatures at a rate that corresponds to the ramping taking 5 hours from room temperature. Similarly, the samples were cooled in 4 hours. Whilst the temperatures of the synthesis and subsequent annealing were derived from the *in situ* analysis the dwell times were extended to account for the larger mass of the *ex situ* samples relative to the small amount of powder examined *in situ*.

After each annealing of the sample, it was removed from the furnace, ground up, and a small sample was then analysed using P-XRD to determine if it was phase-pure. If not, the remainder of the sample was re-annealed; this process was repeated until the PXRD

showed that phase-purity had been achieved. The temperatures and the repeated annealing runs required for each of the *ex situ* samples are summarised in table 6.1.

Sample	$\text{Li}_{0.1}\text{Na}_{0.9}\text{BH}_4$ (Li-0.1)	$\text{Li}_{0.2}\text{Na}_{0.8}\text{BH}_4$ (Li-0.2)	$\text{Li}_{0.3}\text{Na}_{0.7}\text{BH}_4$ (Li-0.3)
Initial <i>ex situ</i> synthesis parameters	260°C for 8 hours	280°C for 18 hours	330°C for 8 hours
1 <sup>st</sup> Annealing parameters	280°C for 8 hours	280°C for 18 hours	300°C for 10 hours
2 <sup>nd</sup> annealing parameters		300°C for 10 hours	

Table 6.1 The annealing parameters for each of the three compositions synthesized *ex situ*, The temperatures of each annealing are given as well as the length of time the samples were held at this temperature.

In preparation for the HT-PXRD experiments each of the samples was sealed in a 1mm-diameter glass capillary whilst in the inert atmosphere of the glove box. The HT-PXRD experiments were performed using a similar method discussed elsewhere in this work. (Chapter 3, section 3.2.1). For NMR experiments, the samples were loaded into 4mm diameter NMR rotors and sealed with the rotor cap within the glove box. The rotors were spun at 10 kHz to reduce broadening of the peaks. To help avoid any degradation of the sample during the NMR experiment, the rotors were spun in nitrogen gas instead of air to try to reduce the exposure of the sample to both oxygen and moisture. The NMR experiments on lithium-7 were performed in a magnetic field of 11.7 T –more commonly referred to as a 500MHz spectrometer given the Larmor frequency of protons at this field strength. The NMR spectra of the sodium-23 and boron-11 nuclei were performed on a 400 MHz spectrometer. For the DTA experiment, each of the samples was sealed, again in the glove box, in aluminium pans, as described in Chapter 3. The experiment was performed from room temperature up to 600°C and then cooled to room temperature, all at a rate of 10°C per minute.

## 6.3 Experimental Results

### 6.3.1 Initial Synthesis

The results of this initial heating and cooling experiment on the sample synthesized *in situ* with equal molar weights of  $\text{NaBH}_4$  and  $\text{LiBH}_4$  are shown in figure 6.2, which presents the cubic lattice parameter derived from fitting of the PXRD data as a function of temperature.

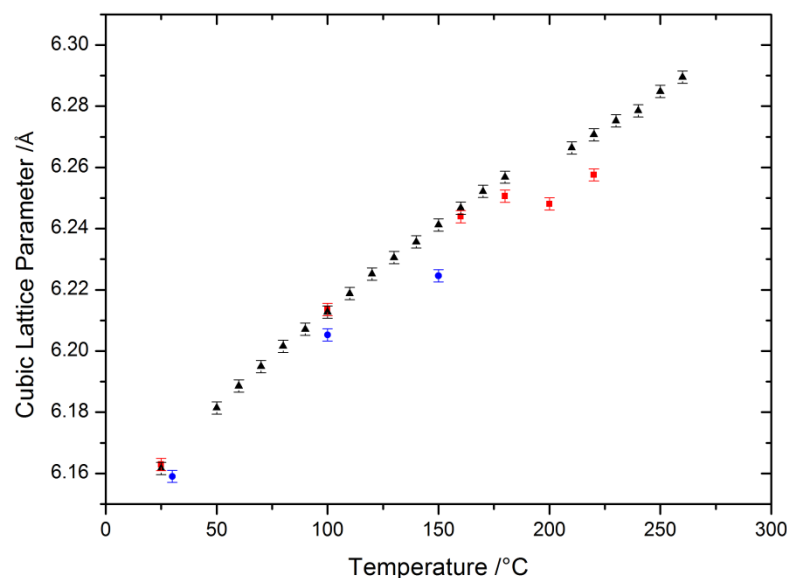


Figure 6.2 Cubic lattice parameters of the sodium borohydride phase of the initial, equal molar weight, sample during heating (red) and cooling (blue). For comparison the lattice parameters of sodium borohydride during heating of a pure sodium borohydride is shown (black).

On initial heating of the mixture, there is a well defined contraction of the lattice parameter of the  $\text{NaBH}_4$  phase as it is heated at around 200°C (red points, Figure 6.2). At temperatures above 200°C, it appears the material continues to expand. By contrast, the lattice parameter does not show the same discontinuity on cooling (blue points, Figure 6.2) indicating that this phenomenon is not reversible. Additionally, the lattice parameter of the resultant material during cooling is consistently smaller than the initial lattice parameters of  $\text{NaBH}_4$ . For comparison, the lattice parameters for pure  $\text{NaBH}_4$  are included in this figure (black points, Figure 6.2). From this two things are apparent:- (1) the lattice parameters of the  $\text{NaBH}_4$  component of this mixture during heating are the same as for the pure sample; (2) there is no corresponding contraction of the pure sample at 200°C, which indicates that this must be related to the proximity of  $\text{LiBH}_4$  in the mixed sample. Most likely this contraction in the volume of the  $\text{NaBH}_4$  unit cell is due to a reaction between  $\text{NaBH}_4$  and

LiBH<sub>4</sub>. A closer look at figure 6.2 shows that the deviation in the lattice parameter begins at a temperature 160°C, before the rate of deviation then rapidly increases at 200°C. Clearly, this temperature of 200°C is important when considering any reaction between the two borohydrides.

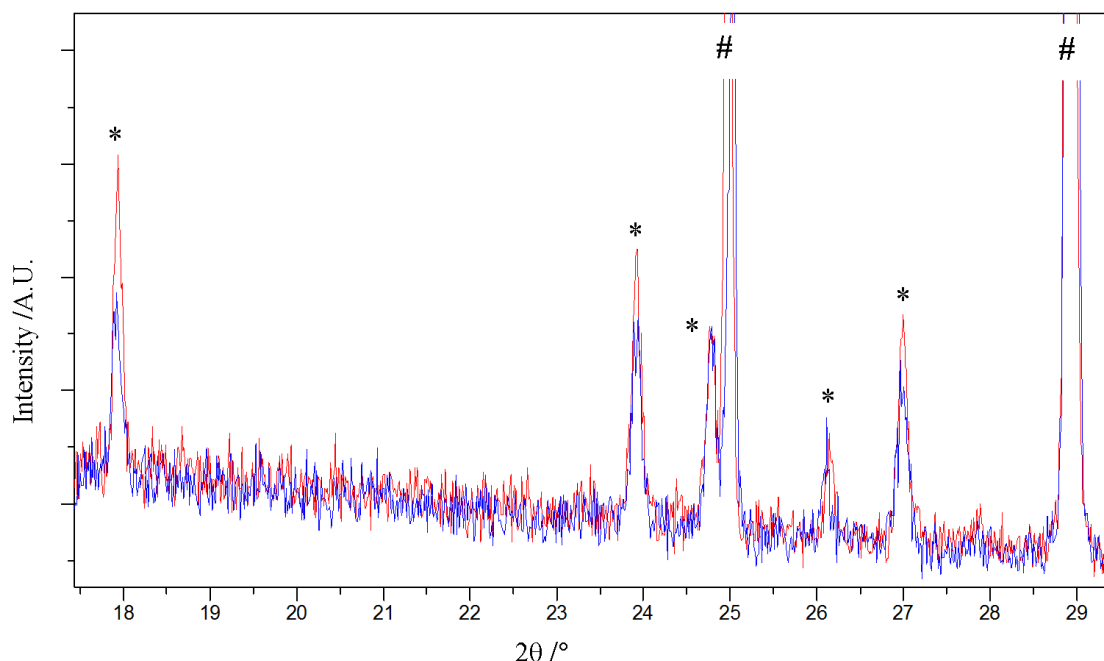


Figure 6.3 x-ray diffraction scans from before (red) and after (blue) the initial synthesis of the equal molar ration sample, showing the diffraction peaks from LiBH<sub>4</sub> (\*) and NaBH<sub>4</sub> (#).

From the room-temperature x-ray diffraction of the resultant material after the mixture in figure 6.2 is cooled, there are no additional crystallographic phases observed other than those of the two original materials. The presence of the LiBH<sub>4</sub> phase indicates that the reaction between the Li and Na compounds is not complete and that only a small proportion of the LiBH<sub>4</sub> has been incorporated into the NaBH<sub>4</sub> structure. Whilst it is difficult to quantify this diffusion using Rietveld refinement, because of the very low atomic weight of LiBH<sub>4</sub>, the comparison between the scans before and after heating (figure 6.3) show that there is less pure LiBH<sub>4</sub> after this reaction than before. There is no evidence for any other crystalline phases and no anomalous features in the background of the scan, further reinforcing the hypothesis that lithium has been incorporated into the sodium borohydride structure. The atomic radii of the two ions in question [Li]<sup>+</sup> and [Na]<sup>+</sup> are 1.45Å and 1.80Å respectively. [2] This difference in radii allows for the limited substitution of these two ions in the cubic structure of NaBH<sub>4</sub> at temperature, whereas the small size of Li<sup>+</sup> promotes its ability to diffuse through the close-packed structure. Similar effects have been seen in previous studies of ion substitution into NaBH<sub>4</sub>. [3] However given the small size of the



lithium ion, it is possible that these ions are diffusing into the structure and occupying interstitial instead of substitutional sites. X-ray diffraction cannot provide evidence on which type of site the lithium is situated. However, Nuclear Magnetic Resonance (NMR) should be able to offer insight into where the lithium is situated. (Section 6.3.5)

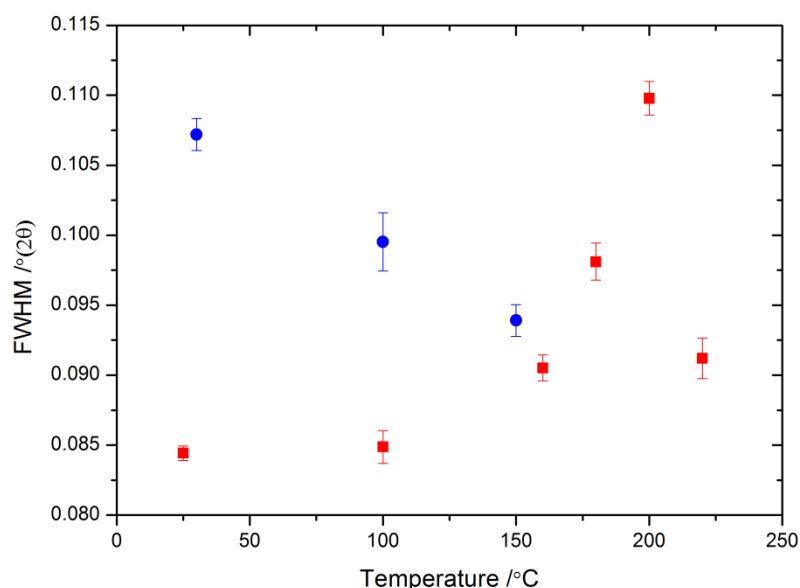


Figure 6.4 the FWHM of the {002} diffraction peak of the sodium borohydride phase of the initial sample during heating (red) and cooling (blue).

From the comparison of the full width at half maximum (FWHM) of the 002  $\text{NaBH}_4$  phase peak (figure 6.4), there is further proof that there is some sort of intermixing of these ions in the cubic structure. During heating, there is very little change ( $0.002^\circ$  in  $2\theta$ ) in the value of the FWHM of  $\text{NaBH}_4$  up to  $100^\circ\text{C}$  from which point, the FWHM begins to rise from  $0.085^\circ$  to  $0.110^\circ$ , a change of 30%, indicating a change in degree of perfection of the crystal structure of  $\text{NaBH}_4$  – this could be the result of either disorder or strain. This change corresponds to the temperature at which the contraction of the lattice volume occurs (seen in figure 6.2). After this point, the FWHM at higher temperature reduces again to a lower value ( $0.092^\circ$ ) albeit still higher than the before the reaction at  $200^\circ\text{C}$ , indicating that the amount of disorder/strain in the material has reduced due to the completion of the initial reaction between  $\text{NaBH}_4$  and  $\text{LiBH}_4$ . Furthermore, in figure 6.4, the cooling of this newly-formed material below  $150^\circ\text{C}$  results in an increase in the FWHM. It is difficult to ascertain the reason for this behaviour but we can discount the possible explanation that this is a reversal of the reaction that forms this mixed phase, because this would be seen in the lattice parameter of the material during cooling and it is not (figure 6.2). The increase in the

FWHM during cooling may be the result of the difference in the relative size of the ionic radii of sodium and lithium. At temperatures around 200°C this difference may be at its minimum, thereby allowing for the maximum inter-diffusion before the size of their coordination environments then diverge during cooling and lock the ions into the structure. There is also another possibility; the cooling of the mixed  $\text{LiNaBH}_4$  sample may result in a crystallographic phase change towards a lower symmetry space group. Given that the room temperature symmetry of  $\text{LiBH}_4$  is orthorhombic, it is possible that the broadening of the 002 diffraction peak FWHM is a result of the peak splitting into a triplet as a result of the divergence of the 200, 020 and 002 diffraction peaks resulting from a divergence of the a, b and c lattice parameters. As these peaks cannot be individually resolved, any changes in the lattice parameters must be very slight. This will be further investigated by examining the *ex situ* samples in section 6.3.4.

The results presented thus far clearly indicate that there is a reaction between the  $\text{LiBH}_4$  and  $\text{NaBH}_4$  and that this reaction leads to an increased disorder/strain in the host  $\text{NaBH}_4$  structure. Whilst it is difficult to ascertain if this effect is present at room temperature, the presence of a larger than expected FWHM ( $0.107^\circ$  vs.  $0.085^\circ$  seen before heating) in the diffraction pattern of the material does indicate that the material is less crystallographically ordered than pure  $\text{NaBH}_4$ . As discussed above, it is difficult from this analysis to be certain of the quantity of lithium based material that has diffused into the  $\text{NaBH}_4$  structure. The next step is to try and create a phase pure sample with a prescribed molecular amount of lithium present in the structure.

### 6.3.2 In situ synthesis of $\text{Li}_{0.1}\text{Na}_{0.9}\text{BH}_4$ (Li-0.1)

After mixing the appropriate molar ratios of  $\text{LiBH}_4$  and  $\text{NaBH}_4$ , the sample was heated for *in situ* HT-PXRD investigation. The initial results of this analysis (figure 6.5) show that again there is a discontinuity in the lattice parameter during heating at 200°C. Above this temperature the lattice parameters during cooling are initially consistent with the values during heating. However, at 200°C, the parameters diverge between heating and cooling. Below 200°C, the lattice parameter of the resulting sample is smaller than that of  $\text{NaBH}_4$  when heated; again this is similar to the behaviour shown during the initial synthesis in section 6.3.1.

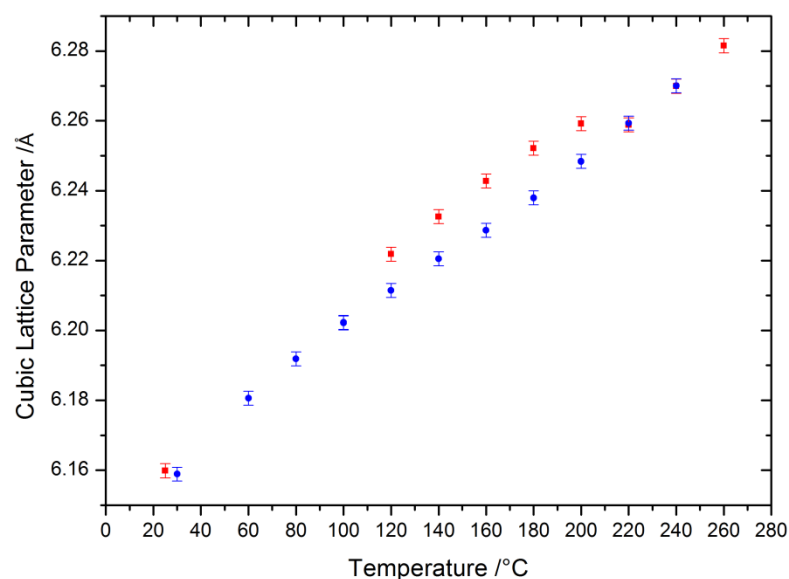


Figure 6.5 cubic lattice parameters of the sodium borohydride phase from the *in situ* Li-0.1 sample both during heating (black) and cooling (red) in the initial synthesis of the sample

The room-temperature lattice parameters show a slight ( $0.001\text{\AA}$ ) difference between the initial  $\text{NaBH}_4$  and the heated and cooled sample. This suggests that less lithium has been included in the structure than that in the sample in section 6.3.1, where equal molar amounts of  $\text{NaBH}_4$  and  $\text{LiBH}_4$  were initially mixed. The room-temperature x-ray scan shows that there is still some pure  $\text{LiBH}_4$  phase in the sample proving that not all  $\text{LiBH}_4$  has been reacted. The initial fraction of lithium inclusion from the first round of heating and cooling cannot be quantified using these data as Rietveld refinement will not allow for the intermixing of sodium and lithium on the sodium site of  $\text{NaBH}_4$  to be determined given the very low  $Z$  of lithium. However, we can estimate that this initial heating has allowed less than 10%  $\text{LiBH}_4$  to be included into the structure of  $\text{NaBH}_4$ . Subsequent *in situ* annealing was required to remove the residual  $\text{LiBH}_4$  from the material (as per the conditions in table 6.1). After re-heating and cooling the sample no evidence for a remaining pure  $\text{LiBH}_4$  phase was seen. Given that there are also no additional crystal phases in the room temperature scan and no anomalies in the background of the scan, which would indicate the presence of amorphous material (boron has a propensity for forming amorphous phases), it was concluded that after this annealing, all the  $\text{LiBH}_4$  material was incorporated into the structure of the  $\text{NaBH}_4$ .

Again the FWHM of the 002 peak in the  $\text{NaBH}_4$  structure was examined (figure 6.6). This shows a similar pattern to the initial synthesis (figure 6.4) in that the FWHM during heating

shows a large increase ( $0.017^\circ$ ) at the same temperature as the shift in the lattice parameter of the sample. During the cooling of the sample the FWHM at lower temperatures shows the same increase as the sample is cooled. There is also a slight increase ( $0.002^\circ$ ) in the FWHM at the same temperature as seen when heating. The reason for this is that there is additional inter-diffusion between ions at this temperature during cooling. It is unclear whether this diffusion is additional lithium diffusing into  $\text{NaBH}_4$  or the lithium added to the sodium borohydride during heating diffusing out of the material again. The reduced FWHM at this temperature ( $200^\circ\text{C}$ ) during cooling would indicate that the amount of diffusion is significantly lower as the sample is cooled. It is clear that this diffusion is curtailed at temperatures under  $180^\circ\text{C}$  and the same behaviour of the FWHM is observed as in the initial, equal molar mass, sample and that the relative amount of lithium and sodium in the structure are 'frozen in' until such time as the sample is heated again. However, as the lattice parameters during cooling do not show any change that could be associated with change in relative lithium and sodium concentrations, it is possible that this diffusion is curtailed to only within the sample. This would then account for the initial reduction in FWHM between  $200^\circ\text{C}$  and  $160^\circ\text{C}$  and how a phase pure sample can be formed relatively easily with only two annealing procedures needed.

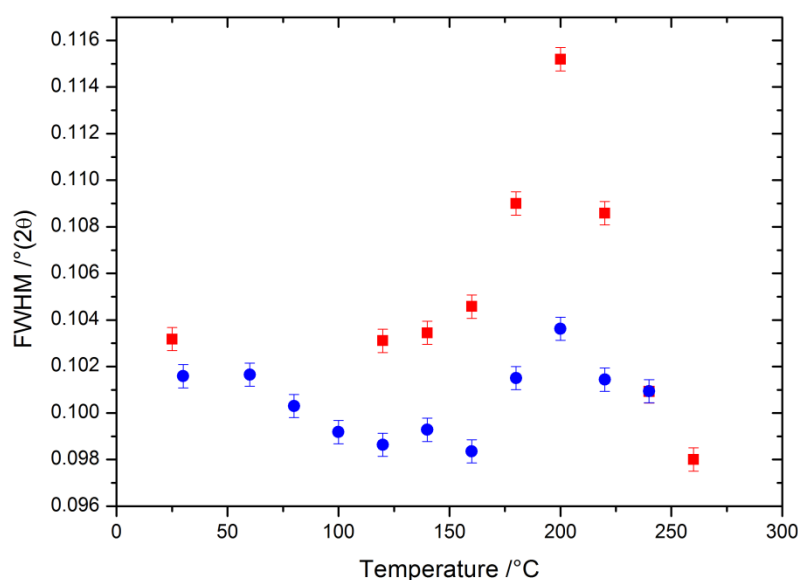


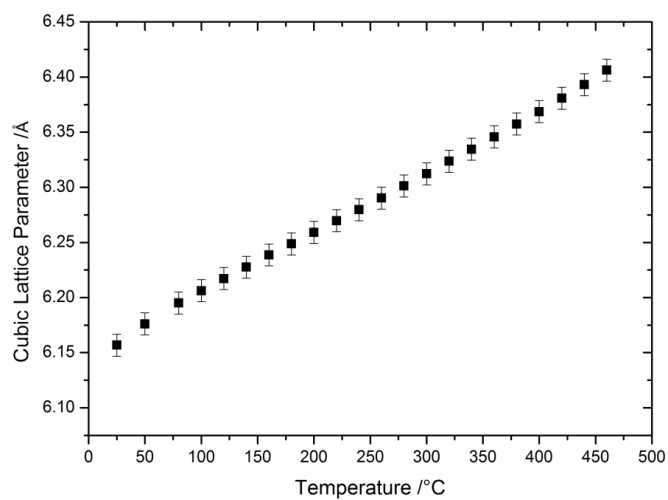
Figure 6.6 FWHM of the 002 reflection of the sodium borohydride phase from the in situ Li-0.1 sample both during heating (black) and cooling (red) in the initial synthesis of the sample.

### 6.3.3 In situ synthesis of Li-0.2 and Li-0.3

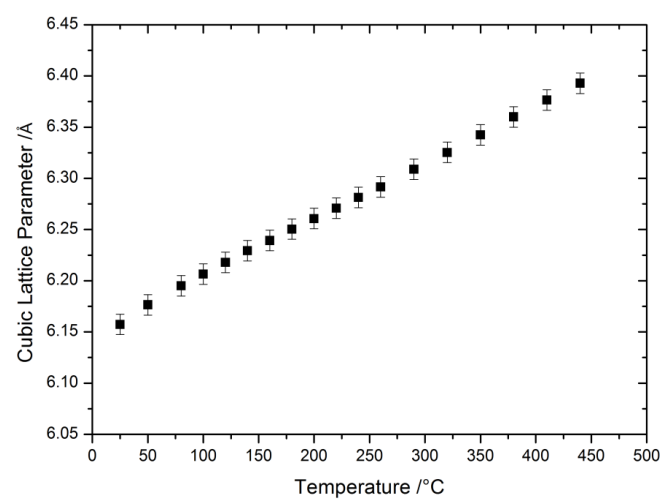
The other two samples were studied *in situ* in a similar way to the analysis given in section 6.3.2. The results show the same trends in both the lattice parameter and FWHMs of the samples. The initial heating of the mixture allows for a similar amount of lithium to be incorporated into the structure and the only way to increase the amount of lithium incorporated is to anneal the samples repeatedly at various temperatures until all the lithium present has been incorporated. It is unclear whether the increased lithium inclusion is as a result of the temperature of the annealing process or the repeated transition through the 200°C point where diffusion is maximised. At lithium/sodium ratios greater than that seen in sample Li-0.3, the diffusion reaches a saturation point where the in- and out-diffusion of lithium is in equilibrium, which precludes the formation of a phase-pure sample.

### 6.3.4 Ex situ analysis of Lithium Sodium Borohydride

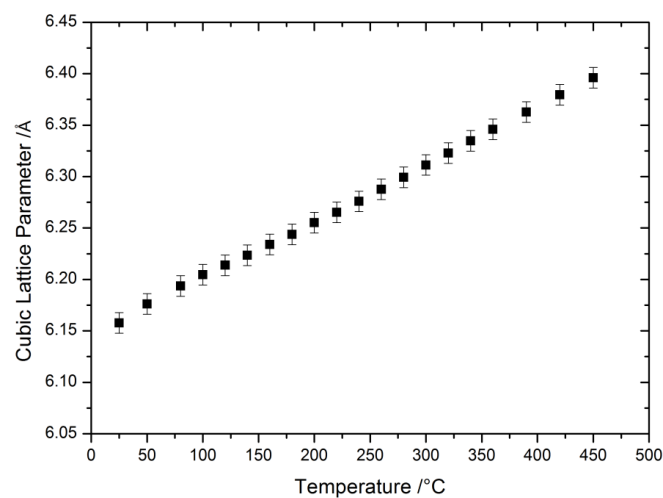
The three phase pure samples (Li-0.1, Li-0.2 and Li-0.3), having been synthesised as described in section 6.2, were then examined using HT-PXRD. The results of this (figure 6.7) show that there is no discontinuous change in the lattice parameter; unlike during the synthesis of these samples, there is no reduction in the lattice parameter at 200°C. This is further evidence that the samples are phase pure and there is no additional diffusion of lithium either into or out of the NaBH<sub>4</sub> structure. Obviously there can be no additional lithium inclusion as all lithium within the sample has already been incorporated; however, there could be lithium out-diffusion. The diffraction scans at temperatures around 200°C and indeed at all other temperatures, show no evidence of any additional crystal phases, which adds to the evidence that no lithium-containing phase has diffused out of the sample. The background of the scans is also unchanged as the samples are heated; there is no evidence of any amorphous phase forming during this heating. The results of the heating of all the samples show that they are all phase-pure throughout the whole temperature range, from room temperature to 450°C. This shows that once the samples have formed, they are thermally stable and do not easily degrade or separate into their constituent parts, NaBH<sub>4</sub> and LiBH<sub>4</sub>. This is in agreement with the conclusions from the *in situ* FWHM analysis of sample Li-0.1 (section 6.3.2) that there is no out-diffusion of lithium from the structure.



(a)



(b)



(c)

Figure 6.7 Cubic lattice parameters of the ex-situ synthesised samples of (a) Li-0.1, (b) Li-0.2 and (c) Li-0.3.

From the results given in figures 6.7 and 6.2, the value of the linear expansion coefficient of each of the samples has been determined. There is a slight deviation from linear expansion seen in all the figures in figure 6.7 at temperatures below 200°C; this could be due to a systematic unreliability of the x-ray furnace at low temperatures, as detailed in chapter 3. However, as analysis of the *in situ* samples has indicated that this temperature of 200°C may be inherently important to these materials. For example, it could be that these variations from linearity in the lattice parameters are a result of a phase change to a lower symmetry space group resembling the room temperature symmetry of LiBH<sub>4</sub>. The results of a straight line, least-squares fitting of the data in the figures is given in table 6.2. The fitting was carried out on data from temperatures above 200°C only to avoid the effects of the deviation, reasons for which are discussed above. Also given are the room temperature lattice parameters calculated from the refinement of the room temperature scans shown in the figures 6.7 and 6.2.

Sample	Room Temperature Cubic Lattice Parameter, a. /Å	Linear thermal expansion coefficient (x10 <sup>-4</sup> ) /°C <sup>-1</sup>
Pure NaBH <sub>4</sub>	6.162(1)	5.77(1)
Li-0.1	6.157 (1)	5.67 (1)
Li-0.2	6.157 (1)	5.59 (1)
Li-0.3	6.158 (1)	5.57 (1)

Table 6.2 Room temperature lattice parameters and linear thermal expansion coefficient of the three ex-situ synthesised samples and pure NaBH<sub>4</sub> calculated from the Rietveld refinement of the samples during heating (figure 6.7) and figure 6.2 for the pure sample.

Table 6.2 shows that the room temperature lattice parameters for the three lithium containing samples are very similar to each other and that these values are smaller than that of the pure NaBH<sub>4</sub> sample, indicating that there is a maximum amount of lattice parameter contraction that can be achieved regardless of the amount of lithium incorporation. The reduction in the lattice parameter is the same as that seen in the initial *in situ* synthesis of the Li-0.1 sample. From that analysis, the amount of lithium incorporation which produces this lattice contraction is less than the 10% incorporated in the *ex situ* Li-0.1 sample. This contraction is spontaneous and only a small amount of lithium inclusion is needed to produce this effect. Once this contracted lattice has been produced, any amount of subsequent lithium inclusion will not have a further effect on the room-temperature lattice parameter. However, the effect this lithium has on the thermal

expansion of the sample is important. From table 6.2, there is a difference (3.1%) in expansion coefficients between the pure  $\text{NaBH}_4$  sample and those of the samples which include lithium. There is a similar difference between the Li-0.1 and Li-0.2 synthesised samples; however, this difference is significantly smaller between the Li-0.2 and Li-0.3 sample, being only 0.36%.

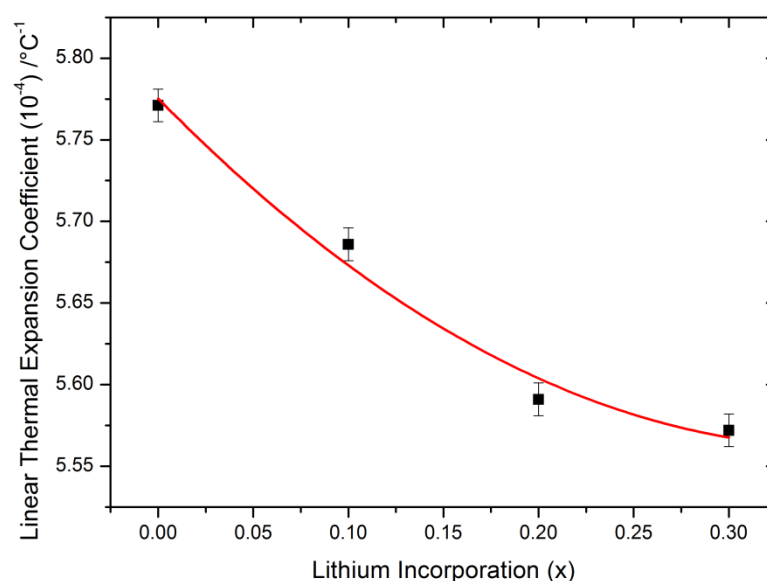


Figure 6.7 Linear thermal expansion coefficients of the various lithium containing samples and that of pure  $\text{NaBH}_4$  fitted to a parabola. The changes in this value vary non-linearly with lithium incorporation.

The graphical representation of these data (figure 6.7) shows this relation more easily. The inclusion of a small amount of lithium has had an obvious effect on the thermal expansion characteristics of the sample; however, this effect starts to become saturated as additional lithium is added. Similar changes in thermal expansion coefficients of  $\text{NaBH}_4$  are seen in other works where ions have been substituted into the structure. [3] In the latter study, the substitution of chloride onto the borohydride ions' position by the mixing of  $\text{NaBH}_4$  and  $\text{NaCl}$  is possible over the entire compositional range and results in a lattice contraction consistent with Vegard's law between the cubic lattice parameters of the end-members  $\text{NaBH}_4$  and  $\text{NaCl}$ . However, whereas both those materials have the same crystal structure, the  $\text{LiBH}_4$  in this study has a different structure and Vegard's law does not apply. These differences in structure may explain why samples with a greater amount of lithium incorporation are difficult to synthesise. Because there is little change in the thermal expansion, the amount of lithium incorporation in the  $\text{NaBH}_4$  structure reaches a saturation point where no additional lithium can be accommodated. If there is indeed a saturation



point, then the presence of further lithium may have a deleterious effect on the crystal quality of the material as the amount of lithium inclusion approaches this concentration.

To investigate if there is a phase change in the samples at temperatures below 200°C, the FWHM of the 111 and 002 reflection of the samples was examined over the range of temperatures up to approximately 450°C (figures 6.9 and 6.10). This analysis of the FWHM also gives a measure of the crystal quality and the strain within the samples.

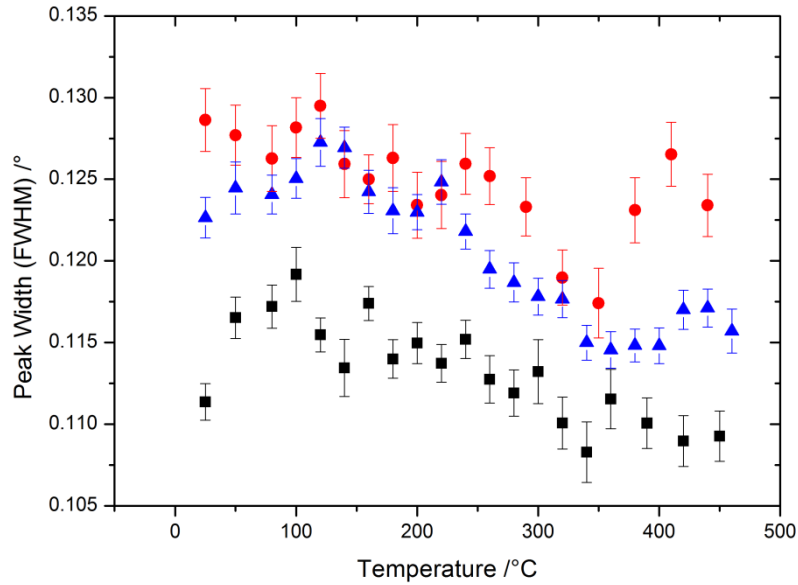


Figure 6.9 FWHM of the 002 reflection of the Li-0.1 (Blue), Li-0.2 (red) and Li-0.3 (black) samples over the temperature range up to 450°C

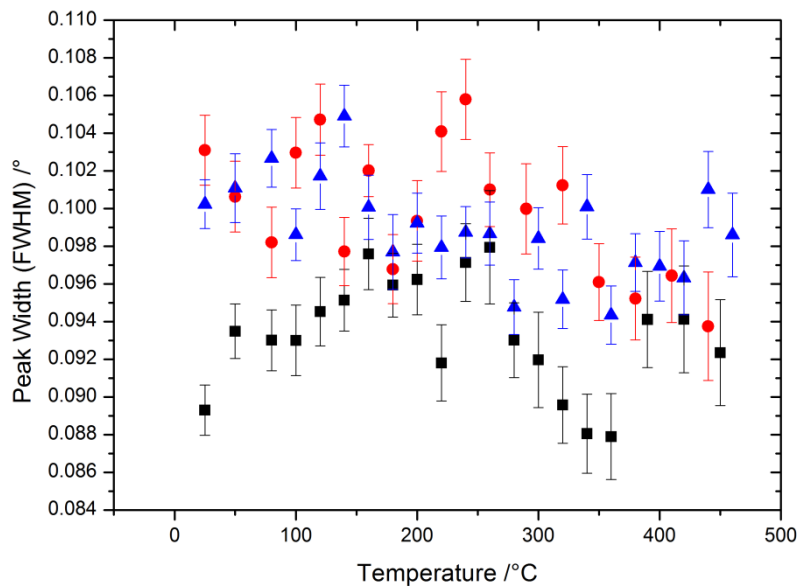


Figure 6.10 FWHM of the 111 reflection of the Li-0.1 (Blue), Li-0.2 (red) and Li-0.3 (black) samples over the temperature range up to 450°C

Examining the FWHM of the 002 diffraction peak shows that there are two features of note; an increase in the FWHM up to a temperature of 100°C and then a reduction of the FWHM up to a temperature of 320°C, where the value is subsequently constant up to 450°C. There are variations in this trend, especially in the Li-0.2 sample, which maybe a result of the extended annealing time this sample required. The width of the reflection of the two samples with 0.2 and 0.1 lithium incorporation are consistent with each other over the majority of the range of temperatures, which is consistent with their showing a similar distribution of lithium and sodium within the structure and, therefore, similar crystal qualities leading to the generally linear changes in thermal expansion seen in figure 6.7. The reduction in the FWHM between 100°C and 320°C could indicate that the peak is changing from a triplet to a single peak which would be indicative of a phase change from orthorhombic to cubic symmetry. However, these temperatures do not correspond with the deviation of the lattice parameters seen in figure 6.7 and so we suggest that the reduction in FWHM seen here is actually a result of a reduction in strain within the samples. The FWHM of the 111 peak of the Li-0.1 sample is broadly constant indicating that the changes in the 002 FWHM may indeed be a result of a subtle phase change. However, as the amount of lithium inclusion increases, in the Li-0.2 and Li-0.3 samples, the 111 FWHM peak appears to increase up to a temperature of 200°C and then begins to decrease again. In the Li-0.3 sample this trend is seen most obviously. This trend of increasing then decreasing FWHM is similar to that seen in the 002 FWHM during the in situ synthesis and is attributed to the diffusion within the sample and explains why the change in the FWHM seen here is at 200°C

The FWHM of both the 111 and 002 peak from the Li-0.3 sample is consistently smaller than the other two samples which is counter-intuitive given that the increased amount of lithium in the NaBH<sub>4</sub> structure would increase the strain within the sample given the increased distribution of lithium leading to localised lattice contractions. However, the data given in figure 6.9 would seem to disagree with this hypothesis. Rather, the sample quality has apparently increased implying that the amount of in-built strain within the structure has been reduced. This, coupled with the thermal expansion results discussed above, seems to confirm that there is a saturation point of lithium inclusion in to the material, which has a substantial effect not only on the thermal expansion at this point but on the quality of the resultant material, which appears optimal when only the width of x-ray diffraction peaks is considered. This optimisation could be the source of the reduced change in the thermal expansion of the Li-0.3 sample, the saturated lithium inclusion

having the effect of tempering the lattice expansion by reducing the strain in the sample. Clearly the increased strain in the samples with less lithium inclusion has allowed the thermal expansion rate of these samples to be reduced relative to the pure NaBH<sub>4</sub> sample. This “hardening” of the lattice in the Li-0.3 sample could also, however, have the effect of increasing the hydrogen desorption temperature of this material and, thus, reduce the usefulness of the sample as a hydrogen storage material.

### 6.3.5 Nuclear Magnetic Resonance

Until now, using only x-ray diffraction analysis, it has been difficult to determine absolutely that the changes seen in the lattice parameters and thermal expansion of the samples have been as a result of the inclusion of lithium into the structure and whether this lithium is incorporated into the structure on a substitutional or interstitial site. Whilst the *in situ* samples for diffraction were sealed in a capillary together with any decomposition products on heating, for the *ex situ* synthesis, this was not the case. Ex situ samples were not sealed and therefore any decomposition of the constituent materials could result in lithium being removed from the crucible and these would not then be evident in subsequent x-ray diffraction. Nuclear magnetic resonance (NMR) is a nucleus-specific technique that gives details of short-range order on the scale of the chemical bond. Therefore, even if the lithium were contained in an amorphous phase, NMR would give evidence of this phase, which would not necessarily give any signature of consequence in an x-ray diffraction pattern.

The results of the NMR of lithium-7 (figure 6.11) show that all three *ex situ samples* as a detectable signal at the expected chemical shift position is found in all cases. As lithium has a spin,  $I$ , of  $I = 3/2$ , the configuration of the NMR signal would show quadrupolar line shape broadening of the peak for almost all environments in which the lithium could exist, whether that be a site in an amorphous phase or in a crystalline phase. The only environments where the peak in the lithium spectra is as well defined as that seen in figure 6.11 are highly-symmetric sites such as that seen in the structure of NaBH<sub>4</sub>, which as a structure of cubic symmetry as denoted by the space group of the sample,  $Fm\bar{3}m$ , (figure 6.1). As the structure of LiBH<sub>4</sub> does not have the level of symmetry required to produce this spectrum, it can be definitively stated that the lithium detected is not incorporated in the initial orthorhombic phase but in some other higher-symmetry phase. Additionally, there is no evidence for an amorphous structure, from the NMR result (figure 6.11), and no evidence of another highly symmetric crystal structure in the x-ray analysis. Therefore, by a

process of elimination, we conclude that the lithium within the material must be present in a cubic Li-doped  $\text{NaBH}_4$ -type structure. The absence of any additional peaks in the chemical shift of the lithium spectra also implies that there are no other chemical environments within the  $\text{NaBH}_4$  structure, implying that none of the lithium has diffused into the material on to interstitial sites.

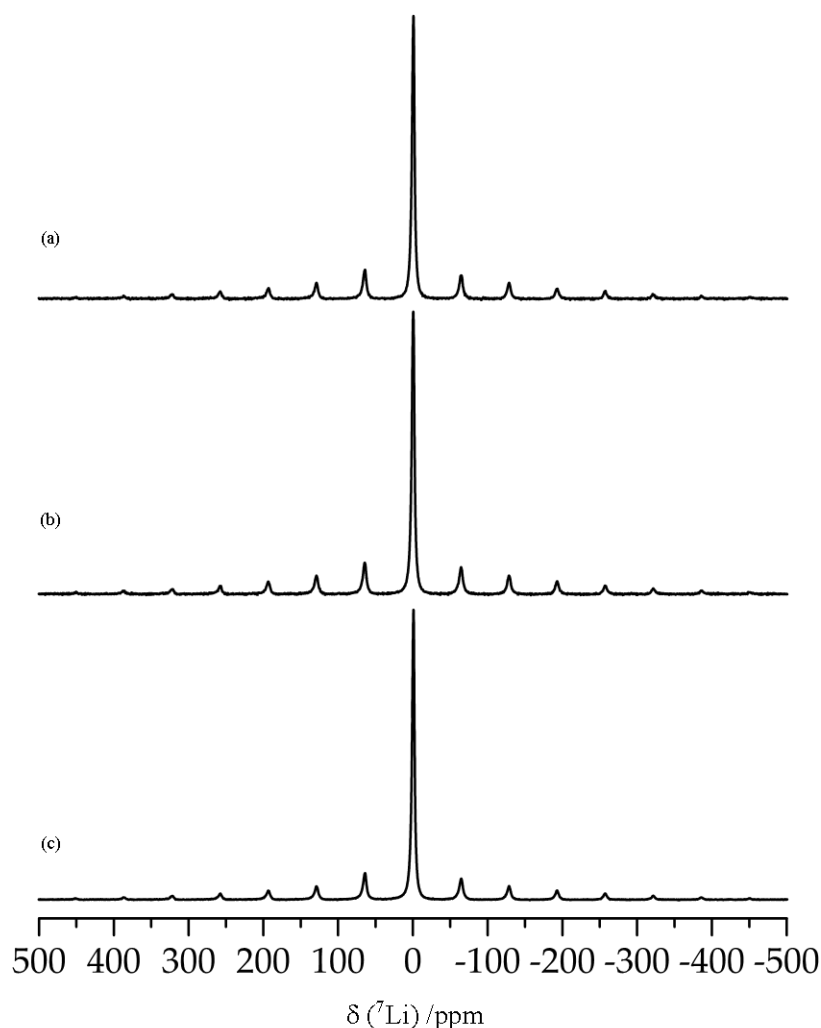


Figure 6.11 lithium-7 NMR results from Li-0.1 (a), Li-0.2 (b) and Li-0.3 (c) ex-situ synthesised samples. The less intense peaks either side of the main peak are the spinning side bands associated with the NMR experiment.

Continuing from the lithium-7 NMR results above, the results of the sodium-23 NMR (figure 6.12) show that there is a similar well-defined peak in the spectra, corresponding to the shared Na/Li site in the cubic Li-doped  $\text{NaBH}_4$ -type structure. Sodium-23 has the same quantised value of spin,  $I$ , as that of lithium-7,  $I = 3/2$ , and as a result, is subject to the same quadrupolar line shape effects as that of lithium-7. Figure 6.12(a) is the sodium-23 spectra of pure  $\text{NaBH}_4$  which shows a well defined peak; this is a result of the high degree of symmetry inherent in the pure  $\text{NaBH}_4$  sample. As the x-ray diffraction of the lithium

containing samples has shown, the symmetry of these samples is the same as that of pure  $\text{NaBH}_4$ , this is then confirmed by the NMR which shows the sodium in all of the samples is subject to the same local symmetry, which manifests itself as the well-defined peak seen in all the sodium-23 spectra in figure 6.12. A more detailed examination of the main peak in each of the sodium spectra from the lithium containing samples shows that there is an increase in the broadening of the chemical shift of the sodium site with increasing lithium inclusion. Whilst this cannot be resolved into two peaks and therefore two distinct chemical shifts, this broadening is most likely due to the reduction of the local symmetry of the site resulting from the lithium substitution on this site, which would cause a larger second order quadrupole moment. This is also the reason why the intensity of the spinning side bands within the spectra has increased in the samples as the amount of lithium inclusion has increased. This reduction in local symmetry is seen in the short range order of the site; however, over longer length scales within the structure, this is averaged out and results in the same long-range average crystal structure of cubic symmetry.

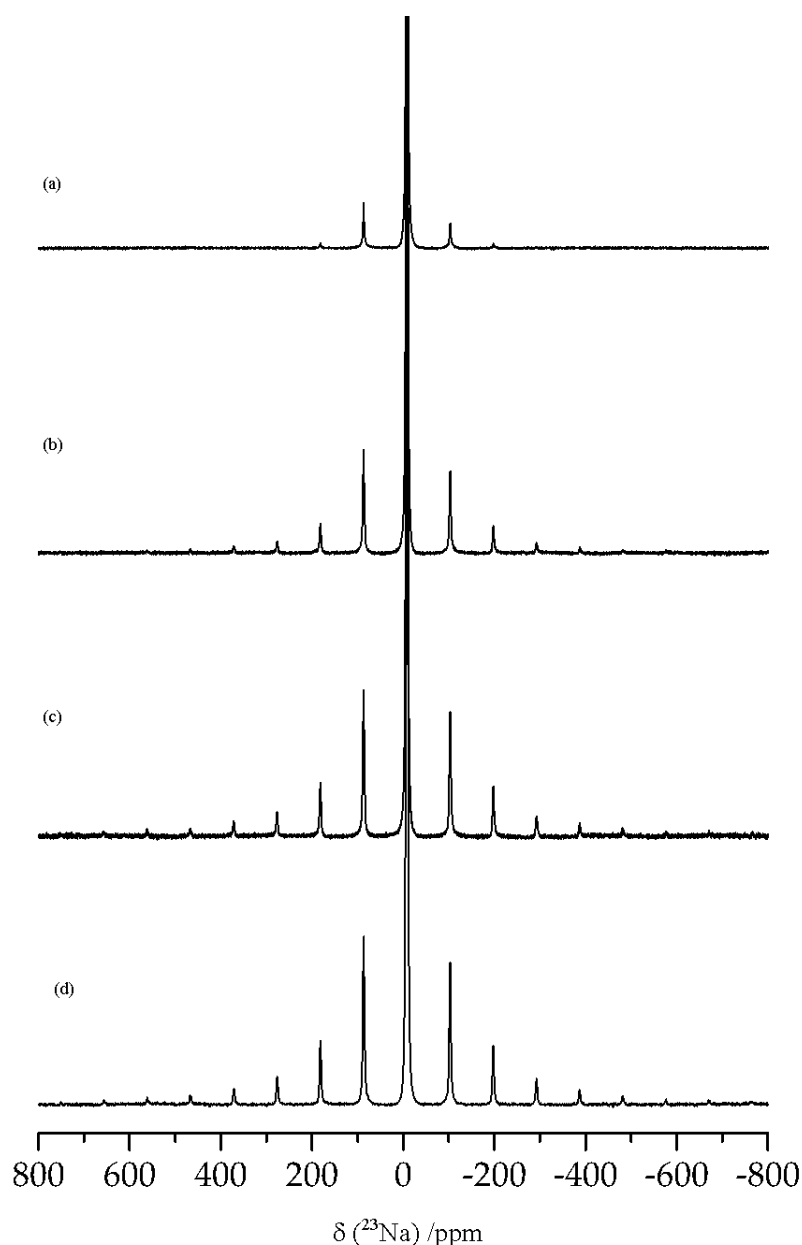


Figure 6.12 sodium-23 NMR results from a pure sample of  $\text{NaBH}_4$  (a) and, in addition, Li-0.1 (b), Li-0.2 (c) and Li-0.3 (d) ex-situ synthesised samples. The less intense peaks either side of the main peak are the spinning side bands associated with the NMR experiment.

This reduction in the local symmetry of the samples can also be seen in the boron-11 spectra. (Figure 6.13) The very weak feature seen in the boron spectra between the main peak and the spinning side band at approximately 10ppm chemical shift is evidence for a second boron environment. With boron-11 also having a spin of  $I = 3/2$  and the peak having a quadrupolar line shape, this indicates that this environment has lower symmetry than that of the main environment. Although there is some evidence for this site in the pure  $\text{NaBH}_4$ , the amount of boron populating this environment increases as the lithium content increases; this is further evidence that the lithium in the samples is causing a

reduction of the local symmetry of the crystal. By examining the relative intensities of this site and the main environment in the samples, it is clear that this less symmetric site is not highly populated and represents only a small volume fraction of each sample. The main peak in the figure is that from the expected boron environment of the sample, seen in all the Li-containing samples as well as the pure  $\text{NaBH}_4$ . With the assumption that the lithium is substituted on the sodium crystallographic site, the boron site should be split as the next nearest neighbours of this boron could be sodium and sodium, sodium and lithium, and less likely lithium and lithium. However there are several reasons why these individual sites cannot be discerned from the NMR results. Firstly, the highly-symmetric site leads to the narrowing of the main boron peak to the point where it becomes very difficult to resolve any of the fine structure within the resolution of the NMR experiment. Secondly, as the closest atoms to the boron site and therefore the ones that have the largest effect on the chemical environment of the boron are the hydrogen atoms which make up borohydride ion, shielding of the boron site by these hydrogen atoms reduces the effect of the sodium and lithium distributions on the boron spectra. Finally, the magnetic environments produced by the sodium and lithium are very similar given the similarity of the atomic radii and magnetic moments of each nuclei.

Whilst no direct evidence can be obtained from the main peak in the boron-11 spectra for the inclusion of lithium, taken with the spectra of the other main nuclei in the material a representation of the structure of the samples and the position of the lithium within the structure can be developed. The results of the NMR spectra presented here show that the assumptions made from the x-ray diffraction experiments are correct and the lithium within the sample is substituted on the crystallographic sodium site in the structure of  $\text{NaBH}_4$ . It is this substitution of lithium which has altered the properties of the material which have been discussed earlier in this chapter.

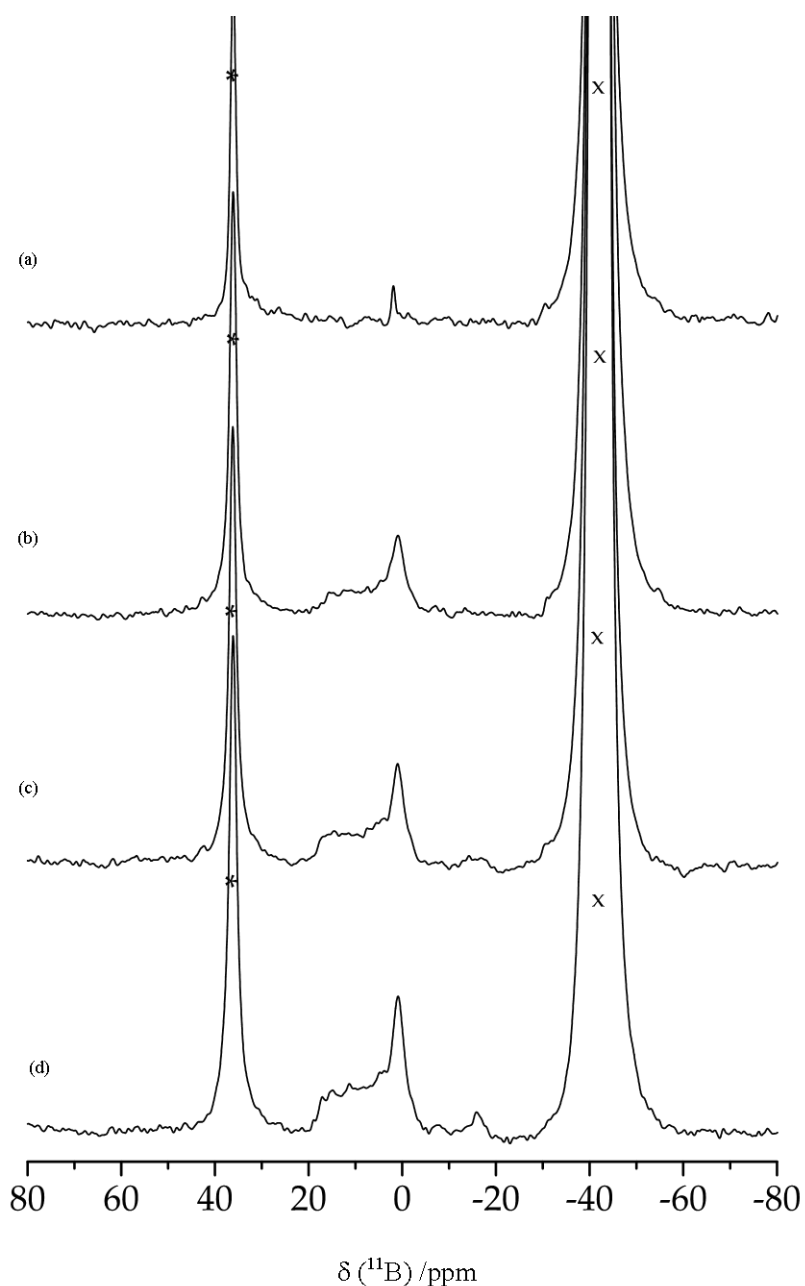


Figure 6.13 boron-11 NMR results from a pure sample of  $\text{NaBH}_4$  (a) and, in addition, Li-0.1 (b), Li-0.2 (c) and Li-0.3 (d) ex-situ synthesised samples. The peaks labelled with x correspond to the main peak in the spectra whilst the spinning side band is labelled (\*).

### 6.3.6 Thermal Analysis

The samples, Li-0.1, Li-0.2 and Li-0.3 have been examined using powder x-ray diffraction up to the temperature of 450°C. At this temperature, a sample of pure  $\text{NaBH}_4$  starts to slowly release hydrogen up to the temperature of 550°C, where the majority of hydrogen release takes place. [1] Clearly, as these samples are still solid at this temperature and there is no indication that the sample has either melted or started to decompose, if any hydrogen release has started before this temperature, it must be very slow. There is evidence that



hydrogen is indeed being released from the samples as it has proved difficult to examine the samples using x-ray diffraction at higher temperatures. The reason for this is that as the samples are sealed in a capillary so that any release of hydrogen results in an increase in the pressure within the capillary causing it to break and fall out of the x-ray beam. The outcome of this means that Differential Thermal Analysis (DTA) has had to be used to investigate the desorption temperatures of the synthesised samples. The results of this thermal analysis (figure 6.14) shows that each sample undergoes a single stage exothermic event which corresponds to the desorption of the material, as the reverse of this event is not seen during cooling as would be the case if the sample has simply melted. The inclusion of lithium into the structure of  $\text{NaBH}_4$  has indeed altered the desorption temperature of the samples; however the reduction of the temperature is only approximately  $50^\circ\text{C}$ . This change in temperature is at least in the right direction as a lower desorption temperature will make this material more efficient as a hydrogen storage material; however, a desorption temperature of around  $500^\circ\text{C}$  is still too high to make this material a viable solution. The greater lithium concentration in sample Li-0.3 has reduced the desorption temperature to  $504(1)^\circ\text{C}$ , whereas samples Li-0.2 and Li-0.1 release the majority of hydrogen at  $507(1)^\circ\text{C}$  and  $510(1)^\circ\text{C}$ , respectively. It would seem that just having at least *some* lithium in the structure of the material is enough to significantly reduce the desorption temperature but the exact lithium concentration may be less important in producing this change.

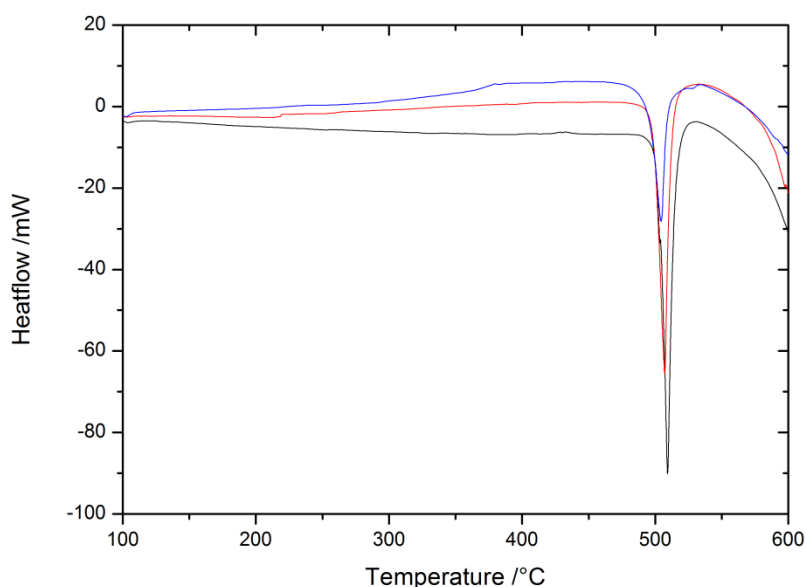


Figure 6.14 Differential thermal analysis (DTA) of the three samples Li-0.1 (black), Li-0.2 (red) and Li-0.3 (blue).

## 6.4 Conclusions

This work has shown that it is possible to incorporate lithium into the structure of sodium borohydride by the reaction of  $\text{LiBH}_4$  with  $\text{NaBH}_4$ . Detailing x-ray diffraction and NMR analysis has shown that the lithium is substituted onto the sodium site of the  $\text{NaBH}_4$  structure. This lithium substitution has created some distortion of the short range symmetry of the structure and the increased amount of lithium increases the amount of lower symmetry sites within the sample. It is relatively easy to introduce a small amount of lithium into  $\text{NaBH}_4$  by heating to a temperature of c.a.  $200^\circ\text{C}$ , but this ratio of lithium inclusion to sodium ions is less than 10%. To increase the amount of lithium substitution, mixtures of the specified molar ratio have to be annealed; the annealing temperature is dependent on the amount of lithium that is to be incorporated into the sample. To allow for more lithium to be incorporated, higher annealing temperatures are required. Once the lithium is incorporated into the sample, it appears that it cannot be diffused out again and that the sample maintains its  $\text{NaBH}_4$  structure throughout heating up to at least  $450^\circ\text{C}$ . There is however a deviation from linear thermal expansion seen in all three samples which at first glance may appear to be the result of a phase change in the material from a lower symmetry phase to a cubic phase at temperature above  $200^\circ\text{C}$ . Whilst the FWHM of various diffraction peaks from the sample supports this hypothesis, NMR has proved that the both the lithium and sodium within the structure occupy highly symmetric (cubic) sites even at room temperature. The deviation from linear thermal expansion and the behaviour of the FWHM of the samples has therefore to be a result of the disorder in the samples at these temperatures, which is suggested to be brought about by the diffusion of the ions within the cubic structure of the material. There is a maximum amount of lithium that can be substituted into the structure and this limit appears to be c.a.  $x=0.3$  in the formula  $\text{Li}_x\text{Na}_{(1-x)}\text{BH}_4$ . Above this concentration no phase-pure sample can be formed. Lithium substitution affects the cubic lattice parameter of the material by contracting the room-temperature lattice parameter. However, this value is constant regardless of the extent of lithium substitution. The thermal expansion of the resulting material is noticeably dependent on the amount of lithium substitution; the rate of expansion is reduced with increasing substitutional lithium. However, this change in thermal expansion rate is very much reduced in the sample that has the perceived maximum amount of lithium inclusion.

In terms of the potential of this mixed lithium sodium borohydride material as a hydrogen storage material, the inclusion of lithium has had several effects on this potential. Firstly,

and perhaps most importantly, the desorption temperature of the material has been reduced by almost 10%, from 550°C to 504°C. Whilst this reduction isn't large enough to make the material viable for on board hydrogen storage, it does show the potential of developing materials based on the mixing of different borohydrides. There are other changes in the properties of these mixed lithium sodium borohydride materials which would benefit its potential as a storage material:- as lithium is lighter than sodium, the inclusion of lithium reduces the overall weight of the material thereby increasing the hydrogen weight percentage of the material. As the room temperature lattice parameter of the mixed borohydride is smaller than that of  $\text{NaBH}_4$ , the density of the material is greater than that of pure  $\text{NaBH}_4$  and as such, the volumetric hydrogen storage density has also increased. Finally with the reduced thermal expansion coefficient of the material, large volumes of the material used as a hydrogen storage medium require less space as they expand, again improving the volumetric density of the overall storage device.

## 6.5 Further work

This work has showed that these types of mixed borohydride materials have the potential to produce new materials with properties that are more suited to use as hydrogen storage materials than their constituent borohydrides. Clearly any future work would have to involve development of additional mixed borohydride to try and find mixed borohydride samples which have lower hydrogen desorption temperatures and greater hydrogen weight percentages. There is a further development of these types of mixed borohydrides by mixing materials with different valence ions such as  $\text{Mg}(\text{BH}_4)_2$  with the materials examined here,  $\text{NaBH}_4$  and  $\text{LiBH}_4$ . It is unclear whether it would be possible to develop a phase pure sample based on these type mixtures and whether this new phase would be the same as one of the constituent structures, as is the case in this work, or a new phase unrelated to either of the constituents. If a phase pure material cannot be developed it is not to say that the mixture of these borohydrides would not help improve the desorption from the sample. Extending this principle further, tertiary mixtures of potential borohydride materials can be investigated. This develops a wide range of potential materials all of which would have to be investigated to find new approaches to developing hydrogen storage materials.

With specific reference to the samples produced here the additional work would involve trying to develop samples with greater amounts lithium incorporation than that seen in the

three samples produced. All the trends shown in this work show that increasing the amount of lithium incorporation into  $\text{NaBH}_4$  has improved the properties of the material to make it more desirable as a hydrogen storage material, further lithium inclusions could further improve these properties to the point where the material could be viable as a storage medium.

The use of NMR at high temperatures, around  $200^\circ\text{C}$  would allow for further investigation of the diffusion process that initially forms the mixed borohydride material and may offer an insight not only into how more lithium could be included in the structure but also what mechanism produces the lower symmetry sites within the structure. Populating more of these sites could effect the desorption of the material further deducing this temperature.

Finally, exploring the desorption process using x-ray diffraction would be desirable as it would show what materials the mixed borohydride desorbs into and whether all the hydrogen stored in the material is desorbed or if an intermediate hydrogen containing material is formed with a desorption temperature higher than the temperature already seen. For this investigation to be possible it would require a new method of examining air sensitive samples at high temperature that would not involve the use of sealed glass capillaries but still protect the sample from the atmosphere or some way of relieving the pressure build up within the capillary as the sample starts releasing hydrogen.

## References

- [1] A. G. Ostroff, R. T. Sanderson, J. Inorganic and Nuclear Chemistry **4** (1957) 230-231
- [2] J. C. Slater, J. Chemical Phys. **41** (1964) 3199
- [3] D. B. Ravnsbæk, L. H. Rude, T. R. Jensen, J. Solid State Chemistry **184** (2011) 18-58-1866

# Chapter 7

## Conclusions

### 7.1 Hydrogen Storage Materials

In terms of new materials for hydrogen storage, this work has shown that it is possible to produce new materials from a mixture of two existing hydrogen containing materials and that these new materials have different properties from those of their constituent materials. In most cases, these new properties make the new material more favourable for hydrogen storage. In the case of mixed lithium and sodium borohydride materials, the introduction of lithium into the structure of  $\text{NaBH}_4$  has resulted in a reduction of the thermal expansion rates as the amount of lithium has increased, figure 6.7, which makes the overall volumetric density of any storage system greater than a system using  $\text{NaBH}_4$  alone.

Similar reductions in the thermal expansion of  $\text{NaBH}_4$  had previously been seen by the substitution of chlorine into the structure although this modification did not improve the desorption temperature of the resultant sample or the weight percentage hydrogen contained in the sample, as chloride replaces the borohydride ion in the sample. In the work presented in this thesis lithium, a lighter element than the sodium it replaces, has not only improved the hydrogen weight percentage of the sample but has also reduced the desorption temperature of the mixed material, (figure 6.14) by over 8% from 550°C to a minimum of 504°C. Both of these modifications have helped improve the materials usefulness as a hydrogen storage material over that of the original  $\text{NaBH}_4$  and perhaps suggest a way forward for tuning of further hydrogenic materials via the complexing of end-members of different crystal symmetry within solid-solutions.

Conversely, the use of crystallography to examination another hydrogen storage material, di-sodium amide borohydride, has revealed that this material can exist in one of three structural phases and the transition between these phases is dependent on the rate at which this material is heated and cooled. There is also a discrepancy between the relative amount of each phase, which exists between the heating and cooling of the material. Whilst these properties of the material will not affect the hydrogen desorption temperature, they do have an effect on the overall volumetric density of the sample. There

is a small discontinuity between the densities of the material per formula unit in each of the phases, which leads to a difference in the overall density of the material between heating and cooling (figure 3.13) which is only exacerbated by the increased heating and cooling rates that would be used if the material was to form part of a hydrogen storage device.

## 7.2 Dilute Nitrides

The analysis of the homoepitaxially grown dilute nitride layers shows that the amount of nitrogen incorporation can be predicted as there is a linear relationship between the growth temperature and this quantity. This relationship differs for different growth rates, namely at higher growth rates the rate of nitrogen incorporation is curtailed. An example of the data are shown in figure 4.3. An understanding of this relationship allows for samples to be grown with a specific amount of nitrogen incorporation, allowing the bandgap of the semiconductor to be tuned to a specific energy corresponding to the infrared region of the spectrum.

In previous works, the nitrogen containing layer has been assumed to be 100% strained on the substrate. However, we have shown that this is not the case for our samples and that use of this assumption leads to inaccurate determination of the true nitrogen content of the layer. Accurately to determine this nitrogen content further, more sophisticated analysis techniques has been deployed, for example, reciprocal space mapping of both a symmetric and asymmetric reflection has been performed. This analysis has also allowed for the quality of the crystal growth to be further examined. It was shown that the crystal quality of these layers is improved as the nitrogen content is increased, which is counter-intuitive given that this increases the mismatch between the layer and substrate. However the over-riding factor affecting the quality of the layer is shown to be its growth temperature, which is reduced for a sample with increased nitrogen incorporation. (figure 4.9) This automatically leads to a situation where samples with greater nitrogen incorporation have better crystal quality, thereby making them more efficient photovoltaic materials.

Annealing of GaNSb layers grown on GaAs has shown that during growth nitrogen is not only incorporated on to crystallographic sites but also on to an interstitial site within the structure of the material. Further to this, annealing has showed that this interstitial nitrogen can be transferred into substitutional sites. This effect is seen over a wide range of nitrogen incorporation and maximisation of the substitutional nitrogen incorporation is

seen at increasing annealing temperatures as the amount of already-substitutional nitrogen is decreased. It is hypothesised that this arises because of the increased diffusion rate within the layer, given the increased amount of nitrogen in the structure. At increased annealing temperatures, substitutional nitrogen is diffused out of the structure of the layer and the amount of functional nitrogen substitution is reduced, resulting in a change in the bandgap energy of the material. These results are summarised in figure 5.4, which show the amount of substitutional nitrogen given the annealing temperatures.

Further to this, analysis has shown that the mosaic spread within the layer increases as the amount of substitutional nitrogen increases, which is contradictory to the analysis of the homoepitaxial samples. This indicates that the type of substrate that the layer is grown on is important in determining its crystal quality.

These investigations have shown that the total amount of nitrogen within all the samples, regardless of the growth temperature or annealing temperature, is constant and the only differences that the growth temperature has on the composition of the sample is to change the initial ratio of nitrogen in substitutional and interstitial sites. This ratio can then be subsequently affected by annealing.

Finally, the amount of substitutional nitrogen contained within these layers can be controlled and manipulated to produce samples with both the desired amount of nitrogen incorporation, and therefore bandgap reduction, and the necessary crystalline quality which, for the most part, is linked to its growth temperature but can also be affected by the annealing regime subsequently adopted. There is a delicate balance between the growth and annealing effects to produce a sample with the optimum level of nitrogen incorporation and the best possible crystal quality, as is required to improve the efficiency of these materials for real solar-cell devices.

### 7.3 Suggestions for Further Study

This work has highlighted areas where further studies could be undertaken, for example whilst this work has shown differences between nitrogen incorporation between GaSb and InSb, additional studies of nitrogen containing layers based on other materials, such as AlSb, could lead to development of layers which have greater nitrogen content at lower temperatures- improving both the bandgap reduction and crystal quality of the layers. These additional materials may allow for a greater amount of interstitial nitrogen inclusion which may become substitutional when annealed. Annealing of these materials may have a



greater effect changing the ratio of substitutional to interstitial nitrogen by allowing for greater diffusion of the atoms during annealing.

This work has shown that the properties of hydrogen storage materials can be changed for the better by producing solid-solutions of mixed samples therefore additional studies of these types of materials has the potential to find examples with specific properties which make them viable for on-board hydrogen storage. Mixing of borohydride materials with different valences as well as different crystal structures could be one way of developing these new materials. For example a study of a system based on magnesium borohydride and either lithium borohydride or sodium borohydride (all of which have different crystal symmetry) could result in materials which, not only very high hydrogen weight percentages, but also have favourable desorption temperatures. This field of study could be further extended by trying to develop tertiary, phase pure, compounds and examining their properties.